ÅGE GRØNNINGSÆTER

REDUCTION OF ACOUSTIC AND ELECTRONIC NOISE IN INTRAVASCULAR ULTRASOUND IMAGING

NTH
UNIVERSITETET I TRONDHEIM
NORGES TEKNISKE HØGSKOLE

DOKTOR INGENIØRAVHANDLING 1992:57
INSTITUTT FOR TEKNISK KYBERNETIKK
TRONDHEIM

ITK-rapport 1992:52-W

Reduction of acoustic and electronic noise in intravascular ultrasound imaging

by

Åge Grønningsæter

A thesis submitted for the degree of

Dr.ing.

University of Trondheim

Norwegian Institute of Technology

Department of Biomedical Engineering

and

Division of Engineering Cybernetics

Trondheim, July 1992

NTH-TRYKK
1993

Preface

In the middle of 1986, the development of an intravascular imaging system was begun by *"Cardiovascular Imaging Systems, Inc."* (California) at the Department of Biomedical Engineering, Medical Faculty, University of Trondheim. This thesis is a continuation of the prototype development for improving the image quality and especially the blood/wall contrast. The prototype with modifications was used in the experiments.

This degree is applied for through the Division of Engineering Cybernetics, Norwegian Institute of Technology, University of Trondheim in collaboration with Department of Biomedical Engineering. The work was carried out at the Department of Biomedical Engineering. The academic advisers were professor Bjørn Angelsen and associate professor David T. Linker, both from the Department of Biomedical Engineering.

The work was funded by a scholarship from the Norwegian Institute of Technology.

Summary

This thesis describes methods to reduce noise in intravascular ultrasound images. The noise signals considered are: echo from blood, reverberations, echo from laser generated gas bubbles, thermal plus amplifier noise and electromagnetic interference. A model for the RF-signal is developed, and parts of the model are verified by measurements. Algorithms for noise reduction are developed based on linear filtering and/or detection and canceling:

Electronic noise is reduced by oversampling and low pass filtering. Reverberations from the catheter housing are detected and canceled based on constant phase properties in the signal. Two methods for blood noise reduction are found: 1) The ultrasound beam is tilted slightly up or down-stream to obtain a Doppler shift from blood. Lateral low-pass filtering in each depth location rejects blood noise due to frequency diversity. 2) The location of the vessel wall is detected and signal in other regions canceled. This method is based on correlation properties of vessel wall and blood signal.

The algorithms are tested by acquiring data in the laboratory, transferring raw RF-data to a computer and performing post processing on the computer. It is also shown that it is possible to implement the algorithms in real time on an ultrasound imaging system.

Acknowledgemets

Several people have contributed to make this thesis a reality. I would like to thank:

Bjørn A. J. Angelsen, professor at Department of Biomedical Engineering, University of Trondheim, who encouraged me to start with this work. His knowledge and technical insight has been of great inspiration to me. Also I have gained valuable knowledge from the numerous discussions with him on minor and major technical issues. He has also been of great help in the final work with the manuscript.

David T. Linker, associate professor at Department of Biomedical Engineering, for valuable help in the initiating phase. He contributed to defining and setting a frame for the thesis. As my supervisor prior to and during the work, I have gained valuable experience and knowledge from him.

Hans Torp, assistant professor at Department of Biomedical Engineering, for ideas and valuable comments during the work. His contribution on the final work with the manuscript has been absolutely indispensable.

Audun Græsli who has made a substantial job by improving and implementing required hardware for data acquisition. During the 15 months, we had continuous fruitful and encouraging discussions on practical and theoretical issues.

Axel Brisken, director of development, Cardiovascular Imaging Systems Inc (CVIS), California, for the supply of transducers and components for the low noise pre-amplifier. These components have been very helpful for the practical measurements. He has also contributed with valuable information on practical intravascular imaging. CVIS also provided financial support to the development of a "Quadrature Demodulator" which made it possible to digitize the RF-signal. This is also gratefully acknowledged.

Kjell Kristoffersen for comments and good ideas, particularly in the simplification of the real time implementation.

Stewart Clark at SINTEF and my friend Arne Erikson have provided valuable comments and suggestions on the English language.

Ketil Jensen, Stein Dørum and Atle Kleven have been of invaluable help by building mechanical test devices that made all the measurements possible. Their willingness to help with minor and major problems, often in a hurry is greatly acknowledged.

The rest of the staff at the Department of Biomedical Engineering for good cooperation and technical assistance.

List of Contents

Nomenclature

List of Symbols

a	Transducer radius
c	Velocity of sound
f_m	Frame rate
k_o	Sound wave number
Ω_m	Beam angular velocity, $(2\pi f_m t)$
r	Range, radial distance
ϕ	Beam lateral angle
ψ	Beam azimuthal angle
f	Temporal frequency
f_ϕ	Lateral temporal frequency
$f_{\phi s}$	Lateral temporal sample frequency
f_{rs}	Radial temporal sample frequency
k	Spatial frequency
k_{BSB}	Blood spectrum broadening factor
k_ϕ	Lateral spatial frequency
$K_{\phi Dec}$	Lateral decimation factor
$k_{\phi Max}$	Maximum lateral spatial frequency, stationary scatterers
$K_{\phi OS}$	Lateral oversampling factor
$k_{\phi s}$	Lateral spatial sample frequency
k_o	Wave number for the transducer center frequency
k_{rs}	Radial spatial sample frequency
k_ψ	Azimuthal spatial frequency
N_b	Beam density, number of acquired beams pr. revolution
N_{bDisp}	Beam density in the display unit
N_{bMin}	Minimum beam density to avoid aliasing
N_{OptEnc}	Number of pulses per revolution from the optical encoder
N_r	Number of radial acquired samples per beam
N_{rDisp}	Number of radial samples in display unit
V_B	Blood velocity
V_{Ba}	Angular blood velocity component
$V_{B\phi}$	Lateral blood velocity component
V_{Br}	Radial blood velocity component
$V_{B\psi}$	Azimuthal blood velocity component

Abbreviations

BPDV	Binary Phase Difference Value
CW	Continuos wave
DSPU	Digital Signal Processing Unit
Log-amp	Logarithmic amplifier.
LPDM	Lateral Phase Difference Magnitude
LVWD	Lateral Vessel Wall Detector
MDU	Motor Drive Unit
MEM	Memory device
NEB	Noise Equivalent Bandwidth
NURD	Non Uniform Rotation Distortion
PDUV	Phase Difference Unit Vector
PDVWD	Phase Difference Vessel Wall Detector
Pre-amp	Pre-amplifier
PRF	Pulse repetition frequency.
PSF	Point Spread Function.
PW	Pulsed wave
QD	Quadrature Demodulator
RD	Reverberation Detector
RPDM	Radial Phase Difference Magnitude
RVWD	Radial Vessel Wall Detector
RX	Receiver
SNR	Signal to noise ratio
TGC	Time Gain Compensation
TX	Transmitter
XD	Transducer

Chapter 1

INTRODUCTION

Intravascular ultrasound imaging is a technique for generating cross section images both of blood vessels and in the immediate vicinity of them. In contrast to optical systems, this technique penetrates through the vessel wall and makes it possible to see the vessel wall thickness and to a certain extent localize plaque. Other biological channels than blood vessels can also be imaged as long as there is an acoustic path between the catheter and the vessel wall. A water filled balloon may serve this purpose.

In the arterial tree, this method is used to diagnose atherosclerosis in the peripheral and coronary vessels. A cross section imaging system is well suited for inspecting the vessel prior to and after balloon angioplasty, if the size of the catheter makes it possible to gain entry through the occlusion. When a cross section ultrasound imaging catheter cannot be entered through a stenosis, a forward looking catheter would be beneficial, ideally a three-dimensional scanning system. A combined forward looking ultrasound and laser atherectomy catheter would be a powerful tool in opening up occluded vessels. However, a standard procedure based on this method is at its best, still some years in the future.

1.1 Methods of intravascular ultrasound imaging

1.1.1 Scanning methods

Two-dimensional intravascular ultrasound imaging is performed by entering a tiny catheter into a vessel and scanning an ultrasound beam 360 degrees around the catheter axis at the tip. A cross section image is generated and the echo from blood cells, vessel walls, plaque and tissue structures is converted to a gray scale light intensity and displayed on a screen in the same way as in radar systems. See Figure 1.1.

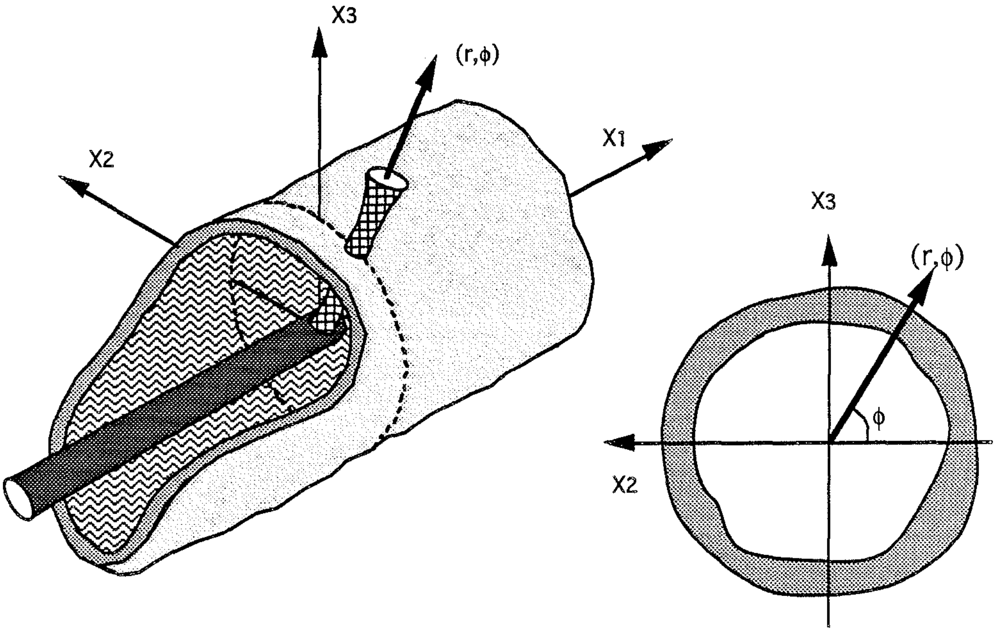

Figure 1.1 *(a) Intravascular ultrasound scanning method: A catheter is entered into the vessel and a 360 degree cross section image is generated.*
(b) Cross section view of the vessel in the ultrasound beam scan plane.

The most common methods of scanning the ultrasound beam at the tip of the catheter are shown in Figure 1.2. Catheters based on these designs are denoted:

(a) *"Rotating transducer catheter":* The transducer is mounted on a flexible wire which rotates inside a protecting tube.

(b) *"Rotating mirror catheter":* The transducer is fixed and directed towards the proximal end of the catheter. A rotating mirror reflects the beam. A thin heat scrink covers the distal housing.

(c) *"Rotating transducer and mirror catheter":* The transducer and a mirror are both mounted on a rotating flexible wire which rotates inside a protective tube.

(d) *"Curvilinear array catheter":* A curvilinear array at the tip of the catheter allows electronical beam steering with no moving parts.

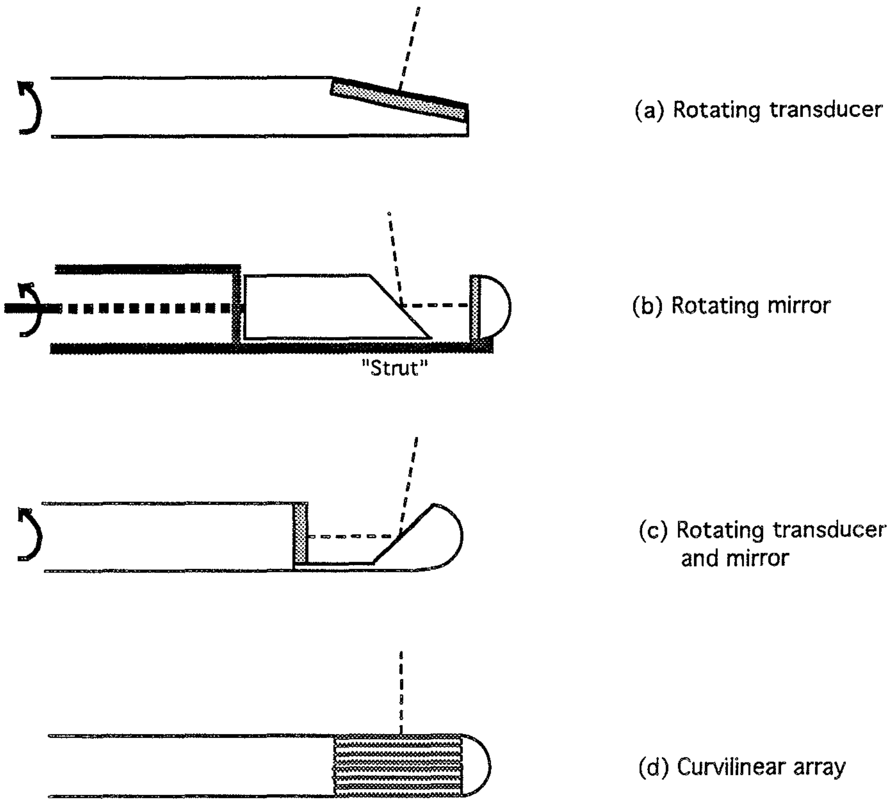

Figure 1.2 *Four different catheter designs. Beam scanning is accomplished by mechanical rotation in (a), (b) and (c), and by electronic beam steering in (d). The catheters in (b) and (c) use a mirror to reflect the beam. In some catheters the beam is tilted in the azimuthal direction as indicated in (a), (b) and (c).*

During transmission, the receiver will be saturated and needs a certain time to return to linear operation. This causes a dead region in the very near field (≈1 millimeter) of the catheters in Figure 1.2(a) and (d). The other two catheters have a water path that causes the receiver to be fully operable at the surface of the catheter.

In the *rotating mirror* and the *rotating mirror and transducer* catheters, the transducer is radiating in the catheter axial direction. This means that the transducer size determines the catheter cross section. The other two catheters radiate approximately perpendicular to the axis which means that the transducer *width* is limited by the catheter size, while the transducer *length* is not. In the far field, the beam width is inversely proportional to the aperture of the transducer. This means that the azimuthal resolution (the thickness of the scan plane) can be better than the lateral resolution. In order to take advantage of this effect, the transducer should be focused. Otherwise the far field properties will lie outside the imaging region of interest.

In some of the catheters the beam is slightly tilted towards the proximal or the distal end of the catheter, i.e. in the azimuthal direction. The primary reasons for tilting the beam are to obtain better reflection at the mirror surface and/or to introduce a Doppler shift in the spectrum from blood. Some of the blood noise can be reduced by frequency selective filtering.

Peripheral and coronary arteries are small in dimension, ranging from ≈5mm in diameter to some micro meters. To get access to as many vessels as possible in the arterial tree, the diameter of the catheter should be as small as possible. But as the dimension is reduced, the requirement to high frequency ultrasound increases in order to maintain high resolution. In intravascular imaging, frequencies in the range 10 to 45 MHz are currently used [Foster 1991], [Yock 1989], [Wiersema 1989]. The trade-off between resolution and penetration makes it necessary to select catheter dimensions and frequency to the specific application. In peripheral arteries, catheters sized between 8F (Ø 2.4mm) and 5F (Ø 1.5mm) are commonly used. In coronary arteries sizes around ≈5F are used.

The length of the catheter should also be selected to the specific application. In order to reduce the electromagnetic susceptibility, the catheter should be kept as short as possible, typical length is ≈0.5m to ≈1.3 m.

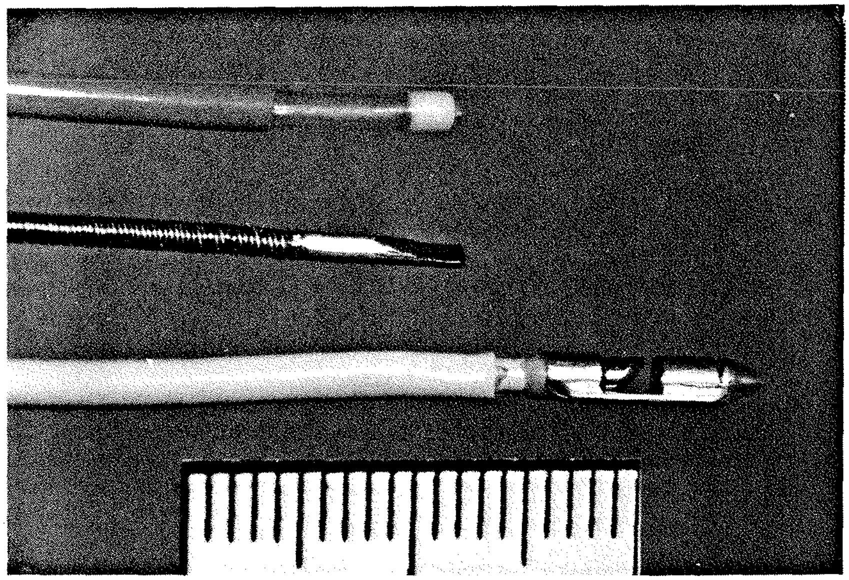

Figure 1.3 *Upper panel: "Rotating transducer catheter" (6.2F) from Boston Scientific. The center wire with the transducer is pulled out of the protecting tube.*
Lower panel: "Rotating mirror catheter" (8F) from Cardiovascular Imaging Systems.

The distal tip of a *rotating transducer catheter* and a *rotating mirror catheter* is shown in Figure 1.3. The upper panel illustrates the protecting tube and the flexible wire from the former type (6.2F, Boston Scientific, Boston). In the lower panel the latter type is shown (8F, Cardiovascular Imaging Systems Inc., California). The resolution of the ruler is 1mm.

1.1.2 Instrument block diagram

An intravascular imaging system can be described by the block diagram in Figure 1.4. Apart from the catheter, it consists of an *adapter* or *Motor Drive Unit* (MDU) and an *imaging instrument*.

Adapter/motor drive unit: Whether the catheter is based on curvilinear array or mechanical scanning, it has to be connected electrically and mechanically to the imaging instrument. A small hand-held device may serve this purpose. It should be connected to the instrument with a flexible cable long enough to bring the instrument out of the sterile zone. If the adapter is not sterilizable, it should be covered by a sterile plastic bag. Since the cable needs to be several meters long, it is preferable to include a pre-amplifier and a transmit power amplifier in this device (to reduce interference and power loss).

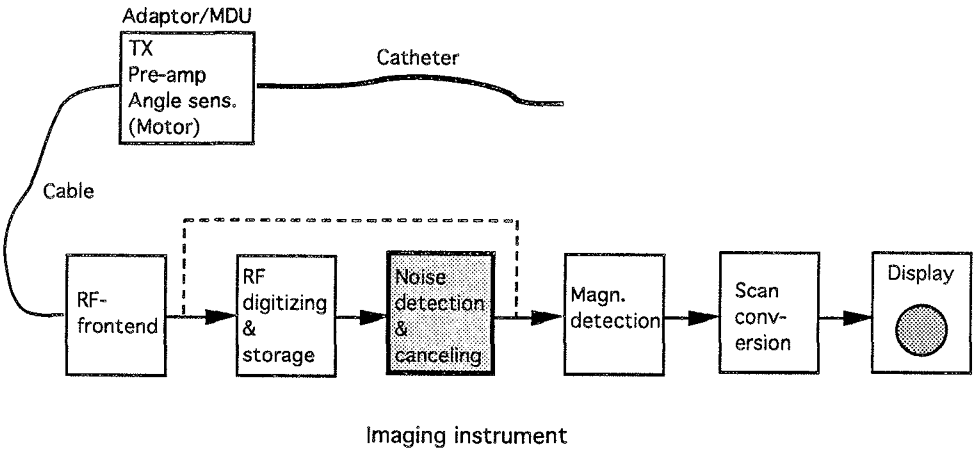

Figure 1.4 *Block diagram of an intravascular imaging system consisting of a catheter, an adapter with cable and an imaging instrument.*

The image is constructed by sending a fixed number of evenly spaced pulses per revolution. With a *curvilinear array catheter*, the beam can be steered electronically. The other catheter types require a motor to rotate the transducer and/or mirror. Ideally an angle sensing device should be located at the *distal tip* of the catheter, and the signal from this device should be used to trigger the transmitter. Due to the difficulties (and cost) to realize this situation, a simpler solution is currently used: An optical angle decoder is connected to the *motor shaft*. If the mirror and/or transducer angle does not follow the motor shaft exactly (due to friction and elasticity in the drive wire), geometric distortion of the image occurs.

Imaging Instrument: The purpose of the imaging system is to generate the transmit pulses in the directions given by the angle sensor and to convert the received signals into gray level light intensity beams in the corresponding locations on the monitor. A straight forward solution is shown in Figure 1.4 where the frontend signal is fed directly to a magnitude detecting device (dashed line) and thereafter scan converted and displayed.

Fast AD-converters make it possible to digitize and store the RF signal (both amplitude and phase). This opens the way for digital signal processing capabilities which cannot be done with the analog signal. Many different digital signal processing algorithms can be implemented in order to improve image quality or extract special information from the signal. Image quality improvement in terms of noise reduction will be treated in this work. The shaded block in Figure 1.4 indicates where noise detection and canceling can be performed in the signal path.

Due to propagation delay through the system, there will be a certain time lag between sampling and display. A delay corresponding to several beams is not noticeable to the user. Even a few frames (1-3) may be acceptable, depending on the frame rate and the application, i.e. non-causal filtering is possible.

The instrumentation used in this work is described in Chapter 3.

1.1.3 Ultrasound RF-image signal

The received ultrasound signal is described in three coordinates: The range or depth parameter "r", the lateral angle "ϕ" and the frame number "m". If the catheter is fixed in the vessel, the frame number is the representation of *time*. If the catheter is moved along its axis, the frame number will represent a third spatial dimension of the vessel. In this thesis, the catheter is assumed to be fixed so that the frame number represents a temporal parameter.

The *ultrasound image signal* can be denoted: $S_u(r,\phi,m)$. This signal is assumed to contain the desired signal "$S_{desired}$" plus noise. Assume that the system is linear and that only blood noise, catheter reverberations and electronic noise are considered. The ultrasound image signal can be written:

$$S_u = S_{desired} + N_{blood} + N_{rev} + N_{elect.noise} \tag{1.1}$$

The goal of this work is to find methods to reduce these three noise signals without degrading the desired signal significantly. The spatial and temporal correlation properties of signal and noise are important in order to discriminate noise. These correlation properties are given by the auto correlation function:

$$E\{\, S_u(r,\phi,m) \;\; S_u^{*}(r+\Delta r,\phi+\Delta\phi,m+\Delta m)\,\} \tag{1.2}$$

The ultrasound image signal is digitized and stored in memory. This makes it possible to process the data along the following three coordinates: radially (sample to sample), laterally (beam to beam) and temporally (frame to frame). Signal and noise have different correlation properties along one or more of these coordinates.

Data acquisition time is limited by the velocity of sound and the penetration depth. This means that there is a relation between *time* and the three coordinates. The relations are given by: $r = {}^{c}/_{2}\, t$, $\phi = \Omega_m t$ and $m = \mathrm{INT}\,\{f_m t\}$ where Ω_m is the beam angular velocity, INT{.} represents the integer part and f_m is the frame rate. In order to obtain all information in the signal during sampling, the following realistic sample frequencies are used: radial sampling frequency $f_r \approx 5$ to 50 MHz, lateral sampling frequency $f_\phi \approx 1$ to 100 kHz and the temporal frame rate $f_r \approx 1$ to 50 Hz.

The statistics of the ultrasound image signal will lie somewhere between the following two extremes:

1) A stochastic Gaussian distribution (due to scattering from a large amount of randomly distributed small scatterers or due to uncorrelated Gaussian noise).
2) A deterministic signal given by the echo from a specular reflector (the catheter housing or a smooth vessel wall surface).

In *radial direction*, all signals have passed the same band-pass filter. There isn't much that can be done in order to distinguish the Gaussian signals (blood) from Gaussian noise (sensor and amplifier noise). Tissue structures will exhibit a combination of the Gaussian stochastic and the deterministic statistics. It has been shown by Wagner, Insana and Brown [Wagner 1986], [Wagner 1987], [Insana 1986] that in some cases it is possible to classify ultrasound image texture by analyzing the first and second order statistical properties in radial direction. Tissue consisting of randomly distributed small scatterers will yield a Rayleigh distributed amplitude. Adding a distribution of large specular scatterers causes the amplitude to be approximately Rician-distributed.

In some cases, catheter reverberations can also be detected by cross correlating the received radial signal with a deterministic pulse, equal to what is received from a specular reflector.

The lateral or *beam to beam mode* and the temporal or *frame to frame mode* yields more information about the signal and noise properties. This thesis describes methods to analyze the signals in both domains. Noise reduction by linear filtering and by detection and canceling is described.

1.2 Acoustic and electronic noise

Noise is defined as signals that by some means reduce the image quality. Some noise signals are caused by external equipment (electromagnetic interference), some because of limitations of the imaging equipment (sensor and amplifier noise, side lobes and catheter reverberations), some due to the actual imaging situation (side lobes and tissue reverberations) and some are due to undesired targets in the image field (red blood cells and gas bubbles due to laser ablation).

The noise sources can be grouped in acoustic and electronic noise. A major difference between the two is that the relative contribution from electronic noise can be reduced by increasing the transmitting power. This is not the case for acoustic noise.

1.2.1 Blood and laser noise - The object noise

The signals from blood and gas bubbles are passed through the system in the same way as all desired signals. From an imaging point of view, these signals are treated as *objects* equivalently to the vessel wall. However, being *undesired objects*, they are consequently defined as noise.

Blood noise: As the ultrasound frequency "f_0" is increased in order to improve resolution, the back scattered signal from blood increases as well. It is primarily the red blood cells that contribute to the back scattered signal from blood. These cells are shaped like discs with concave sides, approximately 2μm thick and 7μm in diameter.

According to Kino [Kino 1978, page 310], back scattered signal from a *rigid sphere* with diameter 7μm located in a liquid will follow the classical Rayleigh scattering for frequencies less than 35 MHz. The back scattered *power* from many such scatterers will be proportional to the fourth power of the ultrasound frequency: The difference in received power at 10 MHz and 30 MHz from such scatterers will be 19 dB.

Rayleigh scattering will be assumed for red blood cells up to 35 MHz. Practical imaging confirms a high frequency dependent scattering from blood. This effect is demonstrated in Figure 1.5 where three images at different system frequencies are shown. The images are collected under different conditions and cannot be treated as a quantitative comparison of the frequency dependency. The only purpose is to illustrate the effect that: at 10 MHz there is no problem with blood noise. At 20 MHz, blood noise is visible and reduces the contrast between the blood and the vessel wall. At 30 MHz, the blood noise is a significant problem and it is difficult to distinguish the vessel wall from the blood noise.

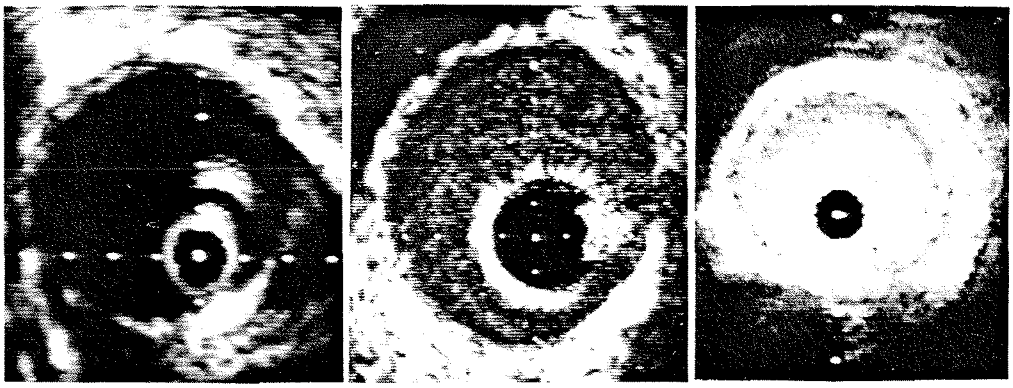

(a) (b) (c)

Figure 1.5 *(a) 10 MHz image of pig ascending aorta. Blood noise is invisible. (Rotating mirror catheter, Cardiovascular Imaging Systems)*
(b) 20 MHz image of pig ascending aorta. Blood noise is visible. (Rotating mirror catheter, Cardiovascular Imaging Systems)
(c) 30 MHz image of human iliac externa. Blood noise represents a major problem. (Rotating transducer catheter, Boston Scientific)

Laser ablation: Early experiments with an Excimer laser at the Department of Biomedical Engineering (Trondheim, Norway) indicate that there was major gas bubble generation during ablation laser. This appears on the screen as bright clouds moving quite slowly. A typical appearance is shown in Figure 1.6(a). The setup is illustrated in (b) except that the laser catheter is located behind the ultrasound scan plane (it is not visible in the image). A cadaver artery was opened and imaged with a 20 MHz *rotating mirror catheter* in a water tank. A laser catheter was directed towards the vessel at the 7 o'clock position, and a *pear shaped bubble distribution* appeared during ablation. The bubbles moved slowly to the surface of the water (upwards).

During laser ablation, the vessel will be flushed with a saline solution. This will remove the bubbles from the ultrasound image field to a certain extent. The time it takes to "clear the sight" *after* an ablation depends on the volume flow, velocity and direction of the flushing. But during ablation, bubble generation cannot be avoided. If it is required or desirable to have a bubble free image *during* ablation, some bubble noise rejection algorithm would be beneficial.

Gas bubbles are compressive, and Kino [Kino 1978] shows that the back scattered signal from a small air bubble in a liquid is 77 dB stronger than the scattering for a rigid sphere of the same size (small compared to the wavelength). Laser noise is much stronger than blood noise, but is otherwise comparable. The bubbles primarily follow the blood flow.

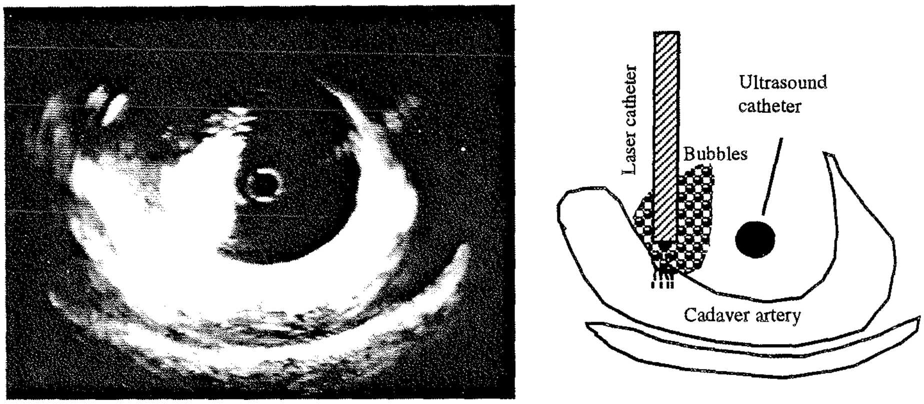

(a) (b)

Figure 1.6 *(a) Laser ablation in arteries generates gas bubbles which appear as a strong noise cloud in the ultrasound image.*
(b) Illustration of the setup. The laser catheter was directed towards the cadaver artery close to the ultrasound scan plane. The laser catheter was not located in the scan plane.

1.2.2 Reverberations

The desired signal from *objects* is characterized by *one single* reflection. Signals that undergo multiple reflections are denoted reverberations. Tissue reverberations are multiple echoes between two biological structures or between the transducer and a biological structure. Catheter reverberations are multiple reflections between the transducer and a catheter part or between two catheter parts.

Tissue reverberations do not appear to be a problem in intravascular imaging due to high attenuation and the geometry. Catheter reverberations are a significant problem. The reverberations can be ranked in the following order according to their apparent noise effect, see Figure 1.2:

> ***Mirror leakage reverberation:*** Some of the side lobe energy may not hit the mirror. A signal that "leaks" outside the mirror may be reflected back to the transducer by mechanical parts in the catheter distal housing. Misalignment of the mirror may cause these reverberations to be angle dependent. The appearance is rings or sectors of rings in the near field of the image.
>
> ***Strut reverberation:*** When the beam hits the "strut" in the *rotating mirror catheter*, the signal will bounce back and forth between the strut and the transducer. Multiple bright clouds appear in the ultrasound image.
>
> ***Protecting tube reverberation:*** The protecting tube around the three catheters with rotating parts will reflect some signals due to change in acoustic impedance between the saline solution (which fills the distal housing), tubing material and blood. This noise will appear as rings or sectors of rings in the near field of the image.
>
> ***Internal mirror reverberations:*** If total reflection at the mirror surface is not obtained (due to surface smoothness and the mirror angle), some acoustic energy may be transmitted into the mirror, undergo some multiple reflections inside the mirror and/or drive wire and return to the transducer. This will appear as small weak noise "clouds" in the near field of the image.
>
> ***Tissue reverberations:*** It is most likely that the vessel wall surface and the transducer cause visible tissue reverberations. The appearance will be a second description of the vessel wall in a depth twice the original depth. This depth is often outside the visible or at least the interesting field.

Figure 1.7 illustrates typical *strut reverberations* and *mirror leakage reverberations* from a *rotating mirror catheter*.

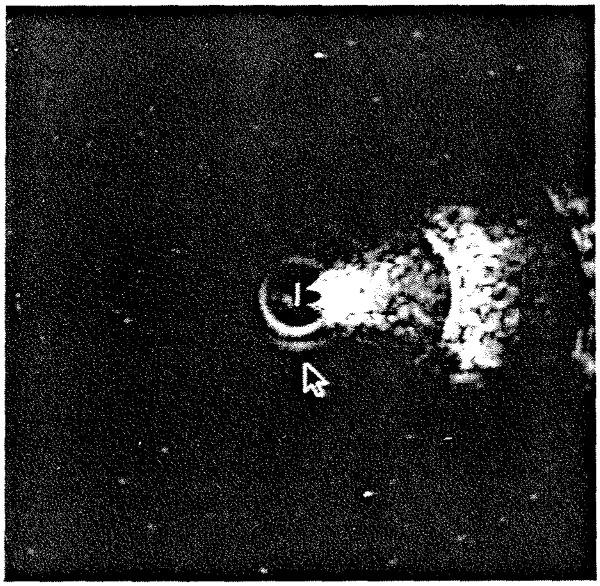

Figure 1.7 *Image illustrating "**strut reverberations**" (right) and "**mirror leakage reverberation**" (arrow) from a rotating mirror catheter (Cardiovascular Imaging Systems)*

1.2.3 Side lobes

Signals from side lobes represent a major limitation to the contrast resolution of the image. A logarithmic far field radiation diagram for a circular transducer excited by Continuous Waves (CW) is illustrated in Figure 1.8. It illustrates the general situation that distinct side lobes always appear outside the main lobe with CW-excitation. A tradeoff between main lobe width and side lobe levels can be made by appodization.

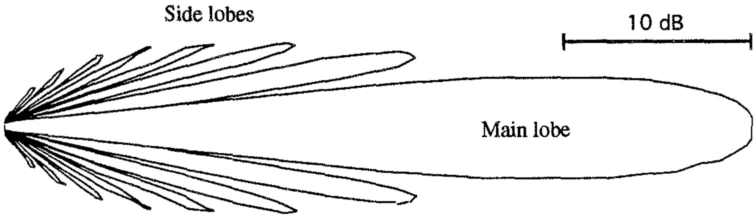

Figure 1.8 *Logarithmic far field radiation diagram for a flat circular transducer excited uniformly with continuous waves. The ratio of the radius to the wavelength is 5, yielding a 14 degree main lobe opening angle.*

The contribution from side lobes is particularly visible in the image when the main lobe is located in a region with weak scattering (for example in a blood region at low system frequency) while side lobes pick up signals from a strong scattering (a vessel wall or calcified plaque). A black region is supposed to be displayed, but a weak signal is received and displayed.

1.2.4 Uncorrelated electronic noise

The two major uncorrelated noise signals are thermal sensor noise and intrinsic amplifier noise.

Sensor noise is due to thermal molecular activity in the transducer and the acoustic medium it is connected to. The available sensor noise power is proportional to the absolute temperature and the bandwidth.

Amplifier noise is primarily caused by electrons crossing a potential barrier. This noise is denoted *shot noise* and is proportional to the DC-currents in the transistors and the bandwidth of the system. The total noise factor of a cascaded system is primarily determined by the noise factor of the first stage (if the gain of this stage is high). The pre-amplifier has 30dB gain which means that this device should be carefully designed in order to minimize the noise factor of the entire system.

These noise sources can be viewed as one Gaussian distributed white noise source. The penetration limit of the system is given by the depth where the desired signals disappear in sensor and amplifier noise.

1.2.5 Electromagnetic Interference (EMI)

Electromagnetic interference (EMI) is electromagnetic radiation that interferes with the desired signal. The EMI-source can be the ultrasound imaging system itself or other equipment. The instrument contains a large number of fast digital electronic components. They are interconnected with relatively short leads on each board, but the boards are connected with longer leads on a bus. High clock frequencies and more or less random digital activity with steep edges generate *broad band noise*. This radiation can be picked up by the catheter and be amplified together with the desired signal if it falls within the instrument pass-band. This noise will appear on the screen as totally random white noise or as random noise with some structural (deterministic) information. The reason for this is that digital activity (bus transfer for example) may in some occasions be in synchronism with image generation in the radial, lateral or temporal directions.

External equipment may also radiate. The most troublesome equipment is one that is *supposed* to radiate, i.e. communication transmitters. These are characterized by a *narrow band signal*. If this signal falls within the transducer pass band, it will add to the desired signal and distort the image. If the interference is so strong that it dominates over ultrasound signal, a homogeneous bright image will appear on the screen. If it is comparable with the desired signal, constructive and destructive interference will occur, thereby resulting in a distorted image.

1.3 Outline of the thesis

Chapter 2 describes a model for the RF-signal. A physical visualization of a typical intravascular ultrasound beam is performed, and an expression for the power spectrum in the lateral direction is found. This result is used to model the power spectrum from stationary vessel wall, pulsating vessel wall and blood. The effect of the log-amp on the signal is demonstrated for a single point scatterer.

Chapter 3 describes the instrumentation and the equipment used in this work. Some measurements to verify the model in Chapter 2 are also presented.

Chapter 4 describes noise reduction for uncorrelated electronic noise, mirror leakage reverberations and blood noise.

Section 4.1: An overview of noise signal properties is given, including methods to reduce the noise by *design changes* and methods to reduce the noise by *signal processing*.

Section 4.2: By tilting the ultrasound beam in the azimuthal direction, a Doppler shift from blood is introduced. Sampling the signal in the lateral direction, the spectrum from vessel wall scatterers will be centered around zero frequency, while the spectrum from blood cells will be shifted proportionally to the blood velocity. A lateral low-pass filter, implemented in each depth location of the image, will reject a certain fraction of the blood noise, while vessel wall signal is unaffected. This method is shown to be effective for high blood velocities, i.e. velocities exceeding several decimeters per second.

Section 4.3: This section describes how uncorrelated electronic noise can be reduced by lateral oversampling and low-pass filtering. The penetration depth is only a few centimeters in intravascular ultrasound imaging. This allows high pulse repetition frequency: PRF≈80kHz at 30 MHz system frequency and PRF≈40kHz at 20 MHz. The corresponding theoretical potential for electronic noise reduction is 10.4dB and 13.6dB respectively.

Section 4.4: *Mirror leakage reverberations* are characterized by a constant distance from the transducer to the reflector. The phase of the signal from a reverberation will be constant. It is shown that this can easily be detected and compensated for in the lateral direction when no other signal than electronic noise is present.

Section 4.5: Signals from blood are normally uncorrelated from frame to frame. Vessel wall signals are normally correlated in the spatial domain (radially/laterally). It is shown that signals from blood and vessel wall can be distinguished by these correlation properties. An effective estimator to detect correlation differences is the phase difference between adjacent frames, averaged in the spatial domain. This means that signals from the vessel wall are *detected*, and signals in other regions can be *canceled*. This yields a blood noise canceler which is effective down to blood velocities ≈0.5 cm/sec.

Chapter 5 describes two possible real time implementations of the algorithms in Chapter 4. Section 5.2 provides a functional description of the 4 algorithms described in Chapter 4 and shows that it is *possible* to realize the algorithms with general digital signal processors, although it is not *cost effective*. Section 5.3 presents an efficient and cost effective solution to the *Uncorrelated electronic noise filter* described in Section 4.3 and the *Blood noise filter* described in Section 4.5.

Chapter 2

MODEL AND PROPERTIES OF THE RF-SIGNAL

The purpose of this chapter is to present a model for the RF-signal that can be used in intravascular imaging. The primary need for the model is to describe the *frequency content in the lateral direction* of the stationary vessel wall signal, pulsating vessel wall signal and blood signal. The model is based on analytical expressions, numerical calculations and practical measurements.

A model is presented in Section 2.1 that is valid in the *far field* and *close to the beam axis*. The radial and lateral properties of the signal are separable.

Some typical beam properties are illustrated in Section 2.2 for a flat circular transducer excited uniformly with continuous waves. In the far field and close to the axis, the well known analytical expression of the field is used due to its convenience. It is desirable to use this description in the more realistic situations as well: in the near field and with pulsed wave transmission. Experiments described in Chapter 3 show that this is possible.

A model for the power spectrum in the lateral direction is found in Section 2.3. Three types of signal are considered: signal from a *stationary vessel wall*, a*pulsating vessel wall* and from *blood*. The power spectrum from the stationary vessel wall is found by numerical integration of the analytical expression that is based on the far field/CW-model described in Section 2.2.

A mathematical model for the log-amp is presented in Section 2.4. Since this device is non-linear making analytical analysis difficult, some simple simulations are performed to gain insight to its performance. By simulations, a single point scatterer is traversed through the sample volume in the radial and lateral directions and the signal is displayed. The beam model in Section 2.2 is used. The received log-compressed signal is presented in both the temporal and frequency domains.

Section 2.5 summarizes the most important properties of the model. Throughout this chapter, the main results and conclusions are printed in bold type.

2.1 RF-signal model

2.1.1 Block diagram of frontend

A block diagram of the analog part of the system used in this work is shown in Figure 2.1. It consists of a catheter with a transducer (and mirror), the adapter or motor drive unit with a unipolar pulse transmitter and a broad band pre-amplifier, the RF-frontend and a Quadrature Demodulator (QD). The RF-frontend consists of a noise limiting band-pass filter that is supposed to be no narrower than the transducer bandwidth, a broad band "Time Gain Compensation" (TGC) circuit, a logarithmic amplifier (log-amp) followed by a band-pass filter to remove higher order harmonics and finally a peak detector. The peak detected RF-signal is digitized and displayed in the conventional way. The signal path from the transducer to TGC-output can be modeled as a pure linear gain stage. The log-amp is used to increase the local dynamic range of the instrument, only 8 bits AD-converters are used.

The purpose of the Quadrature Demodulator is to get access to the RF-signal in terms of amplitude and phase information. The real valued band-pass signal is mixed down to a complex signal in the base band by a synchronous detector. Two AD-converters are required, but their speed requirements are lower than is the case with direct sampling. The input to the Quadrature Demodulator can either be the linear signal U_{TGC} or the log-compressed signal U_{Log}. The linear signal U_{TGC} is used unless otherwise noted.

2.1.2 Far field signal model

Angelsen presents a model for the signal from a single point scatterer located in the *far field* and *close to the axis* (within the main lobe) [Angelsen 1991]. A convenient coordinate system for this model in intravascular use is shown in Figure 2.2.

The catheter axis at the tip of the catheter is given by X_1. The *lateral* angle "ϕ" describes the beam rotation and is defined positive in the clockwise direction seen from the proximal end of the catheter. The beam can be tilted slightly in the azimuthal direction "ψ", the positive angle is defined towards the distal tip of the catheter. A conic scan plane is obtained in contrast to a plane disc. The range or depth to the sample volume is denoted "r". Polar coordinates will be used, and the center of the sample volume is given by (r,ϕ,ψ). The symbol " ' " is used to distinguish the coordinates of a *scatterer*, i.e. (r',ϕ',ψ')

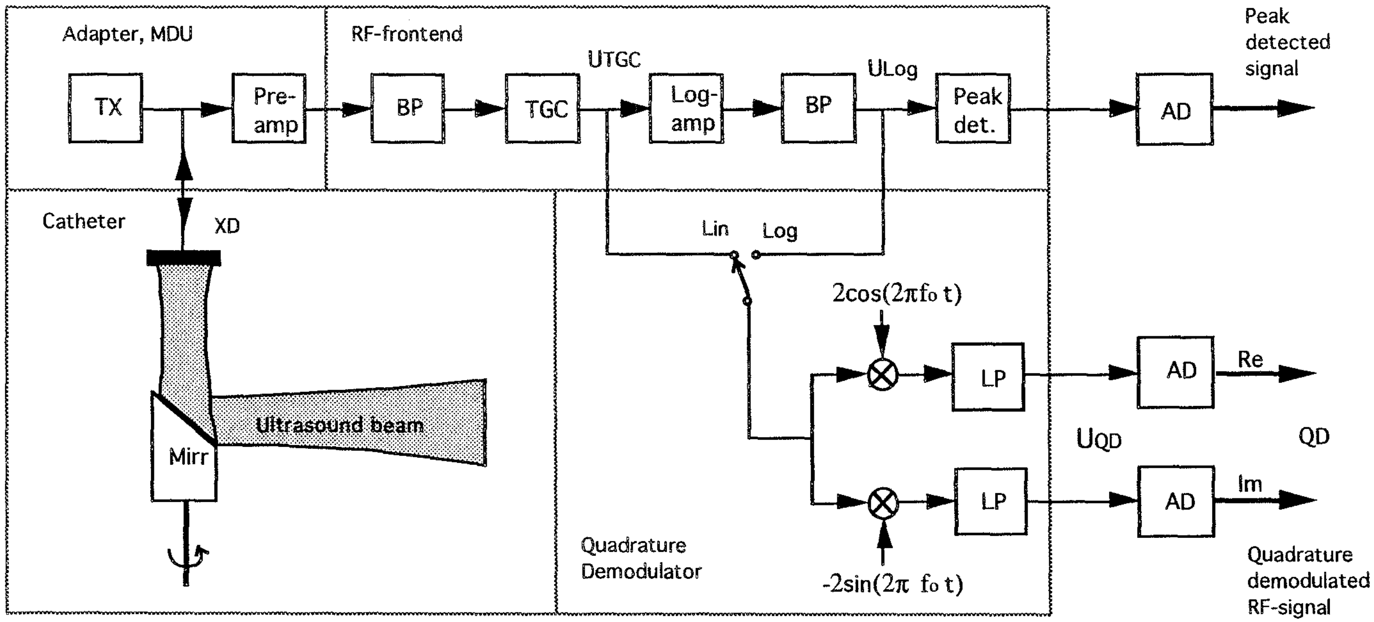

Figure 2.1 *Block diagram of the analog part of the system containing the catheter, adapter, RF-frontend with peak detector and a Quadrature Demodulator.*

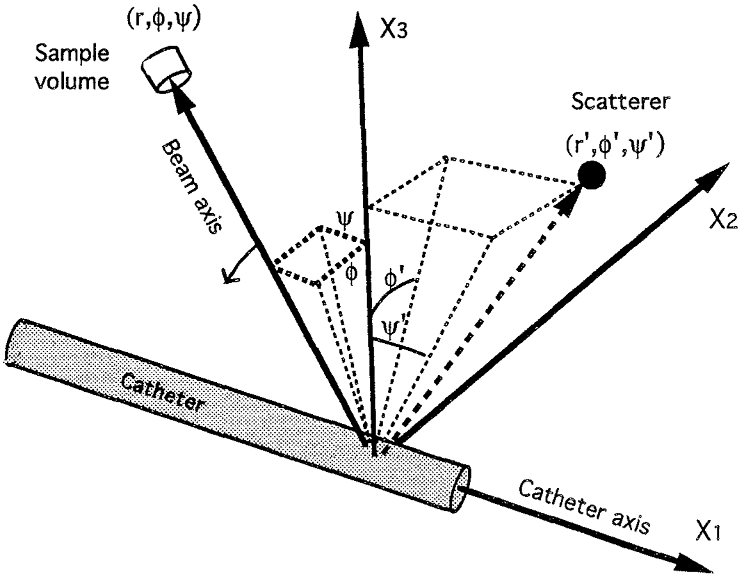

Figure 2.2 *Coordinate system for intravascular ultrasound imaging. The catheter axis at the tip is given by X_1. "r" is range or depth parameter, "ϕ" is the lateral angle (scan direction) and "ψ" is the azimuthal beam tilt angle. The sample volume coordinates are given by (r,ϕ,ψ) and the point scatterer coordinates are given by (r',ϕ',ψ').*

The model presents an expression to the received signal from a point scatterer. It is convenient to express the received signal as the real part of a complex signal. Linear frontend is assumed, and the following signal can be treated as the received single scatterer signal at the output of the TGC-amplifier:

$$g(r,r',\phi,\phi',\psi,\psi') = \mathrm{Re}\left\{ \alpha\, u[\tfrac{2}{c}(r-r')]\; e^{i2k_o(r-r')}\, \frac{1}{r'^2} A(\phi-\phi',\psi-\psi')\,\sigma \right\} \qquad (2.1)$$

α is a gain factor covering the absolute gain of the transmitter, the insertion loss of the transducer, attenuation and the receiver gain.

u[ ] is the complex envelope of the electrical signal received from a point scatterer. The electrical transmit signal is first converted to an acoustic pulse. This pulse propagates and is reflected from a point scatterer (Rayleigh scattering causes frequency dependent scattering: pressure ~ f^2). The reflected pulse is converted back to an electrical signal.

k_o is the wave number ($\omega_o/c=2\pi f_o/c$) determined by the frequency of the transmit signal "f_o" and the velocity of sound "c".

$e^{i2k_o()}$ describes the complex phase of the signal versus range.

r'^{-2} takes care of spherical wave propagation in both directions.

A() is the "two way" angular sensitivity function of the transducer.

σ the *scattering cross section* of the scatterer.

It can be shown by a Fourier transform of Equation 2.1 [Angelsen 1991] that this model represents a *band-pass* signal in *the radial* direction and a *low-pass* signal in *the lateral* (and the azimuthal) direction.

The ***complex envelope*** of the received pulse can be assumed *real valued* under certain conditions. This simplifies the model in that the measured signal phase is given by the exponential term only, i.e. by the scatterer range. In order for "u[]" to be real valued, the total transfer function (in the frequency domain) from transmit signal to received signal should be symmetric. The complex envelope "u[]" is determined by four properties, and the question is when these properties together yield a symmetric frequency response:

1) The electric transmit signal. The transmit voltage is real, the spectrum is symmetric.

2) The transducer frequency response. The frequency shape of a broad band transducer is generally not symmetric, but for narrow band signals it is approximately symmetric.

3) Scattering properties. The back scattered pressure signal is proportional to f^2 for small scatterers ($<<\lambda$) which means asymmetric spectrum, but for narrow band signals the asymmetry can be neglected.
   For very large scatterers ($>>\lambda$) the back scattered pressure is independent of frequency, i.e. symmetric spectrum.

4) When many scatterers are involved, friction losses and scattering losses cause attenuation. Both effects are frequency dependent, and in general the received spectrum will be asymmetric. Again one can assume a symmetric spectrum if the bandwidth is narrow.

The complex envelope term "u[]" can be assumed real valued when the radial bandwidth of the system is narrow. Otherwise it will generally be complex unless the properties in 1-3 add up to a symmetric spectrum.

In the far field and close to the axis, the received signal is separable in the radial and the angular direction. Assume narrow band transducers (fractional bandwidth ≈25%) are used. The envelope "u[]" is assumed to a real valued function.

2.1.3 Point Spread Function

In a linear system, the received signal from a large number of scatterers (in the far field and close to the axis) can be found by summing the contribution from all individual scatterers, i.e. integrating Equation 2.1:

$$g(r,\phi,\psi) = \mathrm{Re}\left\{ \int d^3r' \, \frac{1}{r'^2} \;\; \alpha\, u[\tfrac{2}{c}(r-r')]\, e^{i2k_o(r-r')}\, A(\phi-\phi',\psi-\psi') \;\; \sigma(r',\phi',\psi') \right\} \tag{2.2}$$

This integral is recognized as a spatial convolution between the *Point Spread Function* "$h(r,\phi,\psi)$" of the system and the spatial *scattering distribution* $\sigma(r,\phi,\psi)$:

$$g(r,\phi,\psi) = \mathrm{Re}\{\, [\, h(r,\phi,\psi) \text{ conv } \sigma(r,\phi,\psi)]\,\} \tag{2.3}$$

where the Point Spread Function is defined:

$$\mathbf{h(r,\phi,\psi)} \;\equiv\; \alpha\, \mathbf{u}(\tfrac{\mathbf{2}}{\mathbf{c}}\,\mathbf{r})\, \mathbf{e^{i2k_o r}}\;\; \mathbf{A(\phi,\psi)} \tag{2.4}$$

Since the model is separable in the radial and the angular direction, the Point Spread Function can be written as a radial term "$R(r)$" and an angular term $A(\phi,\psi)$.

$$h(r,\phi,\psi) = R(r)\;\; A(\phi,\psi) \tag{2.5}$$

$$R(r) = \alpha\, u(\tfrac{2}{c}\, r)\;\; e^{i2k_o r} \tag{2.6}$$

2.1.4 Quadrature demodulated signal

The Quadrature Demodulator in Figure 2.1 performs a multiplication of the band-pass signal with an in-phase and a quadrature local oscillator at the same frequency as the transmit pulse "f_o". The products are low-pass filtered to remove higher order products and to avoid aliasing. To minimize electronic noise the low-pass filters should be matched to the transmit pulse. The result of this entire operation is equal to a complex multiplication of the kernel in Equation 2.1 with:

$$2\, e^{-i2k_o r} \tag{2.7}$$

By this complex demodulation, the real valued spectrum is shifted down to a complex spectrum in the base band. The output of the Quadrature Demodulator is:

$$U_{QD}(r,r',\phi,\phi',\psi,\psi') = \alpha\, \frac{1}{r'^2}\, \sigma\, u[\tfrac{2}{c}(r-r')]\; e^{-i2k_o r'}\; A(\phi-\phi',\psi-\psi') \tag{2.8}$$

This equation represents a *low-pass signal* in *the radial* direction and also a *low-pass* signal in *the lateral* (and the azimuthal) direction.

> **The range or depth of the scatterer is described by the phase of $U_{QD}()$ through the exponential term "$\mathbf{R}(r)$" when "u[]" is real valued. This simple relationship makes the Doppler shift analysis simpler.**

2.1.5 Doppler shift, beam tilting

Doppler shift: In Equation 2.8, the phase of the complex signal is given by the range of the point scatterer " r' " (if "u[]" is real valued). For scatterers moving in the radial direction of the beam with velocity "V_r", the range is given by:

$$r' = r'_o + V_r\, t \tag{2.9}$$

where "r'_o" is the range of the scatterer at t=0. Inserting this equation in the phase term of Equation 2.8 yields:

$$e^{-i2k_o r'} = e^{-i2(\frac{2\pi f_o}{c})V_r\, t}\; e^{-i2k_o r'_o} = e^{i2\pi(-2\frac{f_o}{c}V_r)t}\; e^{i\alpha_o} = e^{i\,2\pi f_d\, t}\; e^{i\beta_o} \tag{2.10}$$

where "β_o" is a constant. The Doppler equation for the pulse/echo situation is recognized in the latter expression:

$$\mathbf{f_d = -2\frac{f_o}{c}V_r} \tag{2.11}$$

The output of the quadrature demodulator for a point scatterer (in the far field and close to the axis) can then be written:

$$U_{QD}(r,V_r,t,\phi,\phi',\psi,\psi') = u[\frac{2}{c}(r - V_r t)]\ e^{i\,2\pi f_d t}\ A(\phi-\phi',\psi-\psi') \tag{2.12}$$

(The spherical wave propagation term, the scattering cross section and the gain constant are combined to a single constant, here set to one to simplify the notation. The constant phase "β_o" is set to zero for the same reason.)

This equation expresses a complex modulation in the temporal domain which is identical to a frequency shift in the frequency domain, i.e. a Doppler shift. Due to the pulsed transmit mode, $U_{QD}()$ is only available for discrete time instants.

Velocity components in the radial beam direction: Three kind of movements may cause scatterers to have velocity components in the radial beam direction:

1) Radial dilatation of the vessel wall due to the blood pressure.
2) Blood flow when the beam is tilted.
3) Translation of the catheter tip (perpendicular to the catheter axis) due to viscous forces or vessel walls touching the catheter proximal to the tip.

These velocities are defined in Figure 2.3.

The *radial dilatation* is assumed to be perpendicular to the vessel axis. The vessel wall velocity is a function of longitudinal position "X_l", depth "r", lateral angle "ϕ" and absolute time "t": "$V_{VW}(X_l,r,\phi,t)$" or to shorten the notation: "V_{VW}". It can be decomposed in a radial component directed along the beam axis "V_{VWr}" and an azimuthal angle perpendicular to the ultrasound beam "$V_{VW\psi}$".

The *blood flow* is assumed to be directed in the longitudinal direction, parallel to the catheter axis. By tilting the ultrasound beam in the azimuthal direction, the longitudinal blood velocity "$V_B(X_l,r,\phi,t)$" or just "V_B" can be decomposed in a radial "V_{Br}" and an azimuthal component "$V_{B\psi}$".

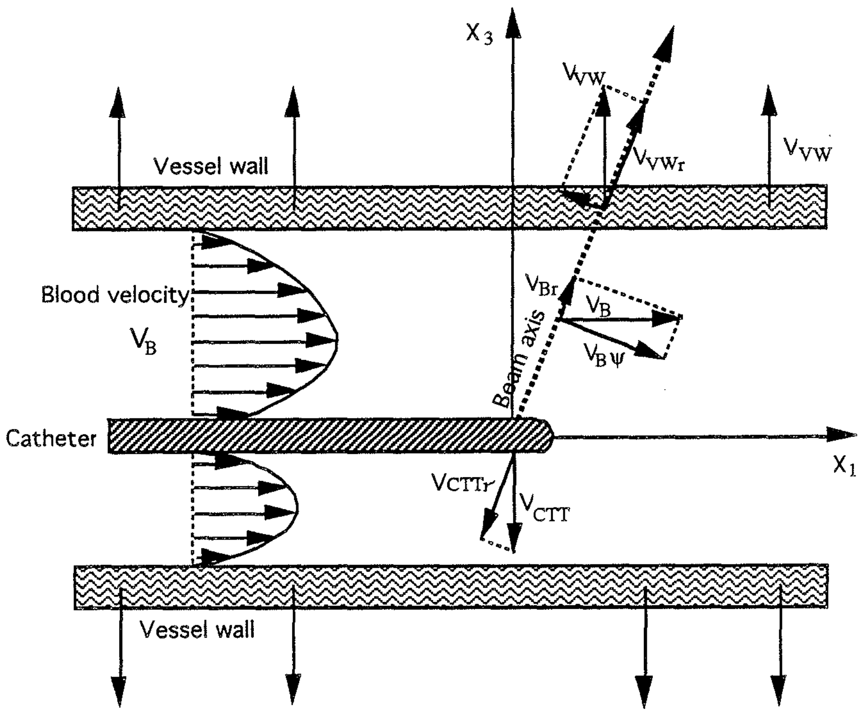

Figure 2.3 *Three kinds of movement cause velocity components in the radial beam direction:*
Blood flow with velocity V_B in the catheter axial direction if the beam is tilted.
Vessel wall dilatation with velocity V_{VW}.
Catheter tip translation V_{CCT} in a plane perpendicular to the catheter axis.
The components of these velocities in the beam radial direction are V_{Br}, V_{VWr} and V_{CTTr} respectively.

Translation of the catheter tip introduces a radial velocity component that depends on the beam lateral angle. If the catheter tip is moving along the X_3 axis when the beam is directed in the X_2 direction, no radial velocity is obtained. In contrast, if the lateral angle of the beam is lined up with the X_3 axis, the catheter tip velocity will cause a maximum radial component. In this case, the maximum radial component due to catheter tip translation "$V_{CTT}(\phi,t)$" (or simply "V_{CTT}") will be "V_{CTTr}".

The radial velocity components versus beam azimuthal angle can be written:

$$V_{VWr} = V_{VW} \cos(\psi) \tag{2.13}$$

$$V_{Br} = V_B \sin(\psi) \tag{2.14}$$

$$V_{CTTr} = V_{CTT} \cos(\psi) \tag{2.15}$$

Beam tilting: By tilting the beam in the azimuthal direction as illustrated in Figures 2.3 and 1.2, a Doppler shift from blood is introduced. The radial velocity is proportional to $\sin(\psi)$. For realistic tilt angles ($\psi \leq 15$ degrees), V_{VW} and V_{CTT} will be reduced negligibly due to tilting. The Doppler equation for blood and vessel wall is then given by:

$$f_{d,Blood} = -2\frac{f_o}{c} V_B \sin(\psi) \approx -2\frac{f_o}{c} V_B \psi \tag{2.16}$$

$$f_{d,VW} = -2\frac{f_o}{c} V_{VW} \cos(\psi) \approx -2\frac{f_o}{c} V_{VW} \tag{2.17}$$

Scatterers moving towards the transducer generate a positive Doppler shift. By selecting the beam tilt angle upstream or downstream, the polarity of the Doppler shift from blood can be selected. The Doppler shift from the expanding vessel wall is always negative.

Catheter translations introduce a Doppler shift that comes in addition to the Doppler shift from the vessel wall and blood. As will be shown in Section 2.3.2, this effect is small and will not be included in the equations for reasons of simplicity.

The situation in Figure 2.3 is idealized. The vessel wall is normally not cylindrical, and the vessel dilatation may not be purely radial to the vessel axis. There can be bends in the vessel or catheter which introduce an angle between the blood flow direction and the catheter tip axis. Turbulent blood flow may also occur. This means that the description in this section is not complete, but may serve as an approximate model to describe the most important effects.

Sampling frequency: In order to extract velocity information from the Doppler spectrum, a proper sampling frequency is required. If the signal is sampled too slowly, aliasing will occur and velocity information is lost. This is the case in the temporal mode (frame to frame), where the sampling frequency is 1-50Hz. If the signal is sampled too rapidly, the signal will contain little or no velocity information. This is the case in the radial mode (sampling frequency: 5-50MHz).

In the lateral direction (beam to beam mode) the sampling frequency is 1-100kHz. By selecting a proper combination of frame rate and beam density, this sampling frequency can be selected to fit the realistic Doppler shifts from blood and vessel walls which are in the range 1-10kHz.

The lateral sampling frequency "$f_{\phi s}$" is given by the Pulse Repetition Frequency (PRF) which is given by the frame rate "f_m" and the number of beams per revolution, the beam density "N_b":

$$f_{\phi s} = f_m \; N_b \tag{2.18}$$

Geometric distortion due to beam tilting: By tilting the beam, data is collected in a slightly coned plane while the image is displayed on the monitor as a flat disc. Structures in the physical sampled image will be "stretched" radially and laterally unless this effect is compensated for by projecting the cone down in the plane. The geometric distortion is given by $1/\cos(\psi)$ which is less than 3.5% for realistic tilt angles ($\psi<15$ degrees). For $\psi=10$ degrees, the geometric distortion is 1.5% which is comparable with other geometrical errors of the imaging system. Compensation is not necessary for tilt angles around this value.

Specular reflection loss by beam tilting: If the vessel surface roughness is small compared to the wavelength, specular reflection will dominate. According to Kino [Kino 1987], this is the case in cardiac and abdominal ultrasound imaging. With a large tilt angle and dominantly specular reflection, only a small fraction of the transmitted power would be reflected back to the transducer. In intravascular imaging, the wave length is $\approx 1/10$ of the wave length in abdominal imaging, so diffuse scattering is expected to play a larger role. With tilt angles in the range $\psi<15$ degrees, power loss by specular reflection is assumed to be negligible.

Vessel wall motion, blood flow and catheter tip translation generate velocity components in the beam radial direction and a Doppler shift is introduced. Frequency analysis in the lateral direction is well suited to extracting the Doppler information from these movements.

2.2 Beam visualization, circular transducer

To get a physical understanding of typical beam properties (dimensions, angles, side lobe levels etc.) in intravascular imaging, some examples will be shown. For illustration a flat circular transducer will be used, excited uniformly with continuous waves (CW). The well known acoustic field and beam properties for this situation is well suited for illustration. It will be shown that the beam properties in the pulsed wave (PW) mode are approximately equal to the beam properties in CW-mode.

2.2.1 Beam profile, near field far field description

Unfocused transducer:
Some important properties of the acoustic beam from a flat circular transducer, uniformly excited with CW is illustrated in: [Angelsen 1991]. The beam will be circular symmetric, and Figure 2.4(a) illustrates the cross section of the beam from a 20 MHz transducer with radius a=0.68mm. A *rotating mirror catheter* is applied to include a water path. (These parameters compare with the ones that are used for practical measurements in this work).

As illustrated in the figure, the acoustic field from the transducer can be divided in three regions:

1) The ***Fraunhofer region or the far field.*** In this region the beam is defined as limited by the cone where the field has dropped 12 dB from the axial value. The region is given by:

$$d_{Fraunhofer} > 2\,\frac{a^2}{\lambda} = \frac{D^2}{2\lambda}$$

2) The ***extreme near field.*** In this region the beam is defined as limited by the cylindrical shadow of the transducer. It is given by:

$$d_{ExtNearField} < 0.8\,\frac{a^2}{\lambda} = 0.8\,\frac{D^2}{4\lambda}$$

3) The region between the *extreme near field* and the *Fraunhofer region* can be denoted the ***transition region.*** In this region the beam will be slightly contracted due to "diffraction focusing".

For this particular transducer and frequency, the two sided opening angle of the -12 dB cone is 6.6 degrees. The extreme near field limit is $d_{ExtNearField} = 4.7$ mm and the far field limit is $d_{Fraunhofer} = 11.8$ mm. The interesting depth of view in intravascular imaging is only a few millimeters.

For a flat circular transducer excited uniformly with CW, the far field region is given by the Fraunhofer region. Practical intravascular imaging is primarily performed in the extreme near field and the transition region.

Focused transducer:
By focusing the transducer or the mirror, the *far field properties of the beam are brought into the focus.* The radius of curvature "F" should be located in the near field in order for focusing to be effective. An example of focusing the same transducer to depth F=4mm is shown in Figure 2.4(b).

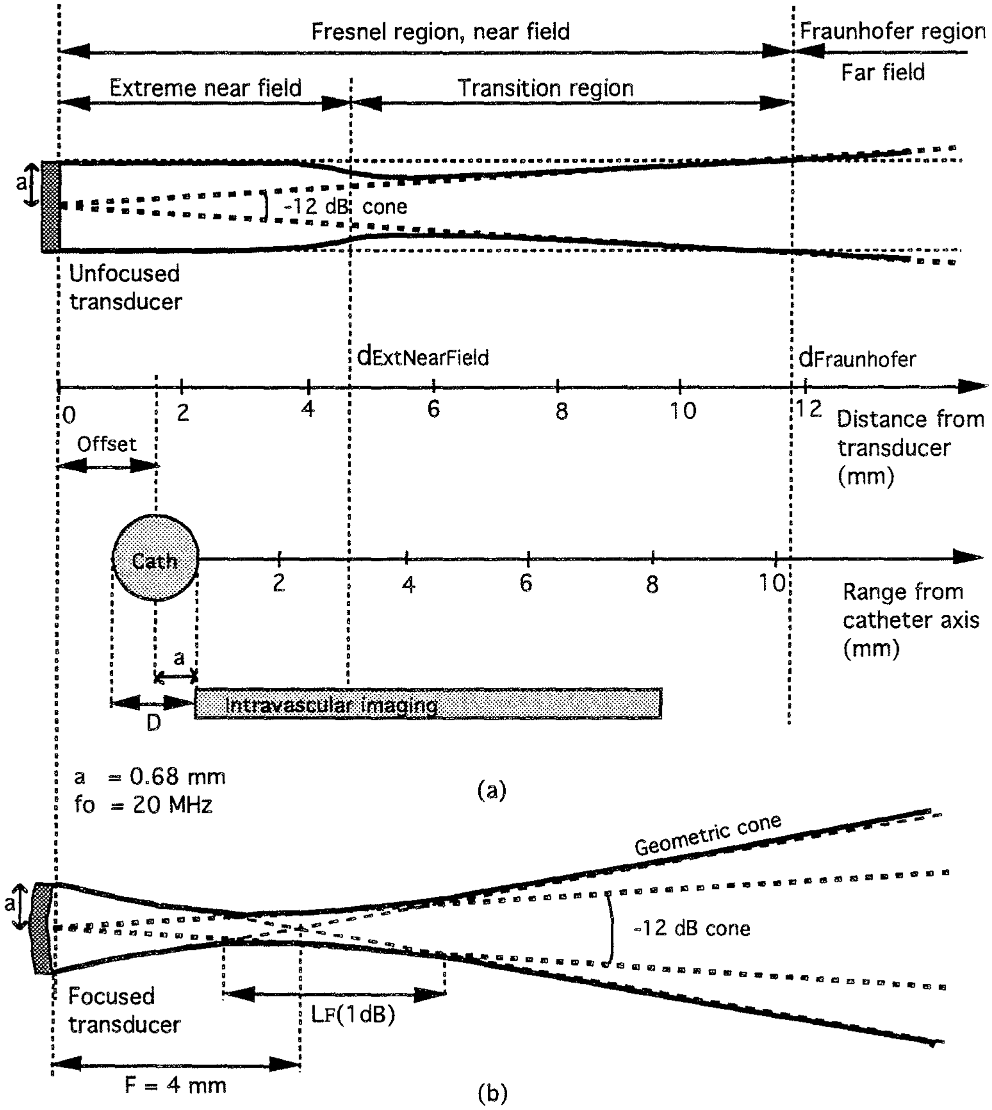

Figure 2.4 *(a) Illustration of the beam profile from a flat circular transducer excited uniformly with CW. The beam can be divided in three regions: The extreme near field, the transition region and the Fraunhofer region. Imaging is normally performed in the near field and the transition region.*
(b) By focusing the same transducer, the far field properties of the beam is brought into focus, and the extreme near field region is shortened. A narrower beam is obtained, limited by the -12dB cone over the focal region LF(1db) that is closer to the transducer. The far field approximation is valid in a realistic imaging range.

The beam profile is now given by two limits: Close to the transducer and far from it (outside the focal region), the beam is limited by the geometric focusing cone. Within the *focal region*, the beam is limited by the diffraction cone which is defined as the previously defined -12 dB cone. The focal region is defined as the region between the two depths where the geometric and the -12dB cone intersects.

The beam diameter defined by the -12 dB cone is:

$$D_{-12dB} \approx \frac{\lambda}{a} r = 2 \frac{\lambda}{D} r \tag{2.19}$$

For the unfocused transducer in Figure 2.4(a) the minimum beam diameter is located ≈ 5.5mm from the transducer and the beam diameter is ≈ 0.7mm. When the same transducer is focused in F=4mm, the minimum diameter is ≈ 0.35mm. The beam width is reduced to half the value of an unfocused transducer.

By focusing the transducer, the far field properties of the beam are brought into the focus. The far field approximation can be applied to a region where practical intravascular imaging is performed. The beam width is reduced to the -12 dB cone in the focal region.

Measurements:
Focusing the beam is one way to make sure that the far field model applies in the imaging region. However, some measurements were performed to check whether focusing is *necessary*. This was performed by measuring the *power spectrum in the lateral direction* from a large amount of stationary scatterers. The test is described in Chapter 3.2.4. It was not possible to register any difference in the power spectrum for scatterers located in the extreme near field and scatterers located in the far field from a flat circular transducer.

For the purpose of modeling the power spectrum in the lateral direction, the measurements in Section 3.2.4 indicate that the far field model can be applied to the near field as well for an unfocused transducer.

2.2.2 Far field angular sensitivity function

The acoustic field from the unfocused circular transducer described previously is complex to describe in the near field and the the transition region. In the far field the following simple analytical expression exists, a so-called "jinc"-function:

$$H_e(\Theta) = \frac{2\,J_1(k_o\,a\sin\Theta)}{k_o\,a\sin\Theta} \tag{2.20}$$

$J_1(x)$ is the Bessel function of the first kind and the first order. "a" is the transducer radius and "k_o" the wave number. "Θ" is the angle between the beam axis and the direction of observation.

The "two way" angular sensitivity function is found by squaring "$H_e(\Theta)$". It represents the transmit/receive sensitivity function for a point scatterer located in an angle Θ relative to the beam. :

$$A(\Theta) = He(\Theta)^2 = [\frac{2\,J_1(k_o\,a\sin\Theta)}{k_o\,a\sin\Theta}]^2 \tag{2.21}$$

The following equation relates the lateral and azimuthal beam and scatterer angles to "Θ":

$$\Theta = \arctan\sqrt{\tan^2(\phi'-\phi) + \tan^2(\psi'-\psi)} \tag{2.22}$$

Equation 2.21 can then be written:

$$A(\phi,\phi',\psi,\psi') = [\frac{2\,J_1(k_o\,a\sin(\arctan\sqrt{\tan^2(\phi'-\phi) + \tan^2(\psi'-\psi)}\,))}{k_o\,a\sin(\arctan\sqrt{\tan^2(\phi'-\phi) + \tan^2(\psi'-\psi)}\,)}]^2 \tag{2.23}$$

"$A(0,\phi',0,\psi')$" is plotted in Figure 2.5(a). The side lobes are so small in this two-way function that they are hardly visible in a linear plot. To get a better view of the beam profile, the one-way function "$H_e(0,\phi',0,\psi')$" is plotted in (b). Note that the odd side lobes are negative in "$H_e(0,\phi',0,\psi')$", while in "$A(0,\phi',0,\psi')$" all side lobes are all positive due to the squaring operation.

> **The angular two way sensitivity function "$A(\phi,\phi',\psi,\psi')$" can be described by an analytical function (the square of a jinc-function) for a flat circular transducer excited uniformly with CW.**

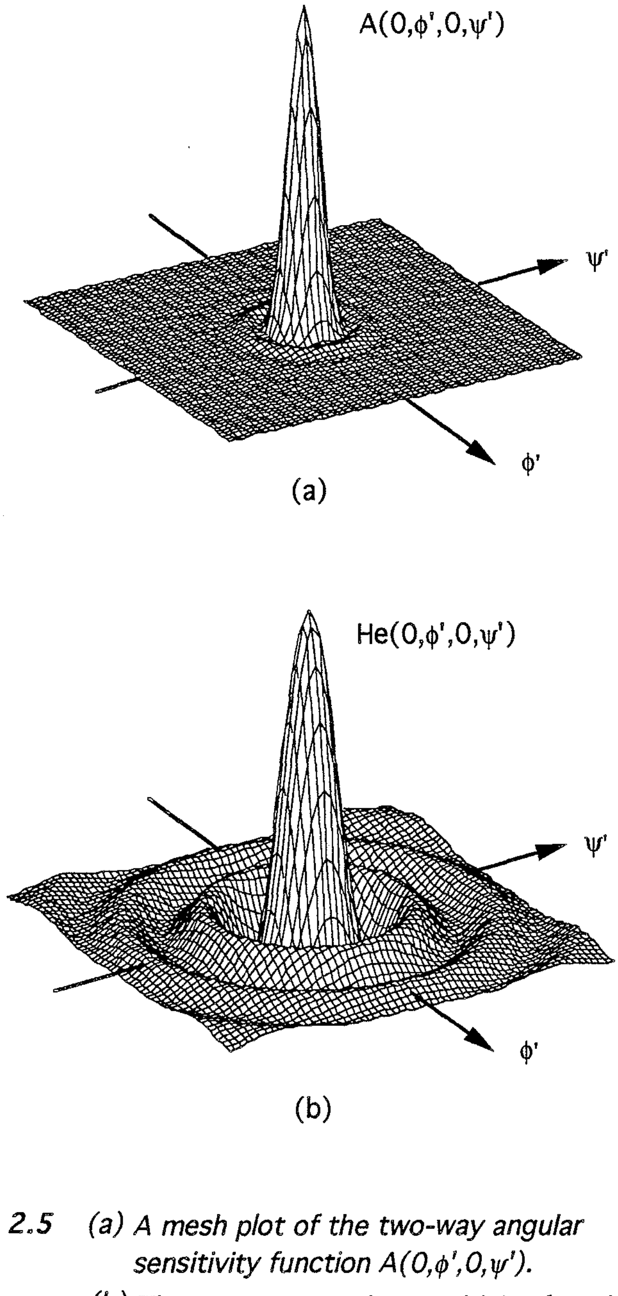

Figure 2.5 *(a) A mesh plot of the two-way angular sensitivity function $A(0,\phi',0,\psi')$.*
(b) The one-way angular sensitivity function $He(0,\phi',0,\psi')$.

2.2.3 Side lobes

The opening angles and the side lobe levels for the angular sensitivity function in Equation 2.21 are visualized in Figure 2.6(a) (as well as the -12 dB cone). The plot represents the far field two way sensitivity function for CW-excitation. The *one sided* opening angle in degrees is given by:

$$\Theta = \frac{180}{\pi} \arcsin\left(\frac{1}{2\pi}\frac{\lambda}{a}\, p_n\right) \qquad (2.24)$$

where p_n is given in Table 2.1. The Table also lists the corresponding *two sided* opening angle $\Omega = 2\Theta$ and the side lobe levels.

Power in side lobes versus power in main lobe:
A numeric integration was performed to get an impression of the power received from the side lobes versus power in the main lobe. We assume that a large amount of small scatterers is distributed randomly in the acoustic far field from a flat circular transducer which is excited uniformly with CW. The two-dimensional spatial power spectral estimate of the scatterer distribution is assumed to be constant. By the Wiener-Khintchine theorem, the received power can be found by integrating the two way angular sensitivity function $A(\phi,\phi',\psi,\psi')$ squared (see Section 2.3.1).

Table 2.1 *Two sided opening angle $\Omega = 2\Theta$ and side lobe levels for the two way angular sensitivity function $A(\Theta)$. (Flat circular transducer excited uniformly with CW at f_o=20MHz, a=0.68mm, c=1560m/sec.)*

	-12dB	1.zero	1.side lobe	2.zero	2.side lobe	3.zero
n	1	2	3	4	5	6
p_n	3.14	3.83	5.3	7.02	8.5	10.17
Ω	6.5deg	8.0deg	11.1deg	14.6deg	17.8deg	21.4deg
$A(\Theta)$	-24.0dB	--	-35.4dB	--	-47.7dB	--

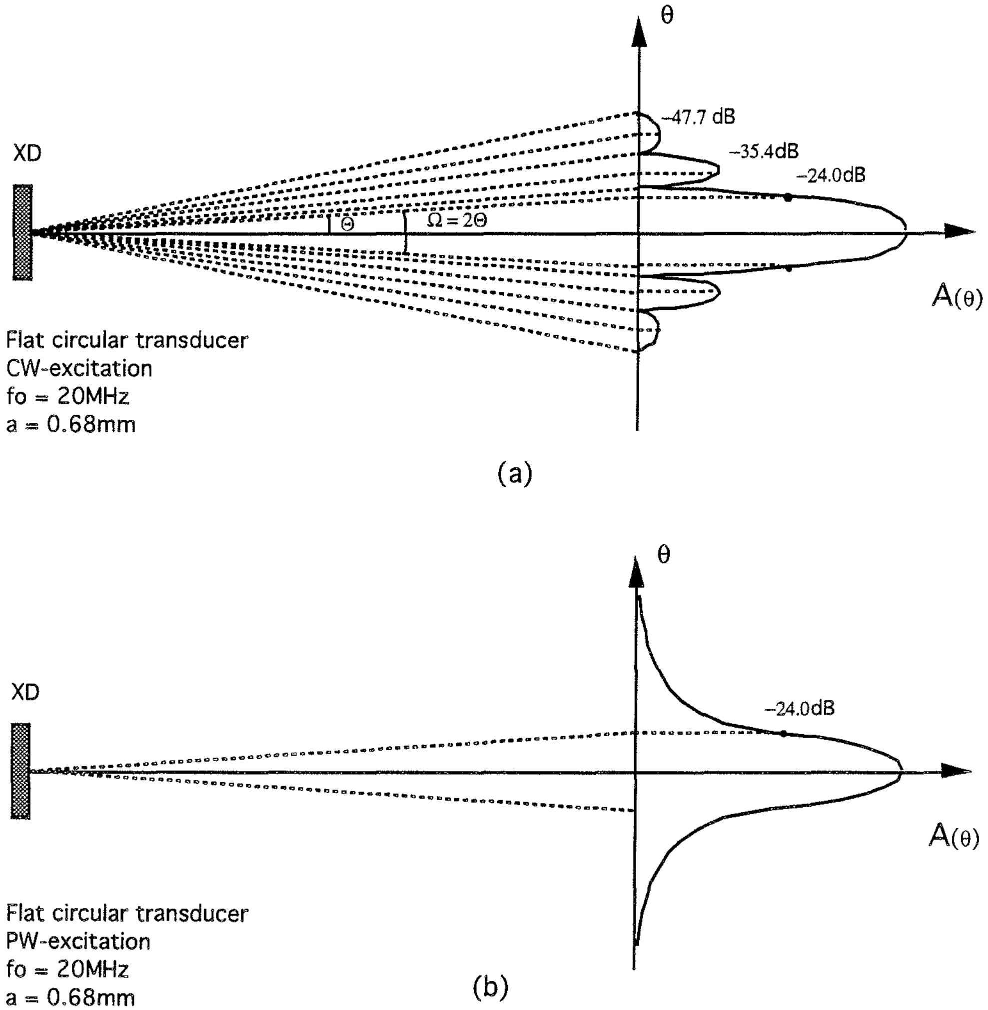

Figure 2.6 *(a) Opening angles for a flat circular transducer excited uniformly by CW (fo=20MHz, a=0.68mm) are illustrated in correct scale. The two way angular sensitivity function A(Θ) is sketched (not correct scale) and side lobe levels are labeled.*
(b) Schematic illustration of the two way angular sensitivity function for the same transducer excited by pulsed waves (PW). The distinct side lobe pattern disappears and a smoother function results.

The received power is given by:

$$\mathbf{P}_{\mathrm{MainLobe}} = \int_{\mathrm{Main\ lobe}} d\phi'\, d\psi'\, |A(0,\phi',0,\psi')|^2 \tag{2.25}$$

$$\mathbf{P}_{\mathrm{SideLobes}} = \int_{\mathrm{SideLobes}} d\phi'\, d\psi'\, |A(0,\phi',0,\psi')|^2 \tag{2.26}$$

The ratio of the power in the main lobe to the power in all the side lobes is:

$$\frac{\mathbf{P}_{\mathrm{MainLobe}}}{\mathbf{P}_{\mathrm{SideLobes}}} = 27\ \mathrm{dB} \tag{2.27}$$

2.2.4 CW / PW-excitation

In high resolution ultrasound *imaging*, i.e. PW-excitation, a short pulse of only a few cycles is transmitted. In the frequency domain this corresponds to a broad spectrum. A transducer with 50-100% fractional bandwidth is regarded as a broad band transducer. Due to linearity, the transmitted pulse can be constructed by an infinite sum of sinusoidal components with amplitude and phase given by the Fourier coefficients. If each of these CW-signals acted alone on the transducer, a far field angular signal strength as illustrated in Figure 2.5(b) would occur (again a flat circular uniformly excited transducer). But the width of the beam would be approximately inversely proportional to the frequency. Adding all the contributions would yield a field that is smoother than in the CW-case. The side lobe pattern is smeared out. The corresponding two way angular sensitivity function is illustrated schematically (without simulations) in Figure 2.6(b). (The CW-situation is shown in (a)).

The near field from a CW-excited transducer is complex to describe. The PW-field is even worse. Hygen's principle states that the signal from a surface can be viewed as the sum of spherical waves emitted from all points on the surface. From an observation point located outside the main lobe and in the near field, the difference in propagation length from different points on the transducer surface will be comparable with the pulse length (short pulse). This means that all the waves can add destructively in the middle of the received pulse, but not at the front and tail. This effect is known as edge waves. The side lobes split to edge waves as a target is brought into the near field.

Measurements:
Since the model presented here is based on CW-excitation, it is desirable to compare CW and PW excitation by measurements. The power spectrum in the lateral direction is of particular interest. Does the spectrum change significantly when going from CW to PW? If the answer is yes, this effect should be included in the model. If the answer is no, the CW-model can be applied for practical PW-imaging.

CW-excitation cannot be realized on the instrument, but the CW-situation was approximated by a high number of pulses in the transmittal burst. Section 3.2.5 describes the test. The number of pulses were changed from 1 to 10 while the measured power spectrum from a large amount of stationary scatterers were calculated. It was not possible to register any changes in the power spectrum versus the number of pulses.

The number of pulses in the transmittal burst did not change the measured spectrum in the lateral direction noticeably. With respect to the power spectrum in the lateral direction, it is assumed that the CW-model can be applied to the PW-excitation mode with negligible errors.

2.3 Power spectrum in the lateral direction

The purpose of this section is to find an approximate description of the power spectrum from the signal sampled in the lateral direction. The signal received from *stationary vessel wall, pulsating vessel wall* and *blood* is treated separately. Frequency dependent scattering and attenuation is *not* taken into account (assume symmetric spectrum, i.e. real valued complex pulse envelope). Stationary vessel wall and blood that is *not* moving are assumed to give identical spectra. The blood velocity causes the transit time to drop, i.e. the spectrum is broadened. In addition, the blood spectrum will be shifted due to the Doppler shift.

2.3.1 Power spectrum from stationary vessel wall

Spatial/temporal frequency:
A noise free ultrasound image signal from a stationary vessel with no catheter movements will in *the lateral direction* be periodic. The received signal in one particular depth is independent of the frame rate "f_m" (also assume that the beam

direction is fixed during sampling). A Fourier transform of the laterally sampled signal yields a frequency domain description where the spatial frequency variable is denoted "k_ϕ" (dimensionless). The lateral spatial sampling frequency "$k_{\phi s}$" is given by the angle between adjacent beams "α_ϕ" which is given by the beam density "N_b":

Lateral *spatial* frequency: k_ϕ

Lateral *spatial* sampling frequency: $$k_{\phi s} = \frac{2\pi}{\alpha_\phi} = N_b \qquad (2.28)$$

The lateral signal can also be treated as a *temporal* signal. In the frequency domain it will be described by the lateral temporal frequency "f_ϕ". The corresponding lateral sampling frequency is given by the time interval between adjacent beams which is denoted "T_ϕ" and determined by the frame rate "f_m" and the beam density "N_b":

Lateral *temporal* frequency: $f_\phi = [1/s]$

Lateral *temporal* sampling frequency/
Pulse repetition frequency (PRF): $$f_{\phi s} = \frac{1}{T_\phi} = f_m\ N_b = [1/s] \qquad (2.29)$$

Lateral *spatial* frequency and lateral *temporal* frequency are related by:

$$f_\phi = k_\phi\ f_m \qquad (2.30)$$

One-dimensional representation of the three-dimensional scattering distribution:

Equation 2.3 states that the received linear signal (in three dimensions) is given by a spatial convolution between the point spread function and the three-dimensional scattering distribution. This is valid in the far field and close to the axis where the radial and lateral terms of the point spread function are separable:

$$g(r,\phi,\psi) = h(r,\phi,\psi) \ \ \text{conv} \ \ \sigma(r,\phi,\psi) \qquad (2.31)$$

The Fourier transform of this equation is written:

$$G(k_r,k_\phi,k_\psi) = H(k_r,k_\phi,k_\psi)\ \Sigma(k_r,k_\phi,k_\psi) \qquad (2.32)$$

The autocorrelation function of the received signal is given by:

$$\mathbf{R}_{3D}(r,\phi,\psi) = E\{ g(r_o + r, \phi_o + \phi, \psi_o + \psi)\ g(r_o, \phi_o, \psi_o) \} \tag{2.33}$$

If the scattering distribution is a stationary random process, the Wiener-Khintchine theorem [Roberts 1987] can be applied to Equation 2.32 yielding:

$$\mathbf{P}_{g3D}(k_r,k_\phi,k_\psi) = | H(k_r,k_\phi,k_\psi) |^2 \ \mathbf{P}_\Sigma(k_r,k_\phi,k_\psi) \tag{2.34}$$

where "$\mathbf{P}_{g3D}(k_r,k_\phi,k_\psi)$" is the power spectral density of $g(r,\phi,\psi)$ in three dimensions.

The scattering distribution is assumed to be a random white (stationary) process. The spatial autocorrelation function is given by:

$$\mathbf{R}_\sigma(r,\phi,\psi) = \delta(r)\ \delta(\phi)\ \delta(\psi) \tag{2.35}$$

which means that the power spectral density $\mathbf{P}_\Sigma(k_r,k_\phi,k_\psi)$ is constant and it is denoted $\mathbf{P}_\Sigma$.

The three-dimensional representation of the signal can be reduced to a two-dimensional (radial and lateral) representation by setting the azimuthal angle equal to zero in the autocorrelation function, i.e. integrating over the azimuthal frequency range:

$$\mathbf{R}_{2D}(r,\phi) = \mathbf{R}_{3D}(r, \phi, \psi{=}0) \tag{2.36}$$

The power spectrum in the lateral direction is then (for a constant range to the scatterers):

$$\mathbf{P}_{g2D}(r,k_\phi) = \frac{1}{2\pi} \int dk_\psi\, \mathbf{P}_{g3D}(k_r,k_\phi,k_\psi) \tag{2.37}$$

Inserting Equations 2.34 and the power spectral densities for the point spread function and the scattering distribution yields:

$$\mathbf{P}_{g2D}(r,k_\phi) = \frac{1}{2\pi} \int dk_\psi\ | R_{FT}(k_r) |^2 \ | A_{FT}(k_\phi,k_\psi) |^2 \ \mathbf{P}_\Sigma \tag{2.38}$$

For a constant range "r", this yields the following expression for the one-dimensional power spectrum in the lateral direction which is denoted:

$$\mathbf{P}_{g\phi}(\mathbf{k}_\phi) \sim \int \mathbf{dk}_\psi\ | \mathbf{A}_{FT}(\mathbf{k}_\phi,\mathbf{k}_\psi) |^2 \tag{2.39}$$

The power spectral density of the lateral signal from many scatterers (representing a stationary random process whose spatial autocorrelation function is a δ-function) located in the far field (and near the axis) can be found by integrating $| A_{FT}(k_\phi,k_\psi) |^2$ over the azimuthal frequency range.

Analytical solution to $\mathbf{A_{FT}(k_\phi,k_\psi)}$:

Angelsen presents an analytical solution to the two-dimensional Fourier transform of $A(\phi,\psi)$ (the far field two way angular sensitivity function for a flat circular transducer excited uniformly with CW) [Angelsen 1991].

The two-way sensitivity function "$A(\phi,\phi',\psi,\psi')$" is the square of the one-way function "$H_e(\phi,\phi',\psi,\psi')$". Since multiplication in the temporal/spatial domain equals convolution in the frequency domain, the result can be found by spatial convolving of "$H_{eFT}(k_\phi,k_\psi)$" with itself:

$$\mathbf{A}_{FT}(k_\phi,k_\psi) = \frac{1}{4\pi^2} \int dp\, dq\, \mathbf{H}_{eFT}(k_\phi-p,k_\psi-q)\, \mathbf{H}_{eFT}(p,q) \tag{2.40}$$

$\mathbf{A}_{FT}()$ denotes the Fourier transform of $A()$ and $\mathbf{H}_{eFT}()$ denotes the Fourier transform of $H_e()$. For the circular transducer with uniform excitation, "$\mathbf{H}_{eFT}(k_\phi,k_\psi)$" is given by a pie-shaped function, a slice of a cylinder. The convolution is performed by keeping one "pie" fixed and moving the other around while the overlapping volume is integrated, see Figure 2.7(a). The radius of the cylindrical slices is "$k_o\, a$".

The resultant function, the two-dimensional Fourier transform will peak in zero and fall down to zero for a circle of radius $2k_o\, a$, see Figure 2.7(b). The analytical solution to the convolution is given by:

$$\mathbf{A}_{FT}(k_\phi,k_\psi) = \begin{cases} \dfrac{4\pi^2\rho^2}{k_o^4} \left\{2k_o^2a^2 \cos^{-1}\left(\dfrac{k}{2k_oa}\right) - kk_oa\sqrt{1 - \left(\dfrac{k}{2\,k_o\,a}\right)^2}\,\right\} & k < 2k_o a \\ 0 & \text{elsewhere} \end{cases} \tag{2.41}$$

$$k = \sqrt{k_\phi^2 + k_\psi^2}$$

The angular two-way sensitivity function represents a low-pass filter operation to the signal in the lateral and the azimuthal direction.

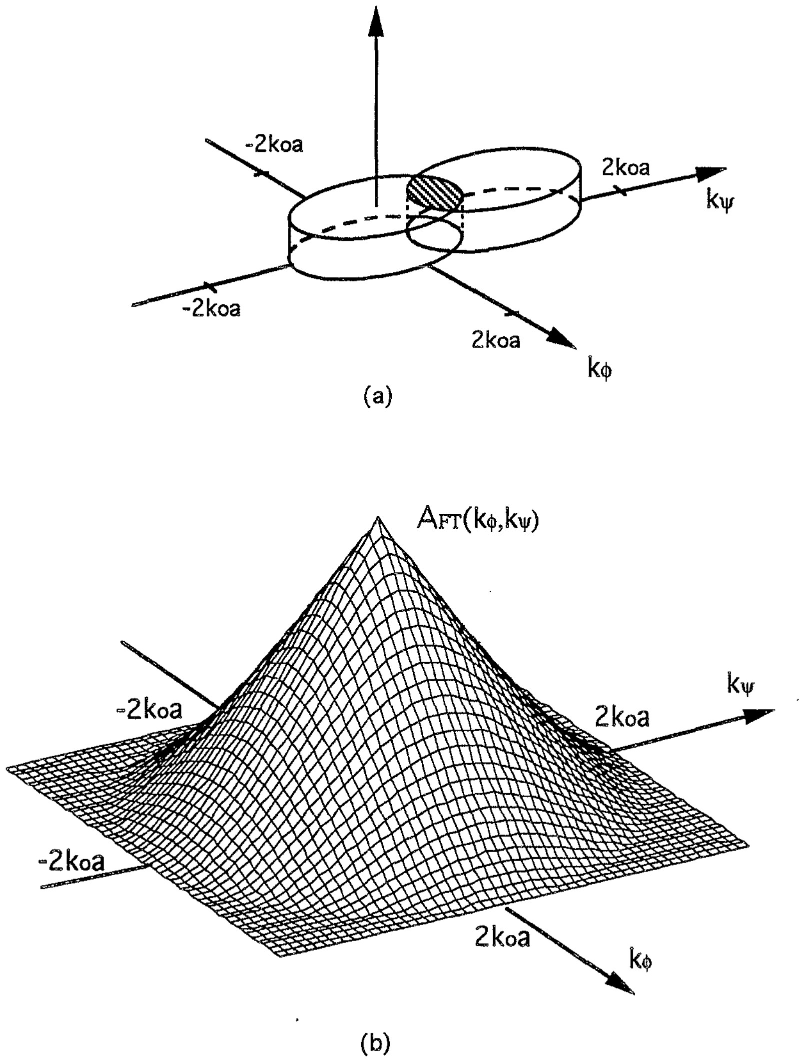

Figure 2.7 *(a) The spatial Fourier transform of $A(\phi,\psi)$ is given by the convolution of the Fourier transform $H_{eFT}(k\phi,k\psi)$ with itself. The latter function is a cylinder slice for a circular transducer excited uniformly with CW.*

(b) The two dimensional Fourier transform $A_{FT}(k\phi,k\psi)$ is given by the volume of the overlapping regions in (a).

Numerical solution to the power spectrum in the *lateral* direction:

The power spectral density in the lateral direction "$\mathbf{P}_{g\phi}(k_\phi)$" is found by numerical integration of Equation 2.39 using Equation 2.41:

$$\mathbf{P}_{g\phi}(k_\phi) \sim \int_{\text{numeric}} dk_\psi \, | A_{FT}(k_\phi, k_\psi) |^2 \tag{2.42}$$

The maximum lateral spatial frequency component is:

$$k_{\phi Max} = 2k_o a = \frac{4\pi a}{c} f_o = 2\pi \frac{D_{XD}}{\lambda_o} \tag{2.43}$$

This power spectrum in the lateral direction is plotted in Figure 2.8, a linear plot in (a) and a semilogarithmic plot in (b).

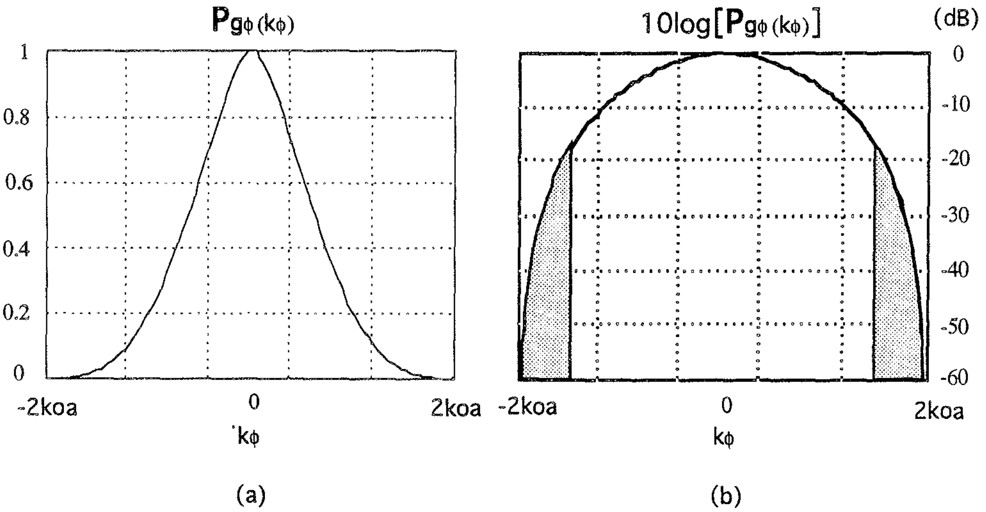

Figure 2.8 *Power spectrum in the lateral direction from a large amount of randomly distributed stationary scatterers. The result is found by numeric integration and will be used as a model for the power spectrum from stationary vessel wall and blood.*
(a) Linear plot. (b) Logarithmic plot.
The shaded area covers the upper 25% of the band where only 2.4% of the power is present.

This power spectrum is an important result. Strictly speaking it is only valid in the far field and for uniform CW-excitation of a circular transducer. But it is also valid in the focal region of a circular focused transducer excited uniformly with CW. However, the experiments have shown that its applications can be extended to the PW-mode:

Equation 2.42 (and 2.43) which is illustrated in Figure 2.8 is used to describe the spectrum (and its maximum frequency component) from stationary vessel wall and stationary blood scatterers in the *far field* and in the *near field* for *PW-excitation*.

An interesting observation can be made by integrating Equation 2.42 over a certain frequency band to see how much power is present in that particular band. This area of integration is illustrated in Figure 2.8(b) by a shaded area covering the upper 12.5% of the band on either side.

In the upper 25 % of the band only 2.4 % of the total power is present.

Measurements:
Some measurements are performed in Section 3.2.2 to compare the measured spectrum with the theoretical. A large number of small stationary scatterers were imaged and a power spectral estimate in the lateral direction was calculated. A typical measured spectrum is shown in Figure 3.6 together with the theoretical spectrum from Equation 2.42.

The measured power spectrum from a large amount of scatterers compares acceptable with the theoretical result presented in Equation 2.42.

2.3.2 Power spectrum from pulsating vessel wall

The power spectrum in the lateral direction from a vessel wall that is pulsating may be slightly different than the spectrum from a stationary vessel wall. Three factors may affect the spectrum:

1) The spectrum is *shifted* due to radial dilation, a Doppler shift is introduced.
2) The spectrum is *broadened* due to reduced transit time caused by relative *radial* movements between the catheter and the vessel wall.
3) The spectrum is *broadened* due to reduced transit time caused by relative *lateral* movements between the catheter and the vessel wall.

Doppler shift due to vessel wall velocity: An approximate description of the maximum radial vessel wall velocity is given by:

$$V_{VW} \approx \frac{\Delta r_{max}}{\Delta t_{min}} \tag{2.44}$$

where Δr_{max} is the maximum radial dilation and Δt_{min} is the minimum time the vessel needs to expand. Nichols tabulates some measured values of the radial pulsation ($\Delta r/r$) in percent for some peripheral and coronary arteries in humans and dogs [Nichols 1990]. Values exceeding 5% rarely occur. Applied to a peripheral artery of radius r=2.5mm, the radial dilation is: Δr_{max} = 0.125mm. Further assume the vessel expands during the rising edge of the systole. An approximate value for the minimum expansion time is set to: $\Delta t_{min} \approx$ 100msec. This yields the following estimate of the vessel wall velocity: $V_{VW} \approx$ 1.25 mm/sec. Although this is not an accurate method, it gives an estimate of what order of magnitude can be expected.

The vessel diameter has been measured with an A-mode ultrasound instrument by tracking the vessel walls with a phase locked loops system [Hokanson, 1972]. The maximum vessel wall velocity extracted from a femoral artery plot was: $V_{VW} \approx$ 2.7 mm/sec.

The vessel wall velocity in peripheral and coronary arteries does usually not exceed V_{VWmax} = 5 mm/sec.

The radial vessel wall velocity is highest during expansion. The spectrum in the lateral direction from vessel wall movements will be shifted more in the negative direction than in the positive direction. But as will be shown in Section 2.3.3:

The Doppler shift from a pulsating vessel wall is small compared to the Doppler shift from blood.

Frequency broadening due to relative *radial* velocities: The spectrum in the lateral direction will be changed when radial velocity components are introduced. The spectrum can no longer be determined by the angular sensitivity function of the beam only. The radial properties will come into account.

The transit time for a scatterer through the sample volume is determined by the lateral and radial sizes of the sample volume, and also by the radial and lateral relative velocity components between the scatterer and the sample volume. Radial velocity components will cause the vessel wall scatterers to traverse through the sample volume "diagonally" in contrast to purely laterally.

The lateral velocity of the sample volume is given by:

$$V_{\phi SV} = 2\pi f_m r \tag{2.45}$$

and typical values range from ≈6 to ≈180 cm/sec. The maximum radial vessel wall velocity is set to ≈0.5 cm/sec. By observing video tapes of human and pig studies, radial velocity components due to catheter tip translation are estimated to be of the same order as the maximum vessel wall velocity. This means that the worst case radial velocity through the sample volume is $V_{rSV} \approx 1$cm/sec.

The radial velocity component is small compared to the lateral velocity component. Although the radial size of the sample volume is smaller than the lateral size, the transit time is primarily determined by the lateral velocity component.

Radial vessel wall and catheter tip movements do not alter the spectrum in the lateral direction significantly.

Frequency broadening due to relative *lateral* velocities: In some beam directions, a lateral velocity component may occur between the vessel wall scatterers and the sample volume. When the lateral velocity component *adds* to the velocity of the sample volume, a reduced transit time results which broadens the spectrum and vice versa.

Lateral velocity components due to catheter movements are estimated to be approximately equal to the radial components, i.e. ≈0.5 cm/sec. This means that the relative velocity between vessel wall scatterers and the sample volume may be changed by ± 0.5 cm/sec. Compared to the typical values listed previously: 6-180 cm/sec., this represents a small change.

Lateral velocity components due to catheter tip movements do not alter the spectrum in the lateral direction significantly.

2.3.3 Power spectrum from blood

The power spectrum in the lateral direction from *stationary blood* is assumed to be identical to the spectrum from stationary vessel wall given by the spatial frequency content in Equation 2.42. When a blood velocity is introduced and the beam is tilted, three effects change the spectrum:

1) The spectrum is *shifted* in frequency according to the Doppler equation.
2) The spectrum is *broadened* due to reduced transit time through the sample volume.
3) The spectrum is *broadened* and changed due to blood velocity distribution over the sample volume.

Only the first two effects will be described. The main effect caused by a velocity distribution is a broader spectrum. The measured spectrum is the sum of the spectra from all individual scatterers. Scatterers with different velocities will contribute with different mean frequencies (Doppler shifts) and with different bandwidths (given by the transit time). The *shape* and the *bandwidth* of the spectrum changes.

It is assumed that the frequency shift and the frequency broadening effect can be described separately due to the following approximations:

a) *Far field* (or focal region) operation *close to the axis* : The radial and the lateral terms in the point spread function are separable.
b) The beam *tilt angle is small* and the *beam is narrow*. The frequency broadening effect is dominated by the reduced transit time. The broadening effect due to radial velocity components from blood is negligible.

Frequency shift from blood: The Doppler shift is proportional to the system frequency and the velocity component "V_r" along the beam. The Doppler equation is plotted for some realistic values in Figure 2.9. The blood velocity range is set from ≈100 cm/sec. forward flow to ≈30 cm/sec. reversed flow. The figure illustrates how the polarity of the Doppler shift can be selected by tilting the beam.

Frequency broadening due to reduced transit time: The relative velocity between the sample volume and *stationary* blood scatterers is purely lateral. The temporal power spectrum in the lateral direction (beam to beam) is given by the beam width and beam angular velocity. The result is given by Equation 2.42 for a particular circular symmetric beam. If the beam rotation is stopped, and a blood velocity is introduced, the temporal spectrum from the sampled signal (beam to beam) will be determined by the beam width in the azimuthal direction and by the blood velocity.

If the beam is circular symmetric, as will be assumed here, the *shape* of the spectrum will be independent of the traverse direction through the beam. When the beam is scanning and the blood velocity is different from zero, the scatterers will traverse through the beam with a lateral and an azimuthal component, here denoted an *angular* blood velocity component "V_{Ba}". The net relative velocity is given by the following expression assuming the approximations a) and b) hold:

$$V_{Ba} \approx \sqrt{(V_{\phi SV})^2 + (V_B)^2} \geq V_{\phi SV} \qquad (2.46)$$

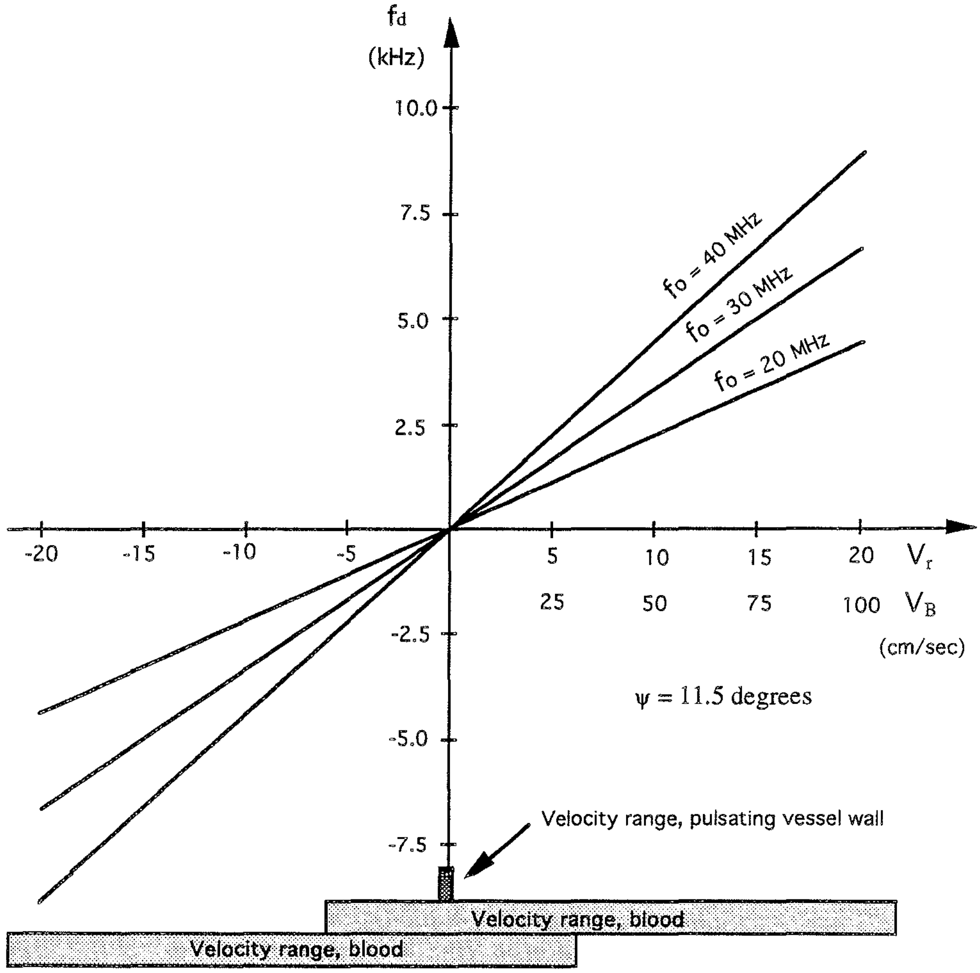

Figure 2.9 *Illustration of the Doppler shift versus the velocity component "V_r" in the radial beam direction and versus the blood velocity "V_B" in case of a beam tilt angle ψ = 11.5 degrees.*
Note that the radial velocity component from a pulsating vessel wall is small compared to blood velocities.

The Doppler equation: $f_d = -2 \frac{f_o}{c} V_r$

Blood: $f_{d,Blood} = -2 \frac{f_o}{c} V_B \sin(\psi)$

The ratio of the transit time for stationary blood and for flowing blood is given by (using Equation 2.46):

$$\frac{T_{BloodStas}}{T_{BloodFlow}} = \frac{V_{Ba}}{V_{\phi SV}} = \sqrt{1 + \left(\frac{V_B}{V_{\phi SV}}\right)^2} \tag{2.47}$$

The Fourier transform properties state that *scaling in the temporal domain* corresponds to *scaling in frequency and amplitude* in the frequency domain. Compressing a temporal signal broadens and lowers the spectrum (power conserving). This transit time ratio in Equation 2.47 represents a temporal scaling of the result obtained in Equation 2.42.

By inserting Equation 2.45 into Equation 2.47, the *blood spectrum broadening factor* due to reduced transit time is defined:

$$\mathbf{k_{BSB}} = \sqrt{1 + \left(\frac{\mathbf{V_B}}{2\pi\, \mathbf{f_m r_o}}\right)^2} \geq \mathbf{1} \tag{2.48}$$

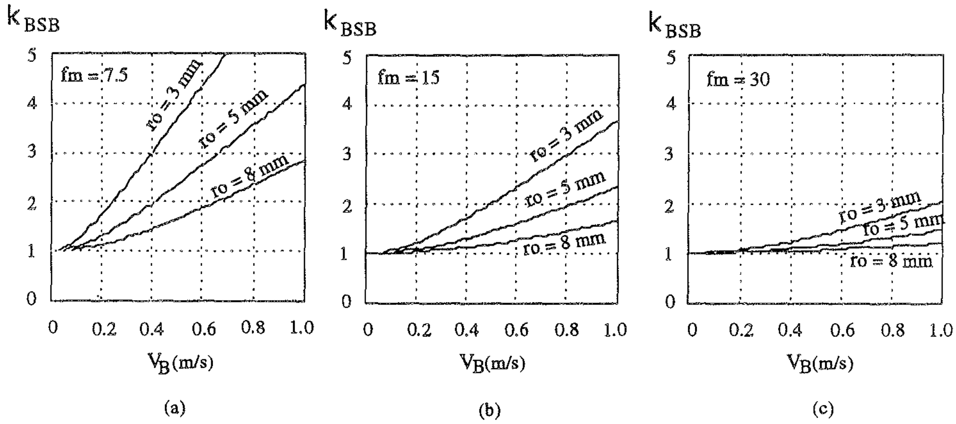

Figure 2.10 *The* ***blood spectrum broadening factor*** *"* $\boldsymbol{k_{BSB}}$ *" versus blood velocity for some realistic parameters.*
(a) $f_m = 7.5$ *f.p.s., (b)* $f_m = 15$ *f.p.s., (c)* $f_m = 30$ *f.p.s.*
Low frame rates and scatterers located close to the axis make the blood velocity dominate over the sample volume velocity, the spectrum is broadened due to reduced transit time (a).
High frame rates cause the lateral velocity of the sample volume to dominate over the blood velocity, a minor frequency broadening takes place (c).

This broadening factor is plotted versus blood velocity for some realistic values in Figure 2.10. For low frame rates and scatterers located close to the axis, the blood velocity dominates over the sample volume velocity, and the spectrum is broadened due to reduced transit time. This is illustrated in (a). For high frame rates, the lateral velocity of the sample volume will dominate over the blood velocity, and a minor frequency broadening takes place due to the blood velocity.

This result is based on the assumption that the beam width is proportional to the range "r_0". This is an acceptable approximation within the focal region of a focused beam. Closer to the transducer, the beam width is broader and the transit time will be longer than described. Values less than r_0 = 3 mm are therefore not listed in the figure.

> **The spectrum from flowing blood will be broadened by the *blood spectrum broadening factor* "k_{BSB}" relative to the spectrum from stationary blood. Realistic values are k_{BSB} = 1-4.**

Frequency shift *and* frequency broadening: The combined effect of frequency shift given by the Doppler equation and the frequency broadening effect due to reduced transit time is illustrated schematically in Figure 2.11. The power spectrum from stationary scatterers (illustrated in Figure 2.8(a)) is first shifted to the frequency given by the Doppler shift and the blood velocity. Then the spectrum is scaled in frequency due to Equation 2.48. Finally, the amplitude is scaled down to keep the mean power constant. A realistic phasic blood velocity curve is applied and the spectrum is plotted versus the phase of the cardiac cycle.

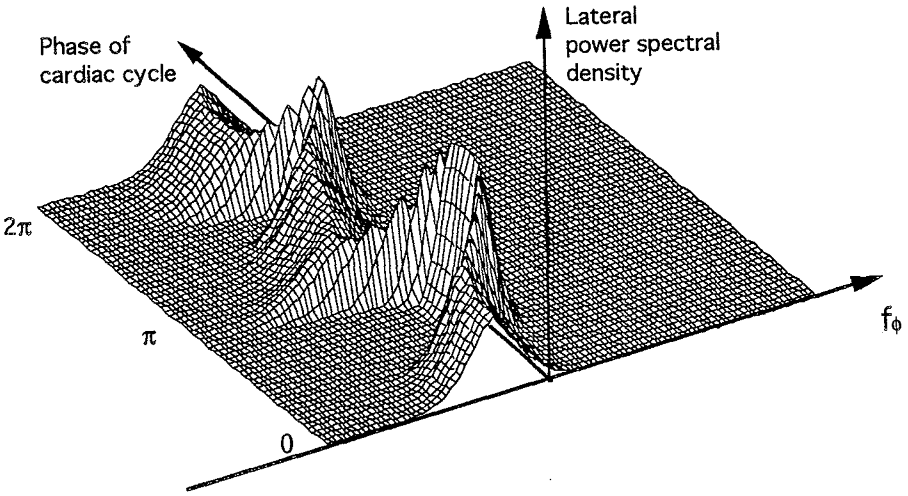

Figure 2.11 *Schematic illustration of the spectrum from blood in the lateral direction versus phase of the cardiac cycle. The plot is generated by shifting the spectrum in Figure 2.8(a) to the frequency given by the Doppler and a realistic phasic blood velocity. Then the spectrum is scaled in frequency and amplitude by the blood spectrum broadening factor "k_{BSB}" in Equation 2.48.*

2.4 Logarithmic amplifier

The main purpose of the log-amp is to increase the local dynamic range. The analog log-amp compresses an input range of approximately 60 dB into a 0-5 Volts output range (black-white) at 10 MHz system frequency. (The input range it can handle drops gradually to ≈50 dB at 30 MHz.) When the instrument was designed, only 8 bits 20 MHz AD-converters were available. 10 and 12 bits AD-converters that are presently available can handle this dynamic range directly. If such components are used, the analog log-amp will be obsolete. A compression will be required to adapt the linear acoustic signal to the logarithmic characteristics of the eye, however, this function can be done digitally.

Due to its non-linearity, the log-amp is complex to analyze. Superposition does not hold which makes it difficult to find the response from a large amount of scatterers. In this section, the signal received from a single point scatterer will be simulated for some simple examples. Radial and lateral properties will be illustrated.

2.4.1 Model for the log-amp

The specific log-amp used in this work is based on a chip from Texas, the TL-441C. This circuit as it is realized in the system can be described as the sum of four tangent hyperbolic terms. The input signal is fed to four identical "tanh" functions through different preceding gain stages. Each section handles 1/4 of the total input range of the log-amp. The most sensitive channel takes care of the weakest signals. As the input signal strength increases, the first stage saturates and the next stage is activated. This takes place until all four stages are saturated. If bandwidth limiting effects are neglected, the mathematical function of the log-amp can be written:

$$\mathbf{F}_{LogAmp}\{U_{In}\} = U_{Out} = K\,[\,\tanh(G_1\,U_{In}) + \tanh(G_2\,U_{In}) + \tanh(G_3\,U_{In}) + \tanh(G_4\,U_{In})\,] \qquad (2.49)$$

"K" is an absolute gain factor and $G_1..G_4$ is the individual gain of each channel. This function is plotted in Figure 2.12 in a semi-logarithmic plot. The parameters are adjusted for a best fit (at 10 MHz system frequency) to the measured response of the log-amp used in this work.

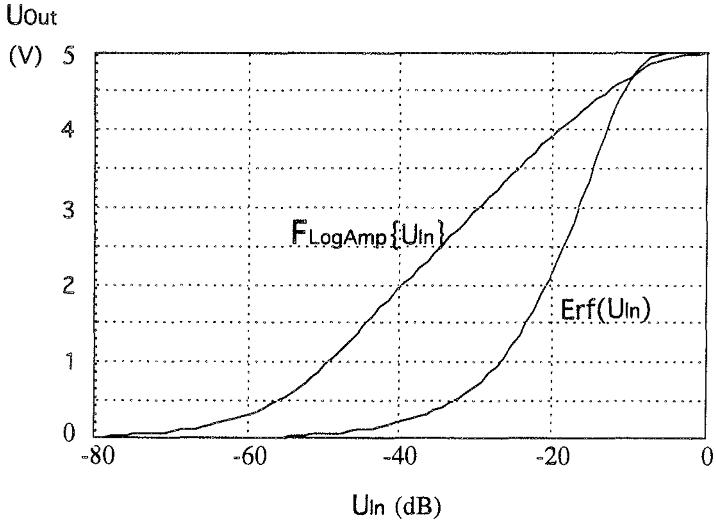

Figure 2.12 *Semi-logarithmic plot of the infinite bandwidth "tanh"-compression function $\mathbf{F}_{LogAmp}\{U_{In}\}$. This function is used as a model for the real log-amp at 10 MHz system frequency. (Input dyn. range ≈ 60 dB).*
An alternative compression function, the "error-function" $Erf(U_{In})$ is shown for comparison.

Real logarithmic amplifiers have limited bandwidth and will only perform as the model describes in a limited frequency range. A low pass filter operation should be added to take care of the limited bandwidth in the transistors. As shown in Figure 2.1, a band-pass filter is implemented after the log-amp. The purpose of this filter is to reject higher order spectrums generated by the log-amp. The effect of this filter comes in addition to the dynamic characteristics of the log-amp chip itself.

2.4.2 Other compression functions

Other compression functions than the "tanh" exist, some examples are: $\tan^{-1}$, $\tanh^{-1}$, μ-law, A-law and Erf. The Erf-function is defined as the integral from zero to U_{In} of the normalized Gaussian function:

$$\mathrm{Erf}(U_{In}) = \frac{1}{K} \frac{1}{\sqrt{2\pi}\,\sigma_1} \int_0^{U_{In}} dz\, e^{-z^2/2\sigma_1^2} \qquad (2.50)$$

The Erf-function is also plotted in Figure 2.12.

The Erf-function: The Erf-function is of special interest in that there is a closed form expression to the normalized autocorrelation function at the output for a Gaussian input (given a normalized input autocorrelation function) [Baum 1957]. This makes it possible to find analytical expressions to the output power spectrum from Erf-compressed Gaussian noise passed through a filter.

If the input to an Erf-function is *low-pass* filtered Gaussian noise of bandwidth "BW", the output spectrum will contain an infinite sum of low-pass spectra, the first and strongest will have bandwidth BW, the second is weaker (depending on the degree of compression) will have bandwidth 3BW, the next 5BW and so forth.

If *band-pass* filtered Gaussian noise with bandwidth BW centered at "f_0" is passed through the Erf-function, the following modified situation will occur: The same fundamental spectrum "family" of width BW, 3BW, 5BW, etc. appears, but centered around "f_0". In addition an infinite sum of spectrum families appears, centered around $3f_0$, $5f_0$, $7f_0$,... etc. These odd harmonic spectral-families are not true copies of the fundamental one, they get broader the higher the center frequency. The spectra located around $3f_0$ are three times as broad as the fundamental family, the spectra located around $5f_0$ are 5 times broader etc.

Although the Erf-function shown in Figure 2.12 deviates from the "tanh" function used in this work, it is reasonable to assume that the frequency content in the radial direction from the two will be related.

2.4.3 Effect on a single point scatterer in the radial direction

A simple single scatterer simulation is performed to gain some physical insight in how the log-amp affects the signal in the radial direction.

Assume a single scatterer is located in the ultrasound beam. The transmit signal "U_{TX}" is converted to an acoustic pulse by the transducer which is described by the Mason equivalent [Angelsen 1991]. This means that the transfer function from the electric to the acoustic port can be modeled by a second order band-pass filter. Realistic parameters are found by measuring the impedance of a typical transducer. The electrical signal received from the point scatterer is found by filtering the electrical transmit pulse back and forth through the second order filter. The resulting linear signal is denoted "U_{RadLin}". Passing this signal through the "tanh"-compression function yields the compressed signal "U_{RadLog}".

Temporal domain: Measured parameters for a realistic 20 MHz transducer are inserted in the Mason's model. A transmit signal consisting of 3 unipolar rectangular pulses at f_0=20MHz is filtered twice through the band-pass filter. The transmit signal "U_{TX}" is shown in Figure 2.13(a). The linear filtered signal "U_{RadLin}" is rectified and shown in Figure 2.13(b). Limited transducer bandwidth causes ringing. The received pulse is broader than the applied pulse.

Passing this signal through the model for the log-amp yields "U_{RadLog}" which is rectified and shown in (c). The pulse is now even broader since the weak signals are amplified and made visible. This causes the radial resolution to drop. The envelope of the pulse rises rapidly in a steep leading edge, but the tail drops slowly to zero. Compression causes the original sinusoidal carry wave to be more rectangular. High frequency components are obviously introduced by the log-amp.

Frequency domain: A power spectral estimate of "U_{RadLin}" and "U_{RadLog}" is shown in Figure 2.13(e). The power spectral estimate operation is denoted: PSE{.}

In the linear case, spectra at odd harmonics of the transducer center frequency appear as expected due to rectangular transmit signal with 50% duty cycle (bold curve). The two-way band-pass filter operation reduces the power spectral density at high frequencies.

In the compressed case, the power spectral density is substantially higher in these odd harmonic components. This can be explained by the compression of the carry wave, the tendency of squaring the pulses.

The increased pulse width in the temporal domain caused by the log-amp is described by a narrower main lobe of the spectrum.

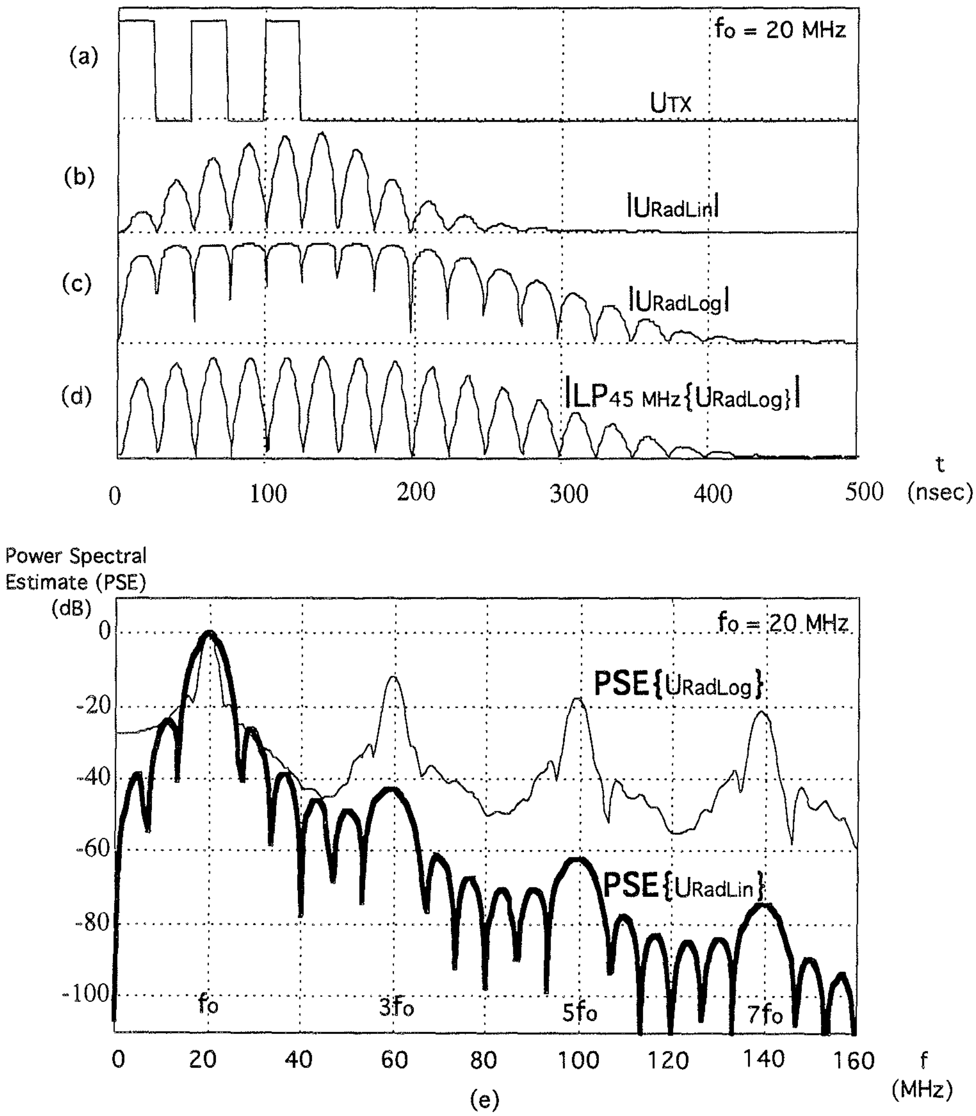

Figure 2.13 *Transmit signal and three rectified received waveforms in the radial direction for a point scatterer. The transducer is modeled as a second order band pass filter in both directions. (Mason's equivalent).*
(a) Transmit signal.
(b) Linear received signal.
(c) The linear signal compressed in the infinite bandwidth " tanh" compression function.
*(d) Compressed and **low pass filtered** signal.*
(e) Power spectral estimate of the linear signal in (b) and the compressed signal in (c).

Finite bandwidth compression function: By applying a low-pass filter operation to the signal after log-compression, a more realistic situation is obtained. A 10th order Chebyshev filter with 45 MHz cutoff frequency was realized in the simulation. This filter is symbolized by the following operator:

$$\mathbf{LP}_{45\,\mathrm{MHz}}\{\,\cdot\,\}$$

This filter effectively rejects all the odd harmonic spectra. The resulting temporal pulse is shown in Figure 2.13(d). The envelope has changed negligibly by the bandwidth limitation. This indicates that most of the envelope information is maintained in the fundamental spectrum family.

The carry wave is restored to an approximately sinusoidal signal as desired. This is important when considering the Doppler shift from blood. If the input to the Quadrature Demodulator contains higher order spectra, the radial phase term and thereby the Doppler shift will be distorted.

For the purpose of sampling the RF-signal and use the phase information, the bandwidth of the compressed signal should be limited to only include the fundamental spectrum generated by the log-amp.

If the low-pass filter effect in the log-amp chip itself is not necessary to cut the higher order spectra, a low-pass filter should be included after this device.

The pulse length is increased in the radial direction due to the log-amp. In the frequency domain this corresponds to a narrower main lobe of the spectrum.
Both the envelope and the carry wave are compressed. This is described in the frequency domain by broadened spectra at the fundamental transmit frequency and at the odd harmonics of the same.

2.4.4 Effect on a single point scatterer in the lateral direction

As in the previous section, a simple single scatterer simulation is performed in the lateral direction. A point scatterer traverses the beam at constant range, crossing the beam axis in a pure lateral movement. The acoustic field is supposed to be generated by a flat circular transducer of diameter a=0.68mm excited uniformly by CW at 20 MHz. If the scatterer is located in the far field, the received signal strength is given by Equation 2.23, the two-way angular sensitivity function $A(0,\phi',0,\psi')$. The linear signal strength is given by:

$$U_{LatLin}(\phi', \psi'=0) = \left[\frac{2\,J_1(k_o\,a\,\sin(\phi'))}{k_o\,a\,\sin(\phi')}\right]^2 \qquad (2.51)$$

Passing this linear signal through the infinite bandwidth "tanh"-compression function yields:

$$U_{LatLog}(\phi', \psi'=0) = F_{LogAmp}\{\,U_{LatLin}(\phi', \psi'=0)\} \qquad (2.52)$$

Spatial domain: These signals are plotted in Figure 2.14(a). The main lobe *width* of the beam increases, the *side lobe levels* of the beam increase and the *edges get steeper* when the log-amp is included. Increased beam width degrades the lateral resolution.

Frequency domain: A power spectral estimate of "U_{LatLin}" and "U_{LatLog}" is shown in Figure 2.14(b). Again the power spectral estimator is denoted: **PSE**{ . } The main lobe of the lateral spatial power spectral estimate is narrower in the compressed case. This corresponds to the increased lateral beam width. Steeper edges in the lateral compressed signal explain the increased bandwidth of the log-compressed spectrum. The spectrum becomes triangular.

Speckle and resolution: Introducing the log-amp causes the pulse width from a single scatterer to increase in both the radial and the lateral directions. It is reasonable to assume that the radial and the lateral *resolution will be degraded* by this device also when a large amount of scatterers is considered. However, the *speckle pattern is reduced* since the pulses are widened. The black speckle regions in the image get narrower, giving the image a more pleasant look. Ultrasound users seems to prefer less speckle at the expense of degraded resolution. In order to obtain this effect in the radial direction, the log-amp should be able to pass the entire *fundamental* spectrum through (see Figure 2.13(e). (in this example frequencies below 45MHz).

The log-amp causes the beam width to increase, and the edges of the main lobe and the side lobes get steeper.
In the frequency domain this corresponds to a narrower main lobe of the spectrum, but generally a broader (and triangular) spectrum.

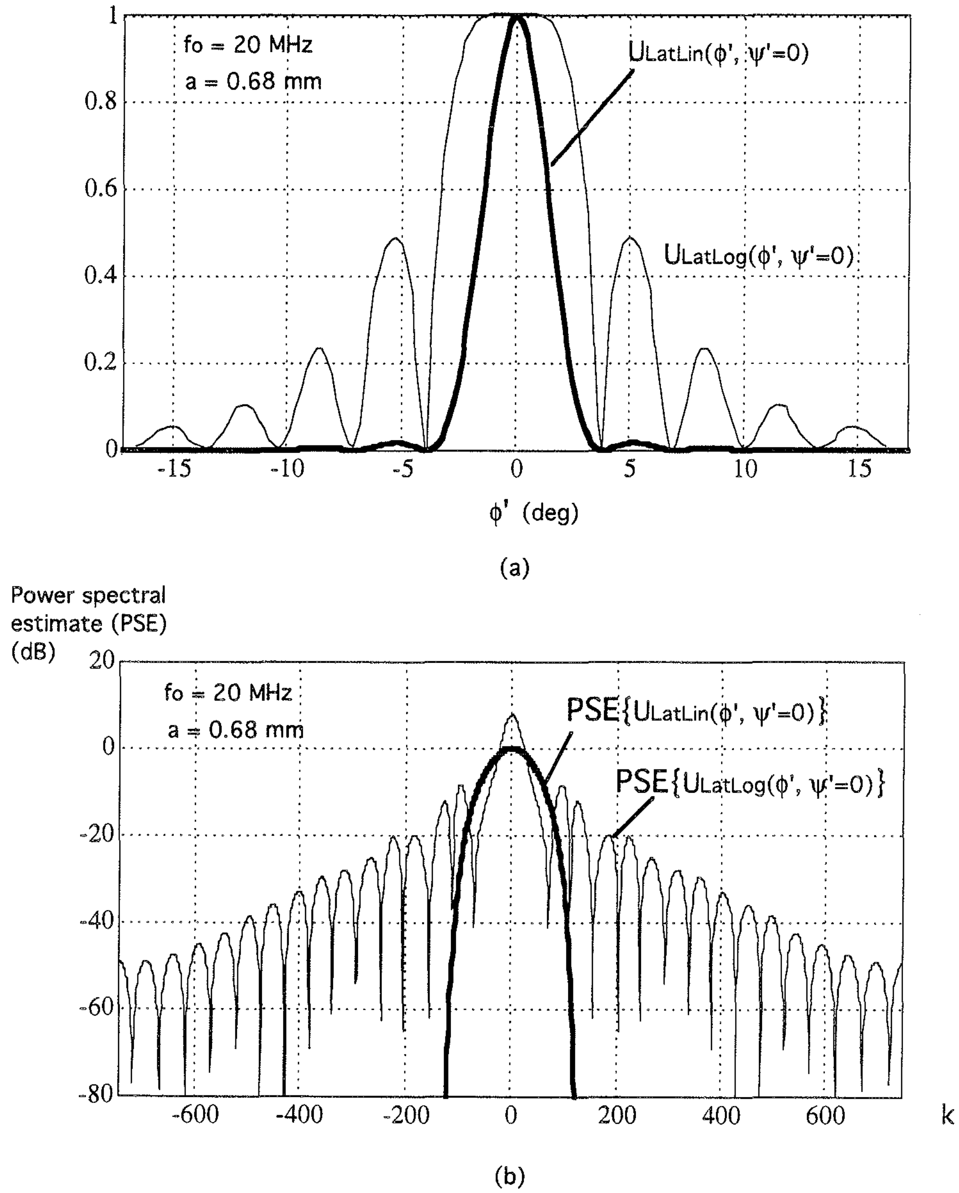

Figure 2.14 *Received signal strength from a single point scatterer traversing laterally through the beam axis in the far field. The transducer is flat and circular, and it is excited uniformly with CW.*

(a) Linear signal ULatLin() and compressed signal ULatLog().
(b) Power spectral estimate of ULatLin() and ULatLog().

2.4.5 Effect on electronic noise

The performance of the log-amp on electronic noise in combination with other signals is interesting. As an example, a uniform distributed white noise source "U_n" is added to a sinusoidal signal "U_{sin}" (variable amplitude). This signal is passed through the log-amp and the output is observed as the sinusoidal amplitude is increased.

A *compression function* is characterized by *signal level dependent gain*. Weak signals are amplified more than strong signals. This means that a weak noise source acting alone on the log-amp will be amplified strongly. This is illustrated in Figure 2.15(a) and (b).

When the same noise source is overlaid by a strong sinusoidal signal, the gain of the log-amp for the noise source will vary through the sinusoidal cycle. This effect is illustrated in Figure 2.15(c) and (d). Close to the zero crossings, the gain and the output noise power are both high. When the input mean value is high, the gain is low and very little noise power is observed at the output.

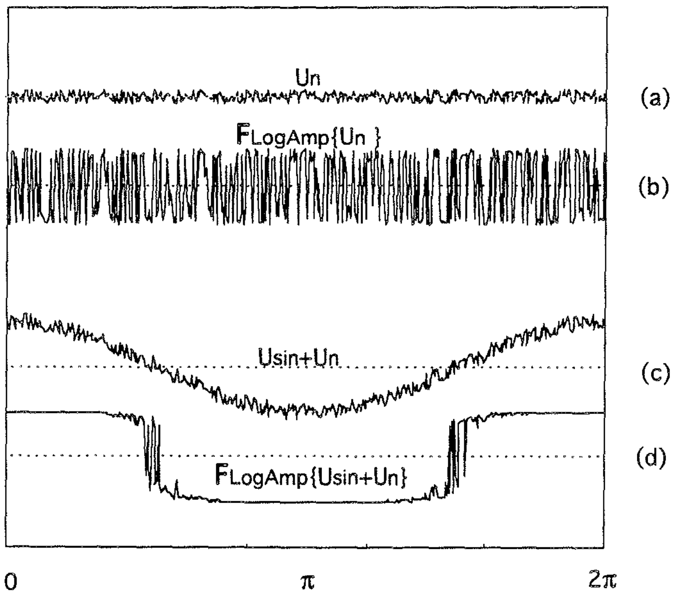

Figure 2.15 *The effect of compressing electronic noise alone and signal plus electronic noise in a "tanh"-compression function.*
(a) Input: Uniform distributed white noise "U_n",
(b) Output: Compressed white noise.
(c) Input: Noise "U_n" plus sinusoidal signal "U_{sin}".
(d) Output: compressed noise plus signal.
The average noise power is dramatically reduced when noise is overlaid a strong signal.

When only electronic noise is applied to the Quadrature Demodulator (linear frontend), the output "U_{QD}" (see Figure 2.1) will be a circular Gaussian process. If this signal is observed over a certain time interval, the vector will describe a "cloud" centered in origin of the complex plane. The diameter or size of the noise cloud is proportional to the input noise power.

If a sinusoidal signal with frequency "f_0" is added to the input of the linear frontend, the center of the noise cloud will be shifted out to a fixed position in the complex plane. The *distance from origin* is proportional to the amplitude of the sinusoidal signal, and the *angle* is given by the phase difference between the input signal and the local oscillator of the Quadrature Demodulator. The noise power is unchanged due to superposition in a linear system (assume no saturation).

If the same signal (electronic noise overlaid a sinusoidal component with frequency "f_0") is passed through the log-amp before it enters the Quadrature Demodulator, a different situation occurs. With noise only, a noise cloud centered in origin will appear. But as the amplitude of the sinusoidal signal is increased, the noise cloud will move out from the origin following a radial line, but the average noise power drops. The diameter or size of the noise cloud is reduced as the distance from origin increases.

This effect makes detection and canceling of *mirror leakage reverberations* simpler as will be shown in Section 4.4.

> **When electronic noise is added to a stronger signal, the average noise power at the output of the log-amp will decrease as the signal level increases.**

2.5 RF-signal model, summarized

From the preceding sections, the following conclusions can be drawn that summarize the main properties of the RF-signal model:

1) The acoustic near field of a transducer is complex to describe, the far field is simpler. Practical imaging is normally performed in the near field. The *far field approximation can be used in the imaging region* by proper focusing of the beam. This property is independent of transducer type (circular, elliptic, rectangular etc.)

2) In the far field and close to the axis, the point spread function is separable in the radial and angular directions. In this work it is assumed that the *point spread function is separable in the entire imaging region.*

3) A model for the power spectrum in the lateral direction is found for a large amount of randomly distributed scatterers. This spectrum is used to describe the spectrum from the stationary vessel wall, pulsating vessel wall and blood.
   The spectrum model is based on a flat circular transducer excited uniformly by CW. Measurements show that the spectrum is not sensitive to the transmitted pulse length. It is assumed that the *spectrum model based on a CW-excitation can be used for PW-excitation as well.* This model is transducer dependent.

4) The Doppler shift caused by vessel wall and catheter tip movements is negligible.

5) The spectrum in the lateral direction from flowing blood is a broadened version of the spectrum from stationary blood when the beam is circular symmetric. The bandwidth is broadened with the *blood spectrum broadening factor* "k_{BSB}" and the amplitude of the spectrum is scaled by $1/k_{BSB}$.
   The spectrum is shifted in frequency according to the Doppler equation when the beam is tilted.

Chapter 3

INSTRUMENTATION AND EXPERIMENTS

This chapter describes the important parts of the instrumentation, the test equipment and some of the experiments that have been done in this work. The purpose of the experiments is threefold:

1) to *extract signal characteristics* from realistic data.
2) to *verify* the signal model.
3) to *illustrate* signal properties.

Section 3.1 describes the equipment and the important design criteria required to be able to extract reliable information from the received signal. The bandwidth of the entire system should be limited by the transducer, and the total dynamic range of an intravascular imaging system should be approximately 80 dB. It is possible to design transducers with fractional bandwidth of 50-100% which means that the system is broad band and susceptible to sensor/amplifier noise and electromagnetic interference.

The instrument used in this work is designed for a 50% fractional bandwidth, and the transducers have a fractional bandwidth of approximately 25%. Electromagnetic interference (EMI) was noted to be the number one limiting factor for dynamic range. Several actions were required to reduce the EMI. A well designed pre-amplifier has a noise figure less than 3 dB. In this work a noise figure of 6 dB was obtained.

A synchronous detector (Quadrature Demodulator) was implemented to be able to digitize the RF-signal with the 8 bits 20 MHz AD-converters that were available at the time the instrument was designed. The dynamic range (single tone to intermodulation products) of this synchronous detector is 60 dB, which is sufficient for the 8 bits AD-converters.

Section 3.2 describes experiments for model verification. The RF-signal model presented in Chapter 2 is valid in the far field (or in the focal region of a focused transducer) with continuous wave (CW) excitation. It is found by experiments that the model can be applied in the near field and in the pulsed wave (PW) mode as well.

3.1 Instrumentation

3.1.1 Experimental setup

A functional block diagram of the instrumentation is shown in Figure 3.1.

The *motor* and the *transmitter (TX) & pre-amplifier (pre-amp)* are separated to reduce electromagnetic interference (EMI). The latter circuits are mounted in a shielded box which is connected directly to the RF-frontend with short leads (<10 cm).

A standard *catheter* is connected mechanically to the motor, but the electrical connection is tapped at the distal tip, and short leads (<20cm) are connected to the TX & pre-amp circuit to reduce the electromagnetic susceptibility.

Alternatively, a small *test tank* is connected to the motor. It consists of a rotating shaft with an acoustic mirror at the tip and a holder for a separate transducer. The transducer is aligned towards the mirror and connected to the TX/pre-amp circuit with short leads (<20cm).

The *analog RF-frontend* (see Figure 2.1 for a more detailed description) contains basically a Time Gain Compensation (TGC) circuit, a log-amp and a peak detector. It is realized for 10, 15, 20 and 30 MHz. The board has two outputs:

1) A compressed and peak detected (low-pass) signal for the purpose of real time display.

2) The RF band-pass signal which is compressed or not (selected by jumpers) for the purpose of storage, transfer to the computer, post processing and analysis.

The *data acquisition* board contains two 8 bits flash AD-converters and also the Quadrature Demodulator (QD) which mixes the band-pass signal down to the base band. The quadrature demodulator is realized for 20 MHz only.

The two AD-converters sample the *in phase* and the *quadrature component* simultaneously when the instrument is in "QD-mode". When the *peak detected* signal is sampled, the two AD-converters operate 180 degrees out of phase. The mode of operation: *peak detected* or *QD-mode* can be changed by software in a time frame less than one motor revolution. It is not possible to display the magnitude of the quadrature demodulated signal in real time.

Data acquisition is performed by running the system in normal real time peak detected mode. The data transferred on the bus is written to the display unit and to the memory board simultaneously. Data storage is prepared by localizing the region of interest on the screen. By pressing a button, the instrument transfers one normal peak detected frame to the memory board. Then it switches to QD-mode and transfers a pre-defined number of QD-frames. Finally one normal peak detected frame is transferred. The frame memory board then contains the RF-data with one peak detected image at each side. This data sequence is transferred to the computer over a parallel line by the CPU-board.

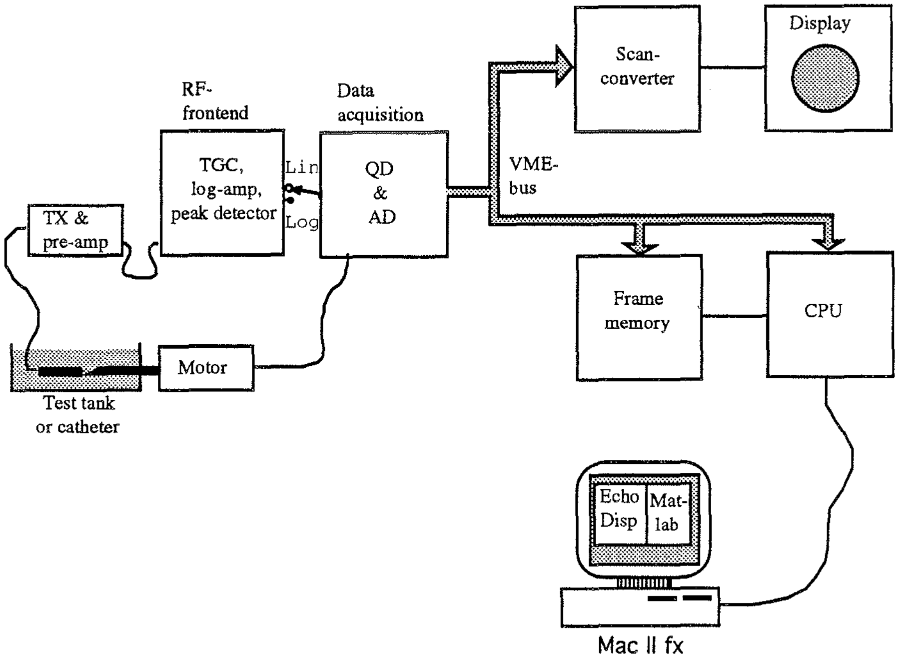

Figure 3.1 *Functional block-diagram of the instrumentation. Linear or compressed RF-signals are stored in the frame memory board and transferred to the computer for post processing and analysis. The pre-amplifier and transmitter circuit is separated from the motor drive unit to reduce EMI.*

A Macintosh IIfx was used for *post processing*. The program "EchoDisp" (Vingmed Sound, Horten, Norway) was used to simplify the access to the raw data and perform scan conversion and display. A control was obtained by comparing the two peak detected images so that unwanted movements would not occur during QD-sampling. With reference to the peak detected images, small regions (beams or circles) of raw RF-data were accessed and written to file for analysis and processing.

All the signal *analysis and characterization* were performed with the program: "Matlab" (The Math Works, Inc). This program is easy to use and is well suited for analyzing small data sets. Simple one and two-dimensional plots were used to characterize the signals and test the performance of the developed algorithms. Unfortunately, the Mac II version did not display gray level images. To test the effect of an algorithm on an entire ultrasound image, the algorithm was implemented as an ECAR (Echo Custom Analysis Routine) under the EchoDisp program and the entire raw data image was processed and displayed.

3.1.2 Data formats and data rates

Number of bits in the AD-converters: In intravascular ultrasound imaging, the total dynamic range requirement is approximately 80dB. However, the local dynamic range requirement is lower, approximately 55 dB. The difference between the two is due to attenuation. A Time Gain Compensation (TGC) circuit is used to compensate for the attenuation.

A rule of thumb specifies that an AD-converter covers 6 dB dynamic range per bit. This means that a minimum of 13 bits is required to digitize the signal directly and cover the total dynamic range. The local dynamic range can be covered with an 9-10 bits AD-converter, and an analog TGC-circuit is required to cover the total input range.

At the time the instrument was designed, only 8 bits AD-converters were available (20 MHz sampling rate). A dynamic range of approximately 75 dB was obtained for the RF-frontend by implementing an analog log-amp that compresses a ≈55 dB input range into the 8 bits range, and a TGC-circuit with a gain span of ≈35 dB.

The data bus is 16 bits wide. In peak detected mode, two depth locations are transferred in each bus cycle, in QD-mode the number is one.

Data format in peak detected mode: 1 x 8 bits
Data format in QD- mode: 2 x 8 bits

Radial direction: The bandwidth of the transducer determines the minimum sampling rate in the radial direction. The system is designed to handle transducers with 50% fractional bandwidth. At 20 MHz the one sided bandwidth is then ≈5 MHz. The transducers are expected to have approximately 25% fractional bandwidth, but the log-amp (and the magnitude detector) broadens the spectrum. By changing the low pass filter cutoff frequency between 2, 3, 5 and 10 MHz, it is found that 5 and 10 MHz yields the same result, while the image is distorted by the 2 and 3 MHz filters. From this the minimum sampling rate in the radial direction is set to: f_{rsMin} = 10 MHz (one sample in peak detected mode and two samples in the QD-mode).

For practical implementation reasons, the beam length is always fixed and equal to N_r = 256. To avoid marginal sampling, the sampling rate is set to f_{rs} = 20 MHz. This represents 100% oversampling at the default depth of view which is 10 mm.

Default number of radial samples: N_r = 256
Default sampling rate: f_{rs} = 20 MHz

Lateral direction: The spatial frequency content in the lateral direction is given by the beam profile. Equation 2.43 gives an estimate of the maximum lateral frequency component for stationary scatterers (circular transducer), and Equation 4.4 gives the corresponding minimum beam density to avoid aliasing:

$$N_{bMin} = 4\ k_o\ a\ =\ 219 \tag{3.1}$$

The system is designed for a beam density of 256 beams/rev, i.e. a slight oversampling.

The lateral sampling rate or pulse repetition frequency is given by:

$$f_{\phi s}\ = N_b\ f_m \tag{3.2}$$

In the system, the default beam density is 256 and the default frame rate is 15 f.p.s.

Default beam density:	$\mathbf{N_b}$	**= 256**
Default lateral sampling frequency:	$\mathbf{f_{\phi s}}$	**= 3.8 kHz**

Frame formats, data rates: One ultrasound raw data frame consists of N_b beams of N_r radial locations. Each radial location consists of one byte in the peak detected mode and two bytes in the QD-mode. This gives the following default frame formats:

Default peak detected frame format:	**64kB**
Default QD-mode frame format:	**128kB**

The frame memory board has a storage capacity of 2 MB. One frame is used for other purposes leaving space for 31 peak detected frames or 15 quadrature detected frames. The specified acquisition format with one peak detected frame on either side of the QD-frames allows storage of **maximum 14 QD-frames**.

Bus capacity limitation: The instrument is capable of transferring 2.8 MB per second to the frame memory and the display unit over the VME-bus. In peak detected mode this yields a maximum theoretical frame rate of 43.4 f.p.s., but it is limited by the motor speed which is maximum ≈33 rev/sec.). In QD-mode, the maximum frame rate drops to 21.7 f.p.s.

Maximum frame rate, peak detected mode:	$\mathbf{f_m \approx}$ **33 f.p.s.**
Maximum frame rate, QD-mode:	$\mathbf{f_m =}$ **21.7 f.p.s.**

In some experiments a higher lateral sampling frequency is required. This is accomplished by increasing the beam density while the frame rate is kept constant. Due to the limited bus capacity, the image size has to be reduced. The instrument is modified to increase the beam density from 256 to 512 and 1024 by jumper selections. The number of radial samples per beam is reduced accordingly from 256 to 128 and 64.

Possible frame formats in QD-mode:

$N_b = 256$	$N_r = 256$	$f_{\phi sMax} = 5.5$ kHz
$N_b = 512$	$N_r = 128$	$f_{\phi sMax} = 11.1$ kHz
$N_b = 1024$	$N_r = 64$	$f_{\phi sMax} = 22.2$ kHz

3.1.3 Catheters, test tank and transducers

Catheters: The *rotating mirror catheters* that come with the instrument (Cardiovascular Imaging Systems) are not well suited for the test work performed in this work: They are designed for single use only and they are subject to variations in acoustical and mechanical quality. Some catheters exhibit Non Uniform Rotation Distortion (NURD), i.e. the variations in the phase angle between the ultrasound beam and the angle sensor. This is a serious problem when signal characteristics from a specific area are supposed to be analyzed and the location from where the data is sampled, varies from frame to frame. A more reliable test setup was required which led to the design of a test tank:

Test tank: A photo of the test tank is shown in Figure 3.2. It consists of a rotating stainless steel shaft (2mm in diameter and 75mm long) mechanically connected to a motor in the proximal end. The distal tip of the shaft is cut with an angle of 40 degrees to the axis, and the surface is polished to serve as an acoustic mirror. (The grain size of the mirror surface is guaranteed to be less than 3μm, i.e. small compared to the wavelength which is 75μm.) This means that the ultrasound beam is tilted in the azimuthal direction towards the motor with an angle $\psi = 10$ degrees. This effectively eliminates internal mirror reverberations and introduces a Doppler shift for scatterers with a velocity parallel to the shaft. The transducer radiates towards the mirror, and the transducer can be rotated around its own axis and tilted in the horizontal plane. The transducer tube is fixed by set screws in a Plexiglas holder.

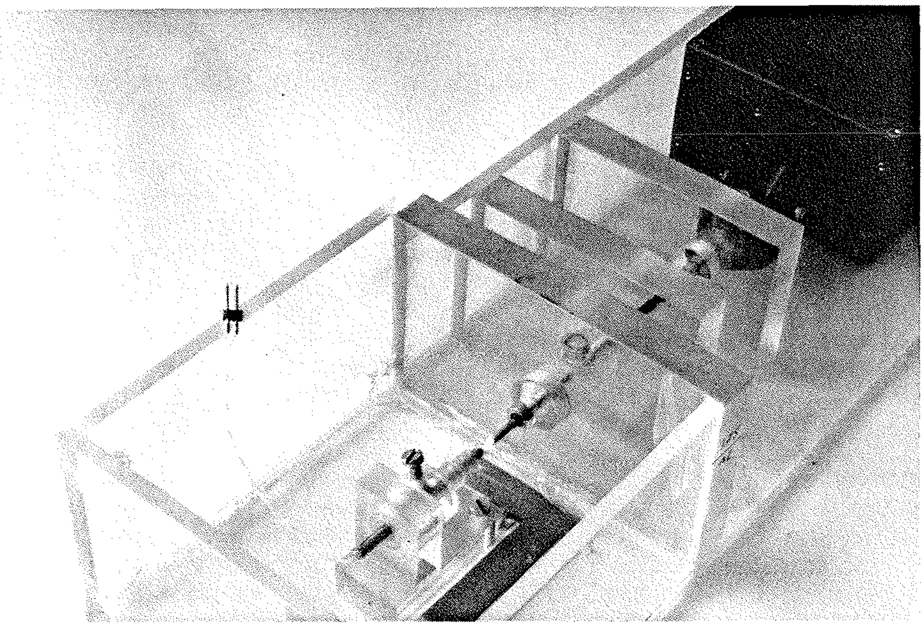

Figure 3.2 *The photo shows the test tank with the motor drive unit in the upper right corner, a rotating shaft with an acoustic mirror (specular surface) and a transducer mounted at the tip of a metal tube and directed towards the mirror. The transducer tube is mounted in a Plexiglas holder. The tube can be rotated and also tilted in the horizontal plane. Short leads connect the transducer to the TX/pre-amp.*

The mirror shaft is rigid and very stable, thereby giving no risk of non uniform rotation distortion. The life time of the transducer is much longer than the life time of a catheter with rotating parts. Approximately equal ultrasound properties can be achieved over a period of several months without any problems if the same transducer is used. Several transducers can easily be tested while other conditions are kept unchanged.

The test tank was normally filled with pure water. To mimic red blood cells, 0.5 volume percent Sephadex particles were mixed in (Sephadex G-25/Superfine, Pharmcia Fine Chemicals, Uppsala, Sweden). It was observed that the rotating mirror shaft caused a pump effect. Water was soaked towards the distal tip of the shaft from the ultrasound scan plane and transported along the shaft in the proximal direction. In some experiments, this effect was undesirable, i.e. the scatterers were supposed to be stationary. In these cases the tank was filled with 50% glycerol and 50% water to increase the viscosity.

However, the velocity of sound did also increase. At T=25°C, the velocity of sound in distilled water is 1496m/sec., in glycerol it is 1904m/sec. A linear relationship is *assumed* here, i.e. the velocity is set to: c = 1700 m/sec. in a 50/50% mixture of water and glycerol. The Sephadex particles are assumed not to affect the velocity of sound significantly due to the low concentration.

Echo from other targets than the *device under test* did in some cases generate acoustic noise. In some high PRF situations, the echo from the water surface, the bottom or the sides of the tank appeared in the sampling window. The echo from the previous pulse returned when the signal from the current pulse was sampled. Attenuating materials were tried in order to solve the problem, but without any success. Two fixes were required: 1) A redesign of the tank. The *dimensions* of the tank, the mirror shaft and the water level were selected carefully to avoid interference for the most common PRF's. 2) Echoes that still caused a problem were directed in other and less critical directions by *reflectors.*

Transducers: Five flat circular transducers (Cardiovascular Imaging Systems, Inc.) were used for testing, all from the same production batch. The *center frequency* of the five transducers was found by measuring the impedance with the transducer dipped in water. The open and short circuit resonance frequencies were measured, and the mean value was used as the center frequency "f_0".

All transducers were equipped with a matching layer. The fractional bandwidth (-6dB) was specified by the manufacturer to minimum 15%, and the radius was specified to a=0.7mm. The radius was measured with calipers under a microscope and the average value was: $a_{Meas} = 0.68$mm.

Average measured transducer frequency: $\mathbf{f_{oAve} = 19.6}$ **MHz**
Average measured transducer radius: $\mathbf{a = 0.68}$ **mm**

3.1.4 Analog receiver circuits

The total dynamic range of the system is determined by the maximum transmit power and the noise level. Patient safety regulations limit the maximum allowed acoustic power. The RF-frontend is designed for a ≈75 dB dynamic range by the TGC-circuit and the log-amp. The pre-amp has approximately the same dynamic range:

Pre-amp: The signal to noise ratio of the pre-amp is determined by the saturation level of the amplifier and the noise floor, i.e. the thermal noise and the amplifier noise. This dynamic range is calculated for some realistic values. The pre-amp used in the experiments has the following parameters (measured):

Gain	:	$G = 27.7$ dB
Bandwidth (-3 dB)	:	$BW = 50$ MHz
Noise factor	:	$F = 2$
Noise figure	:	$NF = 20 \log(F) = 6$ dB
Maximum input level, 1 dB comp. point	:	$U_{S1dB} = 40mV_{peak}$

The maximum input level is specified as the peak amplitude of a sinusoidal signal applied to the input that causes a 1 dB compression at the output. The maximum rms input level is then:

$$U_{Smax} = \frac{U_{S1dB}}{\sqrt{2}} \tag{3.3}$$

The thermal noise voltage from the transducer is given by the following equation when the transducer is loaded with a resistance equal to the real part of the transducer impedance [Motchenbacher, 1973]:

$$U_{Nxd} = \sqrt{4kTR\Delta f} \tag{3.4}$$

where "k" is Boltzmann's constant, "T" is the temperature, "R" is the transducer resistance and "Δf" is the noise bandwidth [Motchenbacher, 1973].

The pre-amp contributes with shot noise which is also proportional to the square root of the bandwidth. If the amplifier noise is modeled as a noise voltage at the input of a noise free pre-amp, the total input noise voltage will be:

$$U_N = U_{Nxd}\ F \tag{3.5}$$

The signal (rms sinusoidal) to noise (rms Gaussian) ratio is then given by:

$$\frac{U_{Smax}}{U_N} = \frac{\frac{U_{S1dB}}{\sqrt{2}}}{F\sqrt{4kTR\Delta f}} \tag{3.6}$$

This signal to noise ratio is tabulated in Table 3.1 for the pre-amp (U_{S1dB} = $40mV_{peak}$ and NF = 6 dB) and for the RF-frontend (50% fractional bandwidth) used in this work. The expected signal to noise ratio is also listed for a pre-amp with noise figure NF = 2 dB. Other parameters are: $4kT = 1.61 \cdot 10^{-20}$, $R = 50\Omega$.

Table 3.1 *Signal to noise ratio for the receiver circuits versus system frequency. The fractional bandwidth of the RF-frontend is set to 50%, and the maximum input level to the pre-amp is set to $40mV_{peak}$ according to the measurements. The signal to noise ratio is also listed for a pre-amp with the same saturation level, but with only 2 dB noise figure.*

f_o	Δf	$\frac{U_{Smax}}{U_N}$ (NF=6dB)	$\frac{U_{Smax}}{U_N}$ (NF=2dB)
10 MHz	5 MHz	77 dB	81 dB
15 MHz	7.5 MHz	75 dB	79 dB
20 MHz	10 MHz	74 dB	78 dB
30 MHz	15 MHz	72 dB	76 dB

The pre-amp is realized with a *Low Noise Amplifier* from AVANTEK, the INA-01170. This amplifier is supposed to have a noise figure of 2 dB at a gain 32.5 dB. The noise figure of the entire pre-amp is *measured* to 6 dB. It is therefore assumed that the protecting network at the input (a diode) contributes with 4 dB.

The dynamic range of the system is approximately 74 dB at 20 MHz system frequency.

TGC: The TGC-circuit is realized with the AIT-100 from Acoustic Imaging. The performance of the TGC-circuit is frequency dependent, the available gain adjustment range drops as the frequency increases. The range is measured to:

Gain span at 10 MHz system frequency: $\Delta G \approx$ **40 dB**
Gain span at 15 MHz system frequency: $\Delta G \approx$ **36 dB**
Gain span at 20 MHz system frequency: $\Delta G \approx$ **33 dB**
Gain span at 30 MHz system frequency: $\Delta G \approx$ **24 dB**

Log-amp: The log-amp is realized with the logarithmic amplifier TL-441C from Texas Instruments. This circuit contains four 30 dB log stages. The four stages may be interconnected to obtain a theoretical input voltage range of 120 dB for DC to 40 MHz. Two stages are interconnected in the log-amp on the RF-frontend to obtain a maximum input range of ≈60 dB. This input voltage range decreases with increasing frequency, measured values are:

Log-amp dynamic range (10 MHz):	**LDR ≈ 60 dB**
Log-amp dynamic range (15 MHz):	**LDR ≈ 60 dB**
Log-amp dynamic range (20 MHz):	**LDR ≈ 55 dB**
Log-amp dynamic range (30 MHz):	**LDR ≈ 50 dB**

Due to saturation in the log-amp and due to electronic noise, the total dynamic range of the RF-frontend (log-amp dynamic range plus TGC-gain span) is less than one would expect from the tabulated measurements. A typical performance of the RF-frontend is plotted in Figure 3.3. The output of the peak detector is plotted versus input level for a 20 MHz sinusoidal signal. The gain can be varied within 33 dB and the total input range is approximately 75 dB.

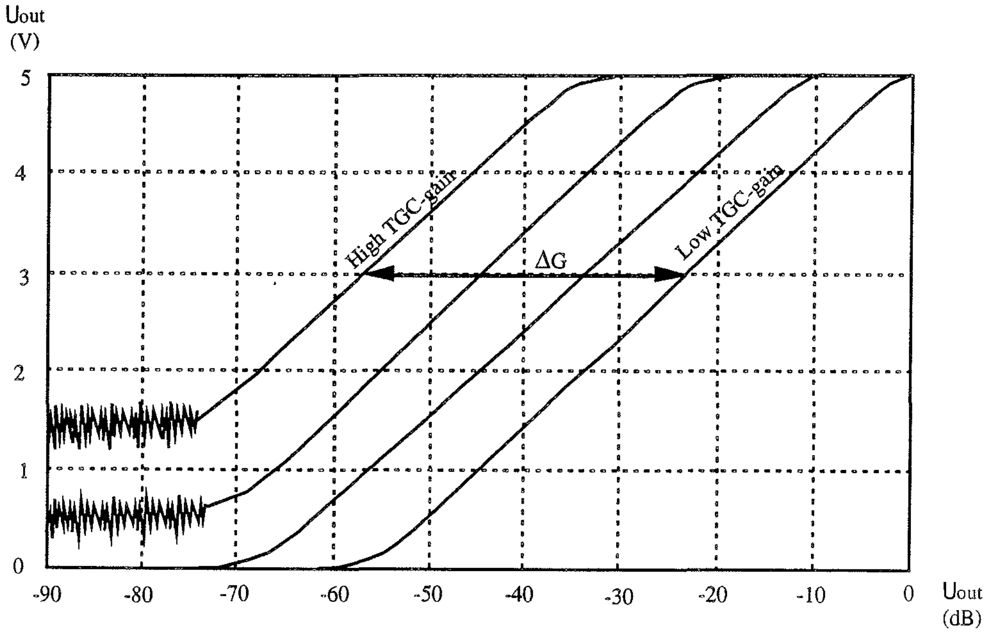

Figure 3.3 *Typical plots of the input/output characteristics of the RF-frontend board for a 20 MHz sinusoidal input. The local input range for the log-amp is approximately 55 dB and the adjustable range for the TGC is ΔG≈33 dB. The total input range is approximately 75 dB.*

Quadrature Demodulator: The quadrature demodulator is realized by two mixers and two low-pass filter channels: the in-phase and the quadrature component. The RF-band-pass signal is mixed with two local oscillators at 20 MHz with 90 degrees phase difference, see Figure 2.1. The mixers are the TAK-3H from Minicircuits (diode mixers). A description of the implementation as well as a discussion of the most critical aspects is given in the following:

Mixing: The *phase difference* of the two oscillators should ideally be 90 degrees (see gain, phase and offset errors below). A practical approximation to this can be obtained by two flip flops and an input clock frequency that is four times higher than the output frequency. As no 80 MHz clock was available on the Acquisition board, the following solution was selected: A 20 MHz oscillator was fed directly to one of the mixers. The same oscillator was fed to the other mixer through a delay line, a 2.6 meter long coax cable. This cable length was supposed to give 92.5 degrees phase shift (a margin for adjustment was built in).

The *duty cycle* of the two clocks should ideally be 50% in order to eliminate *even* harmonic components in the spectrum. The second order harmonic component in particular, represents a risk of undesired mixer products to occur. The log-amp broadens the spectrum, and frequency components that might pass the band-pass filter may be mixed down to the base band.

The second harmonic component (and all even components) is very sensitive to deviations in the duty cycle from 50%: At 49% the second harmonic component is only 30.1dB below the fundamental component according to the Fourier coefficients, at 47% duty cycle it is 20.6dB below. The duty cycle is measured (with an oscilloscope) to 49%, and the second harmonic component is measured (with a spectrum analyzer) to be 27dB below the fundamental.

Low-pass filtering: The low-pass filters are supposed to allow the desired signals to pass through and reject all higher frequency components. In order to let a *pulse* pass through without distortion, the filters should ideally have constant gain and linear phase over the relevant pass band. The two channels should ideally be identical.

Low-pass filters with discrete components were implemented. A filter bank consisting of four (sixth order) low-pass filters on each channel was realized. The cutoff frequencies were: 2, 3, 5 and 10 MHz. These filters did not suppress the undesired mix products sufficiently. A filter module with cutoff frequency 10.7 MHz (PLP-10.7 from Minicircuits) was therefore inserted in front of each of the filter banks. This modification was sufficient.

Gain, phase and offset errors: In a practical situation, it is not possible to obtain identical performance of the two channels. *Gain differences* occur in the mixers, the low-pass filters, the amplifiers and/or in the AD-converters. There are two reasons that *phase differences* occur: One is: The phase lag between the two local oscillators deviate from 90 degrees. The other is: A phase difference in the low-pass filter channels. *Differences in offset* result from DC-drift in the amplifiers and/or AD-converters.

Effect of channel differences: By applying a sinusoidal signal "s(t)" with constant amplitude and frequency to the input of the quadrature demodulator, the output is supposed to describe a circle in the complex plane. The magnitude will be constant as well as the angular velocity. This is illustrated in Figure 3.4(a) where the output signal is shown in the upper panel and the corresponding Fourier transform "S(ω)" is shown in the lower panel.

Phase and/or *gain* differences between the in-phase and quadrature component cause the vector to describe an ellipse instead of a circle, see the upper panel of Figure 3.4(b). Gain differences generate an ellipse whose axis are parallel with the real and imaginary axis. Phase differences cause a rotation of the axis of the ellipse. In both cases the result is ripple in the magnitude with a frequency equal to twice the frequency difference between the input signal and the local oscillator. This can be described by a distortion free signal in addition to an error signal, which is represented by a complex vector rotating in the opposite direction with the same angular velocity. In the frequency domain, this error signal will appear as a mirror frequency component, see the lower panel of Figure 3.4(b).

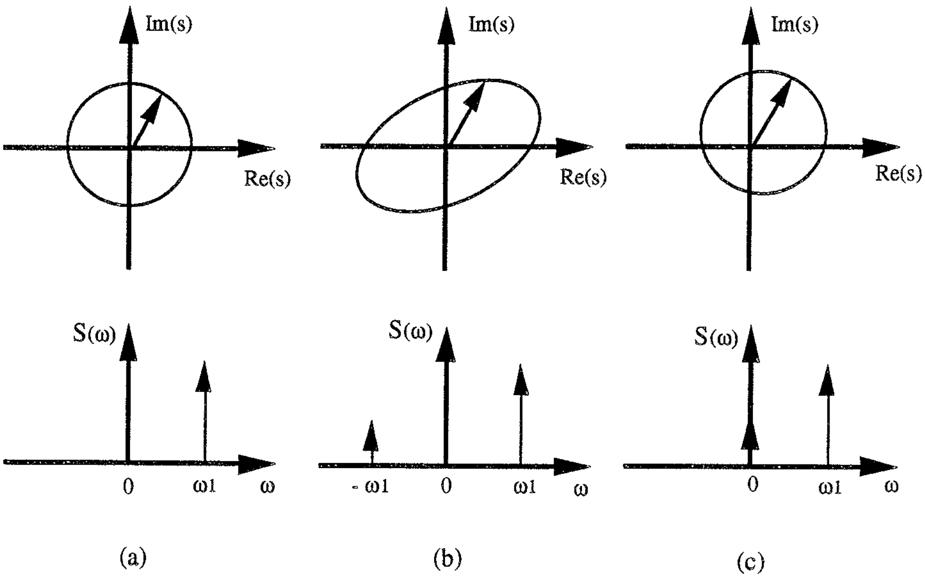

Figure 3.4 *The effect of gain, phase and offset differences between the in-phase and the quadrature channel for a constant amplitude and constant frequency sinusoidal input. All errors cause ripple in the magnitude.*
(a) Identical channels. The signal describes a circle (centered in origin) in the complex plane.
(b) Gain and/or phase differences introduce an ellipse centered in origin. The error signal is a mirror frequency component.
(c) Offset differences introduce a shift in the center of the circle. The error signal is a DC-component.

Offset difference between the two channels cause the center of the circle to be shifted from the origin, also resulting in ripple in the magnitude. Viewing this as an error signal in addition to an offset-free signal, the error signal is a constant complex value, a DC component in the frequency domain. See Figure 3.4(c).

Simulations: A simulation was performed to quantify these effects. A complex signal was described by two sinusoidal components at the same frequency, 90 degrees out of phase. The peak to peak ripple in the magnitude was found for various deviations in amplitude, phase and offset (DC-level). The ratio of the magnitude ripple and the maximum magnitude is denoted "MR_{pp}". The amplitude difference is denoted "ΔA" and specified in dB. The phase error is denoted "$\Delta\alpha$" and specified in degrees. The offset error is denoted "ΔZ" and specified in percent of maximum in-phase or quadrature amplitude. Some results are listed in Table 3.2.

Measurements: A sinusoidal signal at 21 MHz was applied to the input of the quadrature demodulator. The ripple was measured to 9.7% . The gain, phase and offset differences were measured to: ΔA = 0.2 dB, $\Delta\alpha$ = 1.5 degrees and ΔZ = 3.3%. Inserting the latter three values into the simulation model gives: MR_{pp} = 8.6 %. These results indicate that the ripple is caused by an integral effect of the three errors.

Conclusion quadrature demodulator: The implemented quadrature demodulator serves its purpose: to convert the real valued band-pass RF-signal to a complex base band RF-signal. The demodulator has a 60dB dynamic range (defined as the ratio of the maximum single tone output value versus maximum intermodulation products). This is more than sufficient for the 8 bits AD-converters. Deviations in the in-phase and quadrature component gain, phase and offset cause a maximum 10% peak to peak ripple in the output magnitude for a single tone input.

Table 3.2 *Relative peak to peak ripple in the magnitude of a complex vector versus deviations in in-phase and quadrature component: amplitude ΔA, phase $\Delta\alpha$ and offset ΔZ.*

ΔA = 0.1 dB	MR_{pp} = 1.3 %
ΔA = 0.5 dB	MR_{pp} = 5.5 %
$\Delta\alpha$ = 1 deg	MR_{pp} = 2.2 %
$\Delta\alpha$ = 5 deg	MR_{pp} = 8.7 %
ΔZ = 0.8 %	MR_{pp} = 1.8 %
ΔZ = 3.9 %	MR_{pp} = 7.9 %

3.1.5 EMI-protection

Two significant EMI-sources were identified in the initial testing:

> Broad band, partially correlated electromagnetic radiation from the digital activity in the instrument. The radiation was strongest during data transfer on the bus.
>
> A narrow band telecommunication transmitter radiating in the 27 MHz band. It was located in the neighborhood of the facility and radiated for some seconds, with intervals in the range from seconds to minutes.

The latter EMI-source was eliminated by monitoring the transmitter with a spectrum analyzer and a simple antenna. Data acquisition was performed when the transmitter was inactive.

The broad band digital noise was suppressed below the thermal noise level by reducing the radiating power and by making the instrument less susceptible:

Radiation power reduction: The instrument is *not* enclosed in a shielded cabinet. One option was to perform proper shielding and cabling, but this is time consuming, and other solutions were tried first and this was found to be sufficient. The digital noise radiation is strongest during image-transfer on the bus. Interference from this noise was effectively reduced by inhibiting data transfer on the bus during sampling. At the default frame rate and beam density, this represents a 5% waste of bus capacity.

Susceptibility reduction: The transducer leads were made as short as possible. In a few tests, a standard catheter of length 65cm (acting as an antenna) was used. The problem was solved by cutting the leads at the distal tip, and solder new ≈20 cm long twisted leads to it. Most of the testing was performed in the test tank shown in Figure 3.2 where the transducer was connected to the pre-amp with ≈20 cm long leads.
The pre-amplifier was mounted directly on the RF-frontend board and connected electrically with a 10 cm long coax. This eliminated the ≈4 meter long cable between the instrument and the pre-amp. This cable contains the receiver signal which picks up interference, primarily through cross talk and ground loop noise.

3.1.6 AD-converter errors

Two serious problems related to the AD-converters were discovered during testing of the quadrature demodulator.

1) "Wild points". In a data set of 64 kB, a few (up to ≈10) samples were completely wrong. This appeared as white pixels in the image. The AD-converters did not perform according to the specification (too slow at 20 MHz sampling frequency).

2) Offset error. Even with the reference voltage and the input voltage carefully adjusted, an offset error of up to 10 LSB was registered for a mid-range DC-input. Large variations between samples of the same component were observed. The error increased with temperature and with the sampling frequency.

The instrument was originally designed with the MP7684LD from Micro Power Systems, but this component was replaced with the pin-compatible HI-5700A from Harris. This device performs acceptable and was used in all experiments. The AD-converter errors are listed in Table 3.3.

Table 3.3 *The offset error for a mid range DC-input and the "wild point" error for the tested AD-converters.*

	fs = 20 MHz		fs = 10 MHz	
	Offset error	Wild points	Offset error	Wild points
MP7684LD	7 LSB	No	2 LSB	No
MP7684AKN	9 LSB	No	2 LSB	No
MP7684AJN	11 LSB	Yes	no meas.	No
HI-5700A	4 LSB	No	3 LSB	No

3.1.7 Vascular hydromechanical model

A pulsating flow was required in some experiments. This was obtained by introducing the catheter in a cardiovascular hydromechanical model developed by R. Aaslid (Department of Biomedical Engineering, University of Trondheim). This model simulates parts of the circulation system in a 70 kg young man, see Figure 3.5. It consists of the left atrium, the left ventricle, the compliant aorta and six other compliant chambers (only two were used in the tests). Except for the atrium, all these parts are made of elastic rubber with very realistic compliance and acoustic properties. The flow returns to a large plastic tube that acts as the venous system. The design of the model is based on the work done by A.O. Brubakk and R. Aaslid [Brubakk 1978].

An air pressure control unit allows adjustment of the heart beat rate, the rise and fall time of the systole, the pulse shape (to a certain degree) and the systolic and diastolic pressure. In addition, the vascular resistance can be changed. This makes it possible to generate realistic peripheral and coronary flow situations in one and the same test.

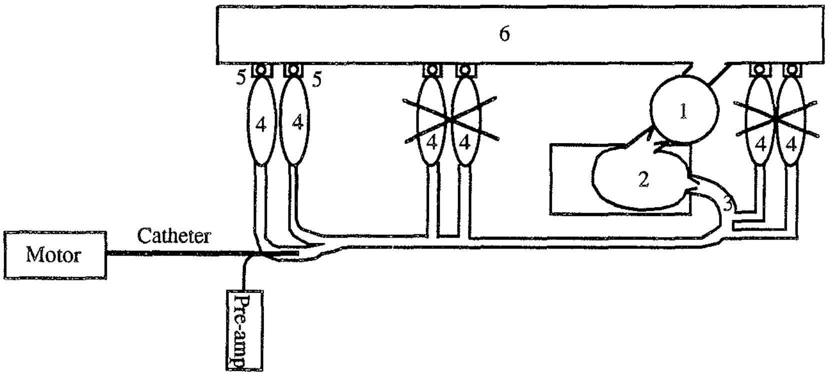

Figure 3.5 *Hydromechanical model of cardiovascular system: 1, atrium; 2, ventricle; 3, aorta; 4, compliant chamber; 5, peripheral resistance; 6, venous system.*

3.2 Measurements for model verification

3.2.1 Beam opening angles

Valuable information about the transducer would have been obtained if the far field two way angular sensitivity function $A(\phi,\phi',\psi,\psi')$ could have been measured by scanning a point scatterer in the angular directions in the far field. This is very difficult to do for at least two reasons:

1) It is practically difficult to *make* and *handle* a target that approximates a point scatterer in size (λ = 75 µm in water at 20 MHz), and further to fix it to a device that does not contribute to the signal.

2) The total dynamic range of the instrument and the transducer is not sufficient. The echo from a target that is much smaller than the wavelength will not exceed the noise floor when the target is located in the side lobes of the beam.

Alternatively, a less informative, but still interesting test is to measure the beam *width* without caring about absolute signal levels in the main lobe and in the side lobes. This can be realized by using a larger target, for example a needle:

Test setup 3.1:
The test tank was filled with water and the head of a needle was located 5mm from the mirror axis. The thickness of the needle was 350 µm (in the azimuthal direction) and the width was 600 µm (in the lateral direction). The offset between the center of the mirror and the transducer was 1.4 mm, which means that the needle was located 6.4 mm from the transducer surface (within the "transition" region, see Figure 2.4). During imaging, the needle position was adjusted slightly to find a position where the pattern of the main lobe, the zeros and side lobes appeared on the screen. The number of cycles in the transmitted pulse was set to 10 in order to approximate CW-operation. The log-amp was not used.

Results: The raw data from the instrument was transferred to the computer for display and measurements. It was possible to detect the main lobe, the first side lobe in all measurements, and in some cases also the second side lobe.

The *measured* two sided opening angle "Ω_{Meas}" was found and averaged for all 5 transducers for the first zero and the first side lobe:

$\Omega_{Meas1zero}$ = 8.6 degrees
$\Omega_{Meas1sidelobe}$ = 12.7 degrees

The corresponding two sided opening angle "Ω_{Calc}" was *calculated* from Equation 2.24 with the following parameters: f_{0Ave}=20MHz, a=0.68mm and c=1500m/s:

$\Omega_{Calc1zero}$ = 7.7 degrees
$\Omega_{Calc1sidelobe}$ = 10.7 degrees

The difference between the measured and calculated angles is most reasonably explained by an appodization effect in the transducers. The transducers were inspected under a microscope, and it looked like the mounting procedure could hinder the front surface along the circumference to move freely.

The *measured* opening angles are 12% and 19% larger than *calculated* angles for the first zero and the first side lobe respectively. This is probably due to appodization.

3.2.2 Power spectrum in the lateral direction, stationary scatterers.

The power spectrum in the lateral direction for a large amount of stationary scatterers is measured. This spectrum is modeled by Equation 2.42 and illustrated in Figure 2.8. The maximum spatial frequency component is supposed to be:

$$k_{\phi Max} = 2k_o\, a \tag{3.7}$$

The purpose of this test is to see how the modeled spectrum corresponds to the measured spectrum.

Test setup 3.2:
The test tank was filled with a mixture of 50% water and 50% glycerol to reduce the mirror shaft "pump effect". Sephadex particles were used to mimic stationary scatterers. The data were acquired shortly after the motor had started to obtain approximately stationary Sephadex particles .
The number of burst pulses was 4, beam density N_b=1024, the number of radial samples N_r=64, the frame rate f_m=15 f.p.s. and the log-amp was not used.
Data were sampled in a depth between 6.4 and 8.9mm from the transducer surface (in the transition region).

Results: The power spectrum in the lateral direction was calculated from circles consisting of 1024 lateral samples. A Hanning window was used to weight the input sequence before the Periodogram estimator was applied (4096 points). This procedure is denoted Power Spectrum Estimate: PSE{•}. To reduce the variance in the stochastic spectrum, five spectra from adjacent depths around 7mm were averaged. The result is plotted in Figure 3.6. The expected spectrum according to Equation 2.42 is also shown. The latter is based on the following parameters: a=0.68mm, c=1700m/s and f_o=20MHz.

This test was performed for all 5 transducers. By varying the transducer radius of the model, the best fit to the measured curve was found. This transducer radius is denoted *reverse calculated transducer radius* "a_{RevPow}" and the average value is: a_{RevPow} = 0.64 mm. This is based on the assumption that the velocity of sound in a mixture of water, glycerol and Sephadex is c=1700 m/sec.

The reverse calculated transducer radius "a_{RevPow}" is ≈6% smaller than the measured value a_{Meas} = 0.68mm, probably due to appodization.

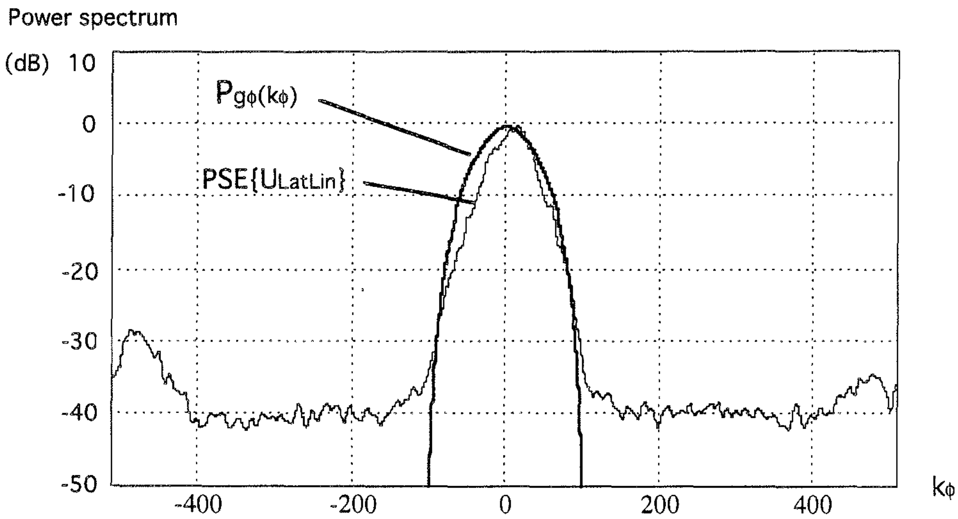

Figure 3.6 *Measured power spectrum in the lateral direction from approximately stationary Sephadex scatterers in a mixture of water and glycerol. Five spectra from adjacent depths around 7mm were averaged to reduce the variance.*
Calculated power spectrum according to Equation 2.42 with the following parameters: a=0.68mm, c=1700m/s and f_o=20MHz is shown for comparison.

3.2.3 Power spectrum in the lateral direction, blood

The Doppler shift and frequency broadening effect from blood mimicking scatterers is *illustrated* by the following test:

Test setup 3.3:
A 45 cm long rubber hose with inner diameter 5 mm was mounted horizontally with one end into a water tank. A rotating mirror catheter (Cardiovascular Imaging Systems) with beam tilt angle $\psi \approx 8$ degrees was inserted in the hose. Water containing Sephadex particles was flushed through the hose with a pump. The flow was calibrated against the pump motor voltage by collected volume measurements. The diameter of the catheter was measured in order to calculate the cross section area between the catheter and the hose. From this the average water velocity could be calculated. The tip of the catheter was located in the center of the hose to obtain symmetric flow profile.
The number of burst pulses were 4, the beam density $N_b=1024$, the number of radial samples $N_r=64$, the frame rate $f_m=15$ f.p.s. and the log-amp was not in use.

Results: The power spectrum estimates "PSE{·}" were calculated from depth r=2.2mm for three different average water velocities: 0, 20 and 50 cm/sec. The result is shown in Figure 3.7. In these measurements, only one spectral estimate was used. To reduce the variance in the display, 60 adjacent values in the (4096 points) spectrum were averaged.

The arrows indicate the *expected* mean Doppler shift according to the Doppler equation, in which the average water velocity is inserted. The *measured* Doppler shift seems to be higher than expected. These measurements are subject to large errors since the beam profile is not measured or modeled. The main purpose of this test is to *illustrate* the Doppler shift effect in a practical experiment.

3.2.4 Power spectrum in the lateral direction, near field / far field

No theoretical analysis was done to model the power spectrum in the lateral direction for scatterers located in the transducer near field (the region where practical imaging is performed for unfocused beams). However, the spectrum was *measured* for scatterers located in the near field, in order to find out whether a separate model for the near field was required or not.

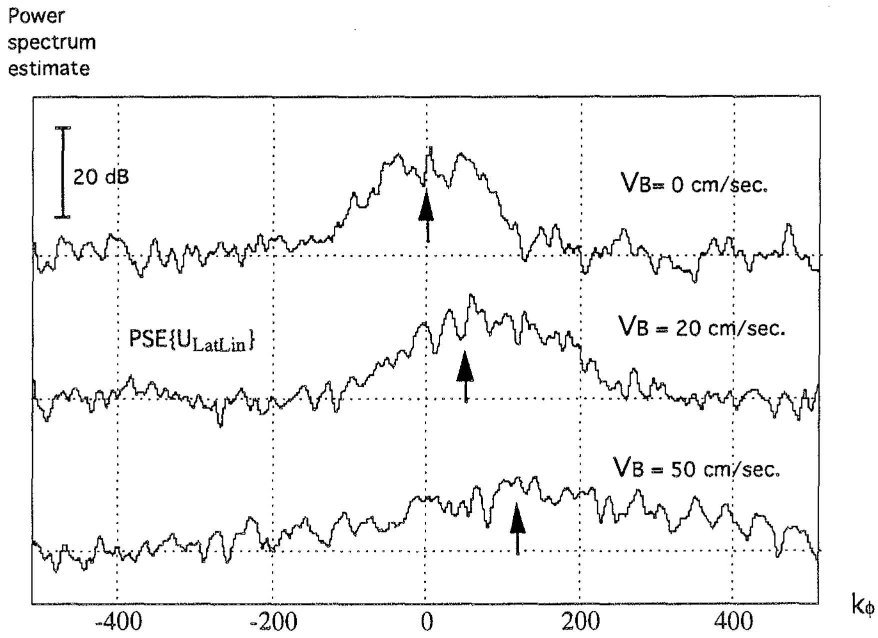

Figure 3.7 *The measured power spectrum in the lateral direction when water containing Sephadex particles flows through a rubber hose.*
The Doppler shift and frequency broadening effect is illustrated. The former seems to be higher than expected from the Doppler equation.

Test setup 3.4:
Same as "Test setup 3.2".

Result: Data were collected from circles (1024 samples) ranging from the extreme near field to the middle of the transition region (distance from transducer: 3.1mm to 9.1 mm). The power spectral estimates were calculated and several spectra from adjacent depths were averaged in order to reduce the variance.

It was not possible to detect any significant difference in the lateral power spectrum versus distance for any of the 5 transducers. This indicates that it is not necessary to modify the RF-signal model to describe the power spectrum in the near field.

3.2.5 Power spectrum in the lateral direction, PW / CW

Another important approximation in the RF-signal model in Chapter 2 is the continuous wave (CW) excitation. A simple test was performed to determine whether the power spectrum in the lateral direction is sensitive to the transmitted pulse length or not. The instrument is not capable of transmitting continuous waves, but CW-excitation was approximated by increasing the number of pulses in the transmitted burst.

> ***Test setup 3.5:***
> *Same as "Test setup 3.2", except the number of pulses in the transmitted burst was varied.*

Result: Power spectrum estimate "PSE{·}" was calculated from depth r=7mm for 1, 4 and 10 burst pulses. No significant change in the spectrum was observed. The transmitted power is significantly lower for 1 burst pulse than for 10. This means that the signal to noise ratio drops, and a smaller part of the spectrum exceeds the noise level. There may be changes of the spectrum that are not observed, especially in the high frequency range.

> **It is not possible to detect any changes in lateral power spectrum for 1, 4 or 10 pulses in the transmitted burst. This indicates that it is not necessary to modify the RF-signal model to describe the PW-mode.**

3.2.6 Power spectrum in the lateral direction, log-amp

A simulation of the power spectrum in the lateral direction from a single point scatterer is shown in Figure 2.14(b). This section describes a test where a large amount of scatterers were imaged and the power spectrum in the lateral direction was calculated:

> ***Test setup 3.6:***
> *Same as "Test setup 3.2" except that the log-amp was included.*

Results: Five power spectrum estimates from adjacent depths around r=7mm were averaged. The result is shown in Figure 3.8. The spectrum from the single point scatterer is shown for comparison, although the latter is not supposed to be a description of the general spectrum. (The following parameters were used when the single scatterer spectrum was calculated: a=0.68mm, c=1700m/s, f_0=20MHz and the "tanh"-compression function described in Equation 2.49). A frequency broadening effect is observed with the log-amp included. The following conclusion can be made by comparing the spectrum in Figure 3.8 with the spectrum in Figure 3.6:

> **The maximum lateral frequency component in a log-compressed signal is approximately 2 times higher than the maximum lateral frequency component in a linear signal (given the dynamic range of the instrument).**

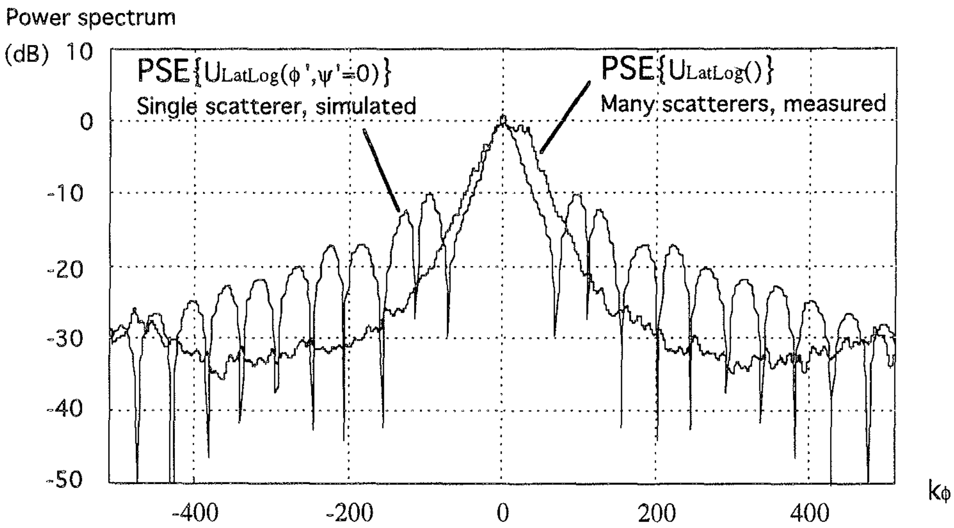

Figure 3.8 *Measured power spectrum in the lateral direction with the log-amp included. Sephadex scatterers are immersed in a mixture of water and glycerol. Five spectra from adjacent depths around 7mm are averaged.*
The calculated power spectrum from a single point scatterer, traversing through the beam axis laterally, is shown for comparison.

Chapter 4

NOISE REDUCTION ALGORITHMS

This chapter describes methods of noise detection and/or rejection. Two ways to reduce the noise in the image are considered:

1) Change the physical conditions in order to reduce the noise sources, primarily by *changing the design* of the catheter and the transducer.

2) Apply *signal processing* that reduces the noise by linear filtering or by non-linear detection and canceling.

Section 4.1 gives an *overview* of noise characteristics and methods to reduce noise by design changes or signal processing. The rest of the chapter describes methods to reduce noise by signal processing. Only the beam to beam and frame to frame modes are considered.

4.1 Overview of noise properties and possible methods of noise reduction

4.1.1 Blood and laser noise - The object noise

Noise properties:

Beam to beam: The blood velocity will cause the transit time of red blood cells and laser generated gas bubbles to be smaller than the transit time for vessel wall scatterers. The spectrum in the lateral direction will be broadened.
By tilting the ultrasound beam in the *azimuthal* direction, a component of the *blood velocity* will be introduced in the beam radial direction. A Doppler shift is introduced and the spectrum in the lateral direction is shifted in frequency proportional to the blood velocity.

Frame to frame: Scatterers moving faster than ≈0.5cm/sec. will yield an uncorrelated signal in the temporal direction. The signal from the vessel wall will normally be *correlated* in the spatial (radial and lateral) domain.
The velocity of the gas bubbles is determined by the blood velocity, the buoyancy and eventually the saline flushing velocity. If the blood velocity is not high enough to make the signal uncorrelated from frame to frame, flushing jets in the area around the scan plane may make the signal uncorrelated.

Reduction by processing:
Beam to beam: By implementing a lateral low-pass filter at each depth location, fractions of the blood noise can be rejected.
Frame to frame: Correlation estimation in the spatial and temporal domain make it possible to distinguish signal from blood/bubbles and vessel wall. The spatial average of the complex phase difference between adjacent frames yields an effective correlation estimator. The presence of the vessel wall can be detected, and blood and laser noise can be canceled.

Reduction by design:
The only way to reduce the back scattered intensity from blood relative vessel wall is to reduce the transducer frequency. Gas bubbles from laser ablation cannot be avoided, but the bubbles can to a certain degree be inhibited in reaching the ultrasound image plane by saline flushing.

4.1.2 Reverberations

<u>**Mirror leakage reverberations**</u>

Noise properties:
Beam to beam: The phase is constant and the signal is a narrow band LP-signal. Misalignments in the mirror may cause the degree of leakage to vary with the angular position of the mirror.
Frame to frame: Constant phase.

Reduction by processing:
Beam to beam: The complex mean value in the lateral direction from the vessel *wall* signal will be located at the origin. The complex mean value of a *mirror leakage*

reverberation will not be located at the origin. This difference can be detected, and a mean-value estimate subtracted to cancel the reverberation.
Alternative: a lateral high pass filter will pass the vessel wall signal through with some distortion while reverberations are suppressed.

Reduction by design:

To inhibit acoustic power to leak outside the mirror, the size of the mirror should be large enough to cover the entire beam. This can be accomplished by reducing the size of the transducer, but this also reduces the lateral resolution. With a given catheter dimension, a maximum transducer size is preferable. The beam can also be narrowed at the mirror surface by focusing. The transducer can be curved or a lens can be placed on the transducer surface.

Strut reverberations

Noise properties:

Beam to beam: The phase of the signal in the lateral direction depends on the shape of the strut. With a cylindrical shape, the phase will change as the beam scans, and it is difficult to distinguish this signal from a vessel wall signal.

Reduction by design:

The material, size and shape of the strut can be manipulated to minimize the reflection from it. In order to reduce the reverberations and the shading effect of the strut, the best would be simply to remove it and use the *rotating transducer and mirror catheter*.

Protecting tube reverberations

Noise properties:

Beam to beam: If the protecting tube is concentrically located around the catheter, the received echo will have constant phase independent of the angular direction of the beam. The quadrature demodulated signal will be *constant in amplitude and phase*. In case of deviations from this idealized situation, the complex signal will be a narrow band LP-signal.
Frame to frame: Constant phase and amplitude.

Reduction by processing:

Same as for *mirror leakage reverberations*.

Reduction by design:

The thickness of the tube and the acoustic impedance of the material relative saline/blood (assumed the same) determine the reflected power. The tube should be as thin as possible and the impedance as close as possible to saline/blood.

Internal mirror reverberations

Reduction by design:

Reverberations from the mirror is effectively reduced by proper polishing of the surface and by tilting the beam a few degrees (5-10) away from the transducer. Snell's law of total reflection is approximately satisfied this way.

Tissue reverberations

Noise properties:

Beam to beam: Due to multiple reflections between two specular surfaces, the received signal will be more sensitive to the beam angle than the primary echo. A "diamond effect" may cause the tissue reverberations to fluctuate more than the desired signal. A lateral low-pass filter may reject such reverberations.

Reduction by design:

Reverberations from the vessel wall and tissue structures can be reduced by inserting an attenuating medium between the transducer and the lumen. The desired signal from the vessel wall has to pass this medium twice, while tissue reverberations have to pass at least four times. If present, these reverberations appear at a depth equal to twice the depth of the reflecting structure (primarily the vessel wall surface or calcified plaque). This will normally be outside the most interesting range which is the lumen and vessel wall.

4.1.3 Side lobes

Noise properties:

Signals received from the side lobes cannot be distinguished from signals received from the main lobe.

Reduction by design:

Side lobes from transducers cannot be avoided, but the side lobe level can be reduced at the expense of main lobe width by appodization. Uniform excitation of the transducer surface causes minimum main lobe width and maximum side lobe level.

4.1.4 Uncorrelated electronic noise

Noise properties:

Beam to beam: The correlation length of the filter operation in the radial direction is short compared to the interval between lateral samples. The noise is uncorrelated in the lateral direction.
Frame to frame: Uncorrelated.

Reduction by processing:

Beam to beam: The uncorrelated electronic noise power can be reduced by lateral oversampling and low-pass filtering.
Frame to frame: Averaging in the temporal direction by implementing a low-pass filter at each spatial location will also reduce the electronic noise power.

Reduction by design:

By careful impedance matching between the transducer and the pre-amplifier, an optimal signal to noise ratio can be achieved for one particular amplifier. By selecting the proper components and operating conditions, a pre-amp noise figure of less than 3 dB is realistic. This means that the amplifier contributes with less noise power than the source resistance, and there is little to gain by pushing the noise figure further down.
Both the thermal and the amplifier noise power are proportional to the bandwidth of the receiver. The receiver bandwidth should be matched to the desired signal bandwidth (which depends on the transmitted pulse and the transducer) in order to minimize electronic noise.

4.1.5 Electromagnetic Interference (EMI)

Noise properties:

Beam to beam: Broad band noise from internal equipment is uncorrelated or partially correlated. Lateral oversampling and averaging as described under "Uncorrelated electronic noise" will effectively reject uncorrelated interference. Partially correlated interference will be less effectively reduced.

Frame to frame: Same as above, but in the temporal direction instead of in the lateral direction.

Reduction by design:

Protection against electromagnetic interference (EMI) should be done at two levels: 1) The instrument should be properly shielded and protected to reduce *radiation*. 2) The catheter and pre-amp should be designed for low EMI-*susceptibility*.

1) Radiation: Radiation from digital equipment can be reduced in many ways. Low radiation design should be included at all levels of the instrument. Some important factors are: The digital components should not be faster than necessary (minimize rise and fall times). Careful layout (ground plane and routing) should minimize current loops. Cables should be carefully shielded and properly fed through cabinets. The power supplies should be carefully routed. All digital electronics should be put in a metal enclosure with holes and slots as small as possible (much smaller than the wavelength of the highest frequency component of the radiation).

2) Susceptibility: In order to protect the patient against failures in the equipment, galvanic insulation is required between the catheter and the instrument. This makes low susceptibility to radiation a challenge. Common mode noise voltages between the catheter (patient) and the instrument will be converted to differential mode voltages. At the intravascular frequency range (10-50MHz), it is difficult to design insulation circuits with high common mode rejection ratios.

To protect the transducer leads in the catheter against differential mode noise pickup, proper cabling is required. Coaxial cables will give high protection and have stable and well defined characteristic impedance properties. The shielded twisted pair is the next best option, but the characteristic impedance properties are not so good.

The rest of this chapter describes four algorithms for noise reduction. Blood noise, mirror leakage reverberations and uncorrelated electronic noise are treated in the lateral direction. Blood noise is also analyzed in the temporal/spatial domain. This is summarized in Figure 4.1 where *noise properties* (above dotted line) and *reduction by processing* (below dotted line) methods are listed.

	Blood noise	Mirror leakage reverberations	Uncorrelated electronic noise
Sample to sample		Specular/ deterministic	
(radial)		Cross correlation, detection and canceling	
Beam to beam	Frequency shift Frequency broadening	Constant phase	Uncorrelated
(lateral)	Beam tilting and lateral LP-filtering (4.2)	Lateral detection and canceling (4.4)	Lateral oversampling and LP-filtering (4.3)
Frame to frame	Uncorrelated for $V_B>0.5$cm/sec.	Constant phase	Uncorrelated
(temporal)	Phase difference, detection & canceling (4.5)		Temporal oversampling and LP-filtering

Figure 4.1 *This figure summarizes the noise properties of blood noise, mirror leakage reverberations and uncorrelated noise. The methods to reduce the noise in the sample to sample, beam to beam and frame to frame mode are listed. The shaded blocks indicate the methods that are described in the chapter.*

4.2 Blood noise reduction by beam tilting and lateral LP-filtering

It is found that the spectrum from blood in beam to beam mode differs from the spectrum from the stationary vessel wall in three ways: By a frequency *shift*, a frequency *broadening* and *reduced amplitude*. The broadening effect is caused by *reduced transit time* through the sample volume, and by the blood *velocity distribution* over the sample volume. To be able to describe this frequency diversity effect, the blood velocity should be known. Then blood noise reduction by frequency selective filtering or detection and canceling can be applied.

4.2.1 Phasic blood velocity and velocity profiles

Phasic blood velocity: The phasic blood velocity is highest in the aorta ascending, typical values are < 100 cm/sec. [Nichols 1990]. Systolic flow dominates. As the distance from the heart increases and the blood vessels branch off, i.e. the cross section area of the arterial tree increases, the blood velocities will decrease.

In the *peripheral arteries* like the femoral and the iliac artery, typical peak values around 40-80 cm/sec. are reported [Nichols 1990], [Fronek 1989]. There are large variations in what is normal. Close to the heart, the pulsation is also at its maximum. Due to compliance and vascular resistance, a filtering effect reduces the pulsation. The diastolic flow increases at the expense of systolic flow as the distance from the heart increases.

The situation is different in the *coronary arteries*. The vascular resistance is high in the systole and low in the diastole. This causes the main coronary flow to be diastolic. The reason for this is the fact that the coronary arteries are distributed in the cardiac muscle and get compressed during the systole, the vascular resistance increases. This effect is more noticeable in the left ventricle than in the right due to higher pressure in the left ventricle. Typical peak velocity in normal coronary arteries is 60 cm/sec.

A typical phasic velocity curve from a human peripheral artery is shown in Figure 4.2(a). This plot is obtained by extracting the spatial maximum from a Doppler spectrum measured with the *CFM-750* scanner form Vingmed Sound (Horten Norway).

Figure 4.2(b) shows a typical phasic velocity curve from a human coronary artery. This plot is obtained by extracting the spatial maximum from a Doppler spectrum presented in a brochure of the *FloMap Doppler Ultrasound System* from Cardiometrics (USA).

Reverse flow may occur in the peripheral arteries while it rarely occurs in coronary arteries.

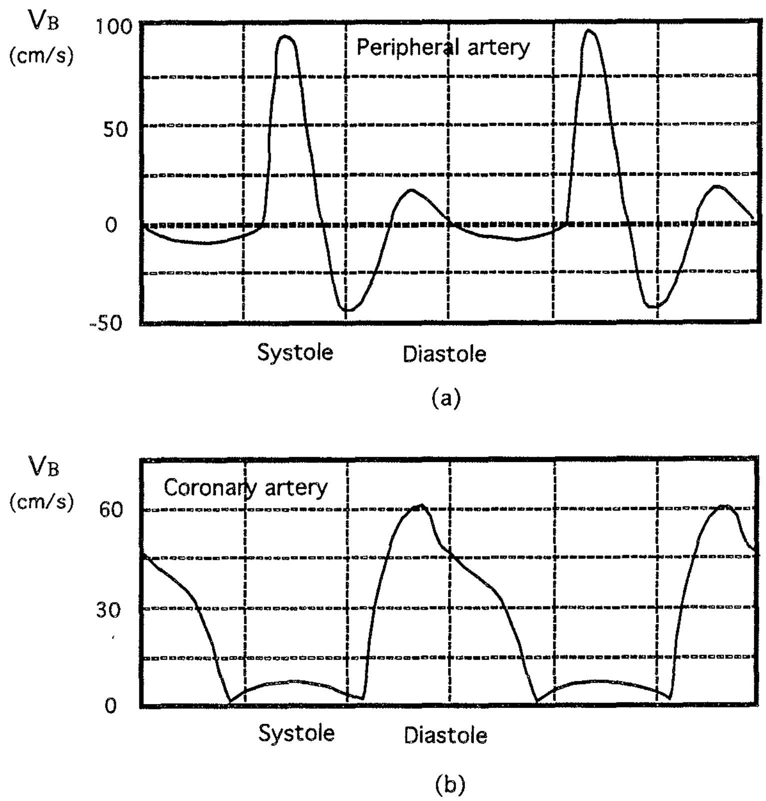

Figure 4.2 *(a) Typical phasic blood velocity in a human femoral artery. The flow is primarily systolic, and the compliance causes an oscillatory flow pattern.*
(b) Typical phasic velocity in a human coronary artery. The flow is primarily diastolic.

The phasic blood velocity in the largest coronary arteries has been measured with intravascular Doppler *catheters*. Cole and Sibley describe the development of catheters with diameter 1.7mm and 1.0mm respectively [Cole 1977], [Sibley 1986]. Both use a 20MHz Doppler instrument with zero crossing detector. The size of the catheters limit the access to small and occluded arteries. The zero crossing detector yields inaccurate velocity information.

Lately, an ultrasound Doppler *guide wire* has been developed by Cardiometrics, Inc. A Doppler transducer (15 or 12 MHz) is mounted at the tip of a guide wire. Two guide wire dimensions are available: diameter 0.35mm and 0.46mm. This makes it possible to enter into much smaller arteries and even through many stenosis. A spectral analysis is performed which yields a better velocity estimate than the zero crossing detector. This method provides continuous blood velocity measurements during catheterization.

***Catheter* affecting phasic blood velocity** : Introducing an ultrasound catheter may in some occasions affect the *phasic* blood flow at the catheter tip. Folts et al. have measured blood flow in dog coronary arteries with simultaneous flow probe and Doppler catheter [Folts 1977]. The blood flow was not altered until the catheter represented a 36±10 % artificial stenosis. With unchanged flow, the phasic velocity will increase accordingly due to the reduction in cross section area. Further increasing the size of the catheter will increase the vascular resistance and the flow (and velocity) will finally drop to zero for 100% stenosis.

> **The phasic blood velocity increases proportional to the artificial occlusion caused by the catheter. As much as 40% velocity increase is expected.**

Phasic peak velocities in peripheral arteries are assumed to be -20 to 80 cm/sec. and 0 to 60 cm/sec. in coronary arteries with no catheter present. With a catheter introduced, a maximum 40 % increase is expected:

> **Phasic peak blood velocities in normal peripheral arteries *with* catheter preset: V_B = -30 to 110 cm/sec.**

> **Phasic peak blood velocities in normal coronary arteries *with* catheter preset: V_B = 0 to 85 cm/sec.**

Velocity profiles: The blood velocity *profile* can be measured in large arteries like aorta and aorta descending. In the human coronary arteries, no measurements are known to the author. Two well known fluid mechanic properties will be used to describe the expected blood velocity profile in peripheral and coronary arteries [Nichols 1990]:

1) The beam profile is approximately flat during acceleration.
2) The beam profile is parabolic when stationary laminar flow is developed.

This can be demonstrated by a simple example. A tube is connected to a large reservoir and the flow through the tube is *constant,* see Figure 4.3. The velocity profile close to the reservoir will be flat, the liquid is accelerating due to the narrowing. Further down the tube, a parabolic flow develops and is described by the Poiseuille's equation when/if the requirements for stationary laminar flow is fulfilled (given by the Reynolds number).

When a pulsating flow like a cardiac phasic blood flow is applied, the liquid will accelerate in the entire tube during the early systole. The velocity profile will be flat in all locations. At the end of the systole, the profile is still flat close to the branch, but at the inlet depth, a parabolic profile develops. In the early diastole, a reverse flow may occur which still yields a flat profile close to the branch. At the inlet length, the flow will be reversed in the periphery and forward in the center of the tube. Blood vessels branching from the aorta approximate the situation with a small tube connected to a larger reservoir.

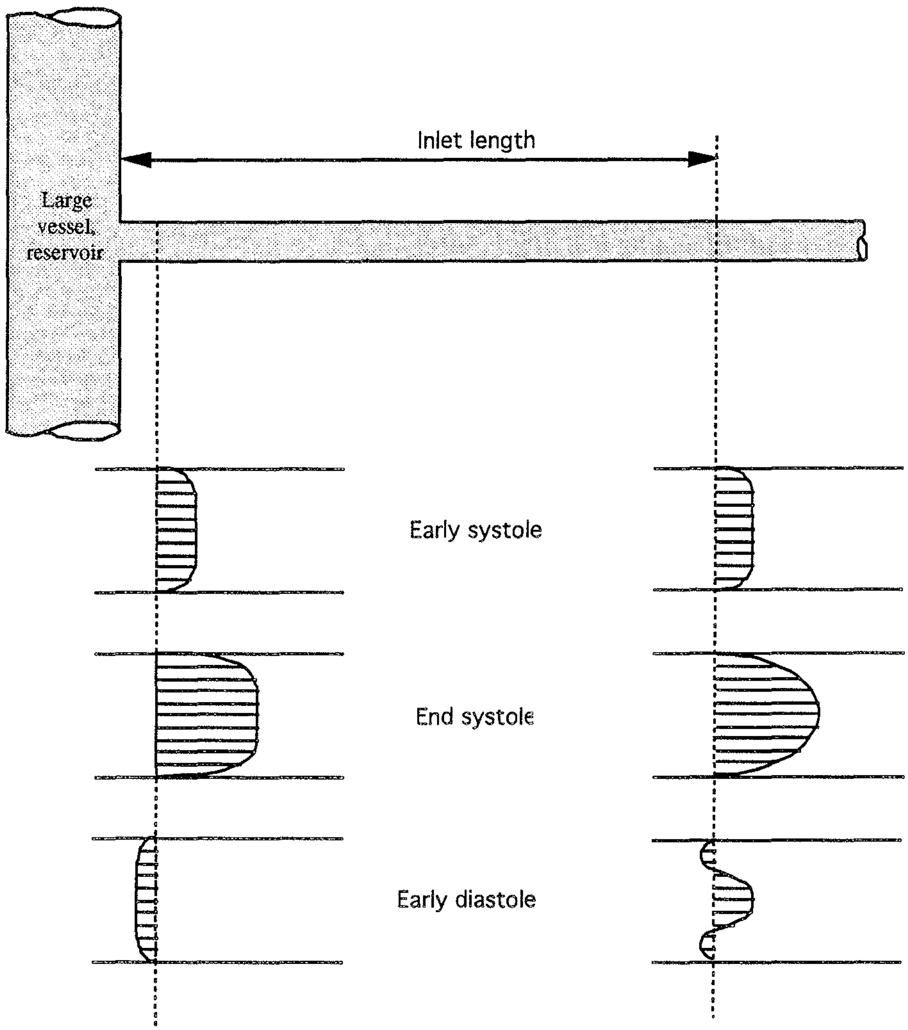

Figure 4.3 *Simple model of a blood vessel branching from aorta. The velocity profile is shown at two locations of the vessel at three instants of the cardiac cycle The velocity profile will be relatively flat close to the branch due to acceleration. At a distance equal to or larger than the inlet length, the flow profile will change during the cardiac cycle. The profile will be flat during the acceleration phase, then parabolic and may end up with flow in both directions as indicated in the early diastole (in case of reverse flow).*

***Catheter* affecting velocity profiles:** The ultrasound imaging catheter will change the velocity profile. No accurate velocity profiles will be given, but the most important profiles are illustrated schematically in Figure 4.4 where a circular catheter is located concentrically in a cylindrical tube.

In (a) the flow is directed along the catheter and stationary flow is developed. A parabolic flow profile develops. In (b), a stationary flow with parabolic profile is developed in the vessel, but the catheter narrowing causes liquid acceleration to flatten the profile. In (c) an accelerating flow along the catheter causes flat profile. In (d) an accelerating flow towards the catheter does also cause a flat profile.

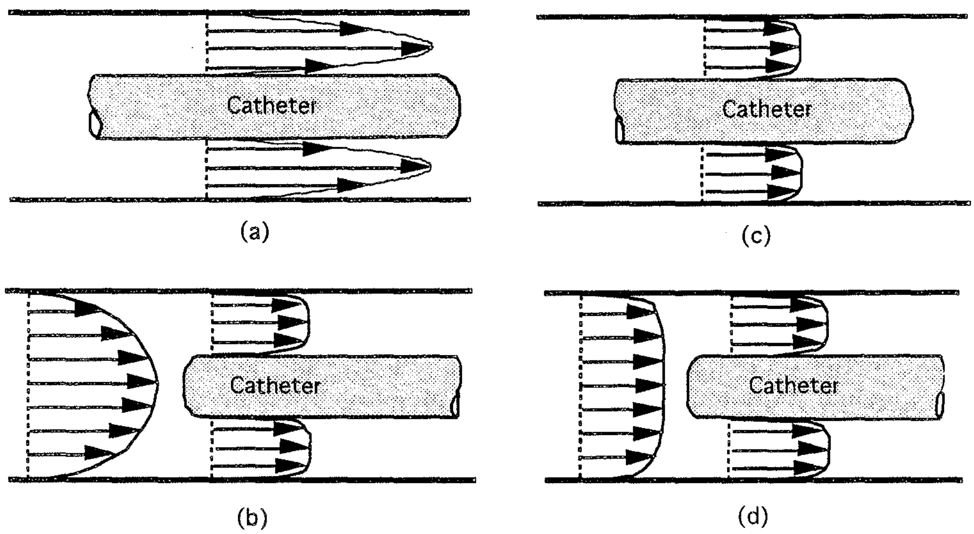

Figure 4.4 *Schematic illustration of velocity profiles with a circular catheter located concentrically in a circular tube.*
(a) Stationary laminar flow directed along the catheter: parabolic flow.
(b) Stationary laminar flow towards catheter tip. The catheter narrowing accelerates the liquid: flat profile.
(c) Accelerating flow along the catheter: flat profile.
(d) Accelerating flow towards the catheter: flat profile.

4.2.2 Frequency diversity

The frequency diversity between the vessel wall and blood signal can be found when information about the phasic blood velocity is available. The results from Section 2.3 will be used in this section. The velocity profile is assumed to be flat, i.e. the frequency diversity is independent of the spatial location of the sample volume.

In intravascular imaging, the desired vessel wall signal and the undesired blood noise are separated spatially. In a sequence of sampled vessel wall data, no blood noise is present and vice versa. The frequency diversity between the two signal types can be illustrated in the same plot, but this does not mean that the two signals exist simultaneously. Generally they do not, except when the observation window overlaps both regions.

The frequency diversity between the vessel wall signal and the blood noise is illustrated by a simulation. The two spectra are displayed for different blood velocities with realistic parameters.

Simulation 4.1:

1) *Calculate the spectrum from a stationary vessel wall by Equation 2.42.*
2) *Assume the vessel wall is expanding. Shift the spectrum according to the Doppler equation for vessel wall (Equation 2.17) and plot.*
3) *For five blood velocities, calculate the blood spectrum broadening factor "k_{BSB}" (Equation 2.48). Scale the spectrum from stationary blood (Equation 2.42) in frequency and amplitude.*
4) *Shift these broadened spactra according to the Doppler equation for blood (Equation 2.16) and plot.*
5) *The following parameters are used:*

System frequency:	f_o=*20MHz.*
Transducer radius:	a=*0.68mm.*
Velocity of sound:	c=*1560 m/sec.*
Beam tilt angle:	ψ=*10degrees*
Depth of scatterers:	r_o=*5mm.*
Vessel wall velocity:	V_{VW}= *5 mm/sec.*

The expanding vessel wall gives a negative Doppler shift. The beam tilt angle is selected to also yield a negative Doppler shift in order to obtain a worst case situation regarding frequency diversity. The result of the simulation is shown in Figure 4.5. In (a) the frame rate is f_m=15 f.p.s., in (b) it is 7.5 f.p.s.

The following observations should be made:

1) The bandwidth of the vessel wall spectrum is proportional to the frame rate. The spectrum in Figure 4.5(a) is twice as broad as the spectrum in (b).
2) The Doppler shift from blood is independent of the frame rate.
3) The bandwidth from blood noise is not proportional to the frame rate. The *blood spectrum broadening factor* is a function of the frame rate, blood velocity and range.

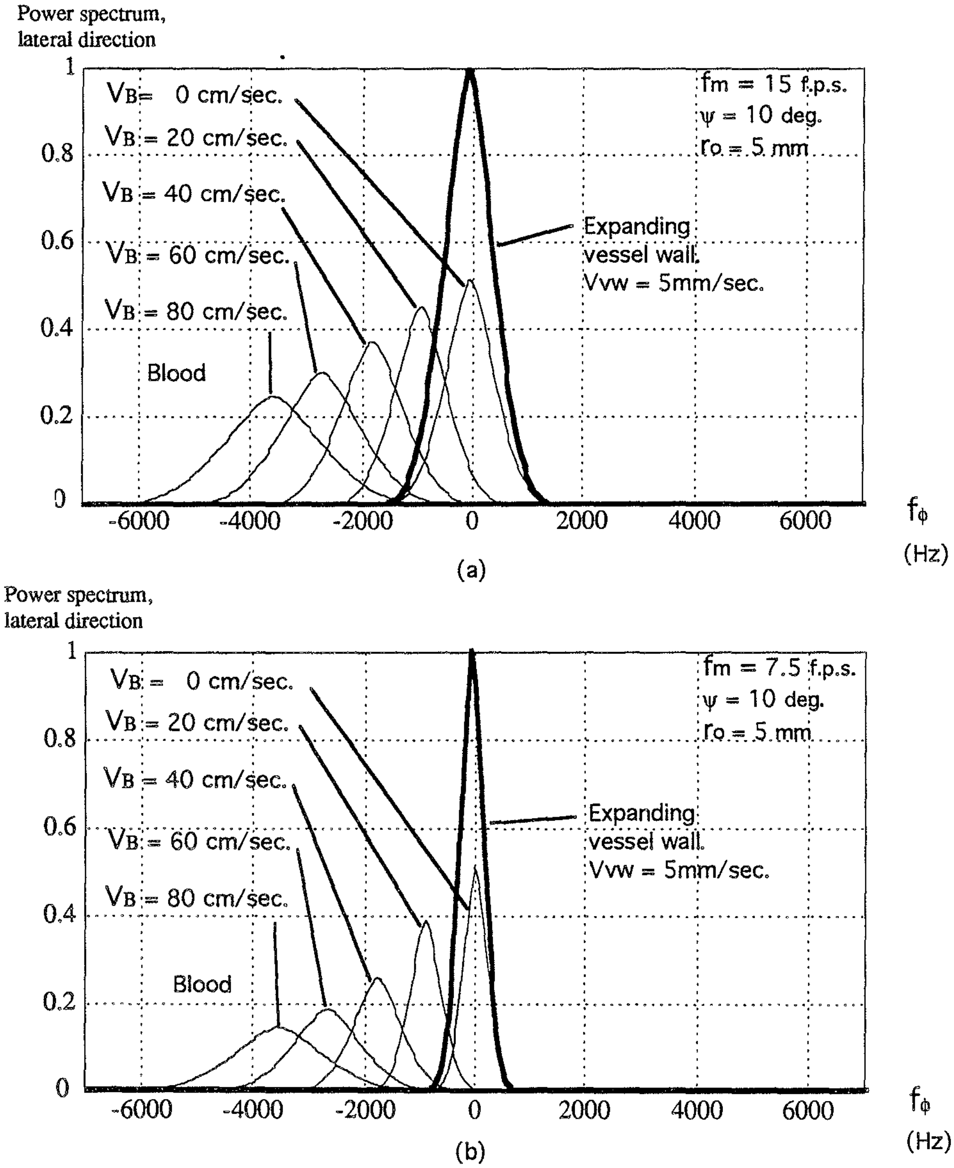

Figure 4.5 Realistic power spectrum in the lateral direction from expanding vessel wall and from blood. A worst case situation with respect to frequency diversity is shown where both Doppler shifts are negative.
(a) Frame rate: f_m = 15 f.p.s.
(b) Frame rate: f_m = 7.5 f.p.s.
The Doppler shifts are independent of the frame rate. The bandwidth of the vessel wall spectrum is proportional to the frame rate, while the spectrum from blood is not. The total effect is increased frequency diversity for decreasing frame rate.

By decreasing the frame rate, the frequency diversity increases, separation and/or detection becomes simpler. However, geometric distortion increases due to vessel wall and/or catheter movements.

Figure 4.5(a) illustrates that the power spectra from blood and vessel wall are fully separated for blood velocities exceeding 60 cm/sec. when the frame rate is 15 f.p.s. The number is 40 cm/sec. for frame rate equal to 7.5 f.p.s. This means that a low pass filter in the lateral direction will, according to the simulations, effectively reject blood noise for velocities exceeding these values.

However, the figure illustrates that the frequency diversity can be *detected* for lower blood velocities. A high-pass filter and a power estimate may for example register when the spectrum from blood is shifted slightly up or down.

This simulation indicates that beam tilting and lateral linear low-pass filtering will be effective for blood velocities exceeding ≈ 50 cm/sec. This limit can be pushed down by trading other parameters.

4.2.3 Blood noise detection

Assume that a power spectrum estimate "PSE_{Lat}" is calculated continuously, this based on a certain data window in the lateral direction. Then the measured frequency content will change as the beam scans through vessel wall and blood regions. In a vessel wall region, the spectrum will be approximately symmetric (the Doppler shift is low), and the bandwidth is defined by the beam properties and the frame rate. In a region with flowing blood, the spectrum will be asymmetric, and the signal power will appear outside the vessel wall spectral band. This difference can be detected. Two methods are suggested without further investigation:

1) Signal power outside the vessel wall spectral band can be detected by high-pass filtering the lateral signal and by estimating the power. Values exceeding a certain threshold are detected as blood signal, while values below the threshold are detected as vessel wall signal. This is illustrated in Figure 4.6(a) and (b). No power (except for noise) is measured in the pass-band of the high-pass filter in (a). In (b) the shaded area illustrates power P_0 from blood.

2) The asymmetry in the spectrum can be detected by integrating the power spectral density on both sides of a certain frequency limit. The ratio of integrated power "P_l" below the frequency limit "$f_{\phi c}$" to the integrated power "P_l" above the same limit is defined:

$$\beta = \frac{P_1}{P_2} \tag{4.1}$$

$$P_1 = \int_{-f_\phi s/2}^{f_\phi c} \mathrm{PSE}\{S(\phi)\} \qquad P_2 = \int_{f_\phi c}^{f_\phi s/2} \mathrm{PSE}\{S(\phi)\}) \tag{4.2}$$

A schematic illustration is given in Figure 4.6. In (c) a symmetric spectrum from a stationary vessel wall is presented, in (d) an asymmetric spectrum from blood. With the cutoff frequency as shown, "β" will be less than 1 for vessel wall signal and larger than 1 for blood signal. As the beam scans through regions with vessel wall and blood, "β" will change.

Whatever method is selected, the detection of vessel wall signal and blood noise can be formulated as a binary hypothesis test:

1) Given a vessel wall signal, what is the probability of detecting a vessel wall signal?
2) Given a blood signal, what is the probability of detecting blood?
3) Given a vessel wall signal, what is the probability of detecting blood?
4) Given a blood signal, what is the probability of detecting a vessel wall signal?

The first and second outcomes are correct, the other two represent false detection. In regions where blood noise is detected, a reject function can be applied. The probability of the two false detections should not be equal. It is better to accept some blood noise adjacent to a vessel wall region than to reject the vessel wall signal adjacent to a blood region. See the Neyman-Pearson test [Van Trees, 1986].

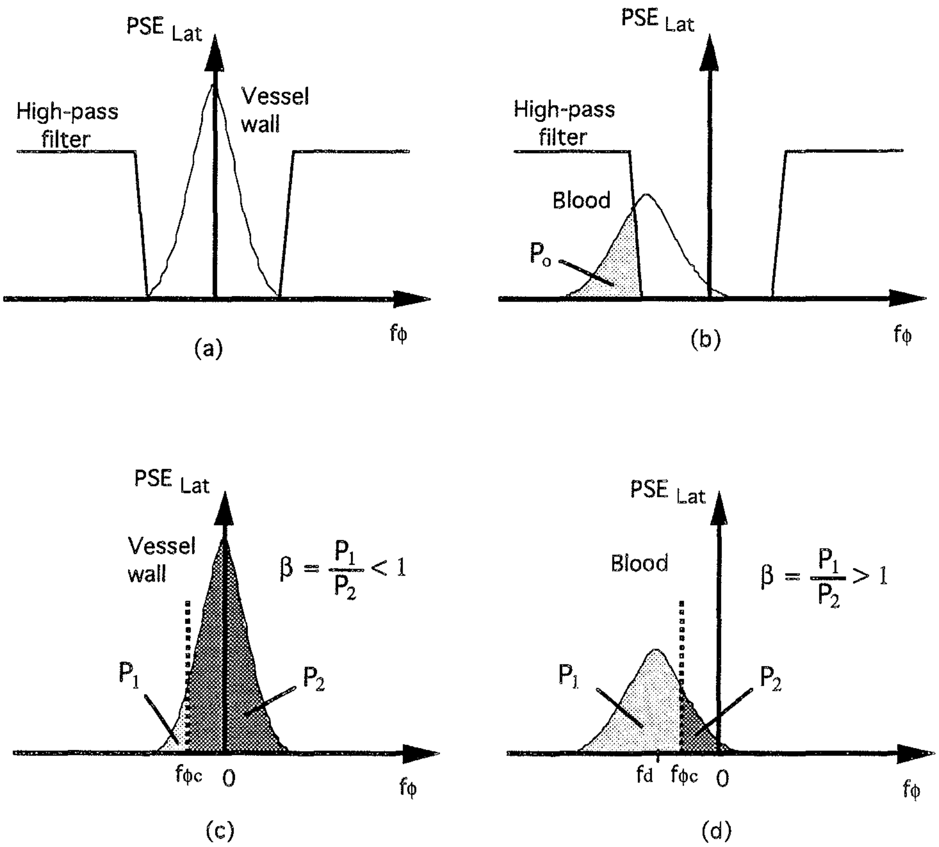

Figure 4.6 *Schematic illustration of two methods to detect signals from vessel wall and blood: in the upper panel by high pass filtering and power estimate, in the lower panel by detecting the spectrum asymmetry around a selected frequency limit "$f\phi c$".*
(a) Power spectrum from the vessel wall. No power except electronic noise is measured after high pass filtering.
(b) Power spectrum from blood, blood noise passes the high pass filter.
(c) The majority of the power from the vessel wall is located to the right of the frequency limit, i.e. $\beta < 1$.
(d) The majority of the power from blood is located to the left of the frequency limit, i.e. $\beta > 1$.

4.2.4 Blood noise filtering

This section describes blood noise reduction by lateral low pass filtering. The complex quadrature demodulated signal is supposed to be filtered in the lateral direction at each radial depth location. The filter is supposed to pass the vessel wall signal through with no or minimum distortion, while as much as possible of the blood noise should be rejected. In order for this method to be interesting in intravascular imaging, a real time implementation is required.

There are tradeoffs between filter performance and filter complexity. An *ideal low pass filter* covering the spectrum from the vessel wall will pass this signal through with no distortion. However, the blood noise power is not minimized. A Wiener filter can be considered which optimizes the signal to noise ratio for specified signal and noise (blood) spectra. The Wiener filter will distort the vessel wall signal slightly, but yield an optimal blood noise reduction for a certain blood velocity. Since the blood noise spectrum changes continuously, this is not a practical solution.

Filters: In this work two filters are considered. One is the averaging filter which is particularly simple to implement at high speed. However, the side lobe level in the frequency domain of this filter is higher than any other filter. The other filter is a 14th order FIR filter with lower side lobe level in the frequency domain and steeper pass-band edges. The noise bandwidth of the two is approximately equal. All tests were performed with both filters for comparison. The filters are denoted:

Filter 1: A 14th order FIR filter with cutoff frequency $k_c = 120$.
(Linear phase windowed design based on a
-20dB ripple Chebyshev window)

Filter 2: An averaging filter,
(N_{Ave}-1) order FIR-filter with equal coefficients.

The frequency response of these filters is compared with a typical spectrum from stationary scatterers in Figure 4.7, (Sephadex particles in water, log-amp included and beam density N_b=1024). *Filter1* is shown in (a). This filter is experimentally designed to obtain a better approximation to an ideal LP-filter than the simple averaging filter. *Filter2* is the simple averaging filter, identical to a FIR-filter with equal coefficients. The only parameter that can change filter spatial frequency response is the filter order. Increasing the filter order narrows the bandwidth. The frequency response for N_{Ave}=5 is shown in Figure 4.7(b). A slightly distorted signal is expected. In (c), 13 values are averaged yielding a narrower filter, significant distortion is expected.

No significant difference was observed between Filter1 and Filter2 with N_{Ave}=5 in any of the tests performed. For this reason, only the results based on Filter2 will be presented.

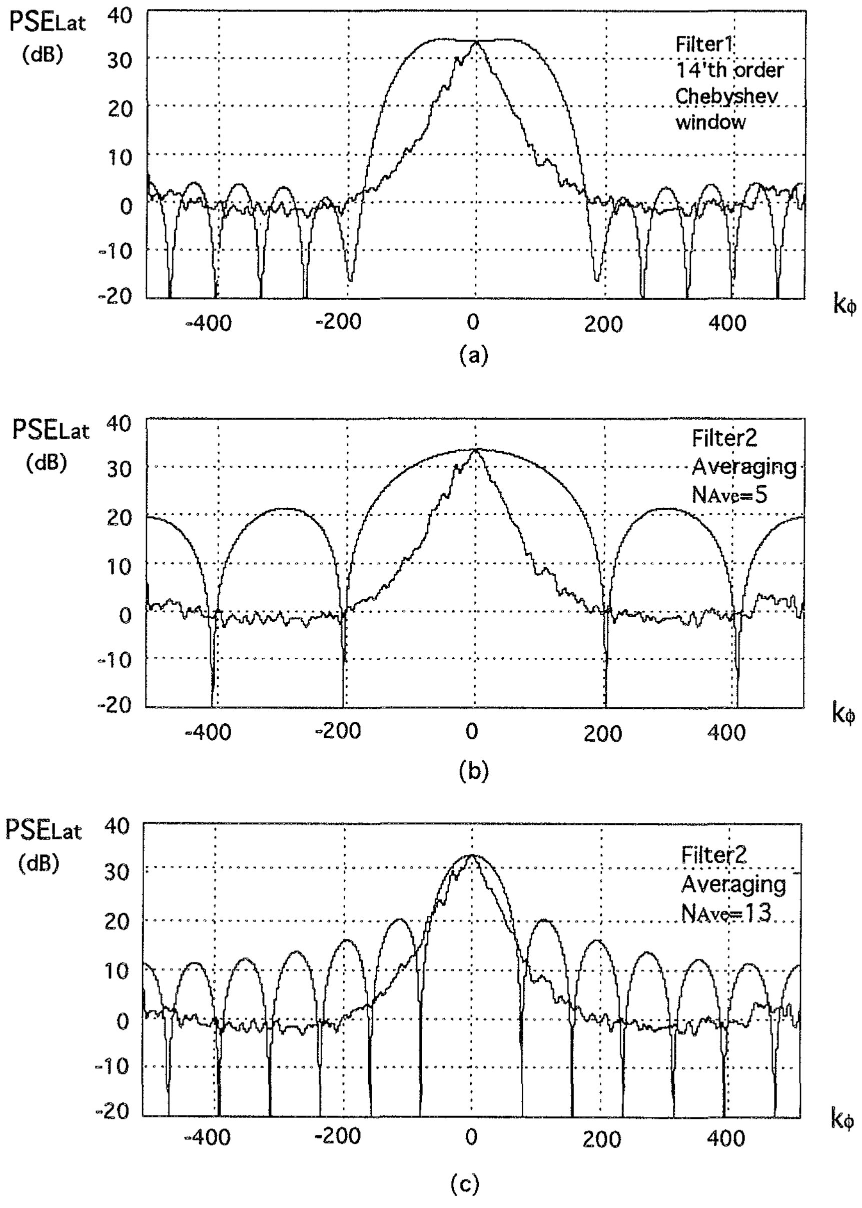

Figure 4.7 Comparison of the power spectrum in the lateral direction from stationary scatterers (log-compressed, Nb=1024) with the frequency response of the two actual filters:
(a) Filter1: 14th order FIR-filter (Chebyshev window)
(b) Filter2: averaging filter, N_{Ave}=5.
(c) Filter2: averaging filter, N_{Ave}=13.

Signal distortion versus filter order: Low distortion of the vessel wall signal should be given higher priority than effective blood noise reduction. The cutoff frequencies of the two filters were found empirically by narrowing the filter passband until a noticeable change in the image appeared. The frequency responses in Figure 4.7(a) and (b) represent the distortion limits for log-compressed signal from stationary scatterers. The following test was performed to find these limits:

> ***Test setup 4.1:*** *A silicone phantom was used as a tissue mimicking device. Small scatterers are mixed in a silicone mass and then cured (the recipe is unknown to the author). This material gives realistic tissue images. A flat surface of this material was kept close (≈3mm) to the mirror.*
> *An image was acquired with a flat 20 MHz transducer of radius $a=0.68mm$ and with the beam density $N_b=1024$ beams per revolution. The lateral spatial oversampling rate was $K_{\phi OS} = 1024/210 = 4.88$, (see Section 4.3.3). The raw data were transferred to the computer for filtering, magnitude detection, scan conversion and display. Decimation from 1024 to 256 beams was performed to match the display format.*

The result for Filter2 is shown in Figure 4.8. The unfiltered reference image is shown in (a). Figure 4.8(b),(c),(d) and (e) shows the result of averaging $N_{Ave} = 5$, 7, 9 and 13 adjacent complex samples respectively. There is a visible, but not significant change in the image when $N_{Ave} = 5$.

Low-pass filtering of the complex QD-signal in the lateral direction increase the speckle. The black regions due to destructive interference are broadened. The low-pass filter operation *appears at first glance* to be a contrast enhancement operation. Transitions from black to white get steeper. This is the opposite effect of what is observed when a gray level intensity image is low-pass filtered in the spatial domain. In the latter case, contrast and resolution is degraded, the image is smeared out.

The increased speckle effect can be explained by a phenomena described by Seggie [Seggie 1987]: *In areas of speckle, the instant frequency deviates significantly from the transducer center frequency.* In a spatial region with speckle, the quadrature demodulated samples will describe a large spread in phase values. By averaging several complex numbers with a large variation in phase, the result will go towards the origin, i.e. zero magnitude.

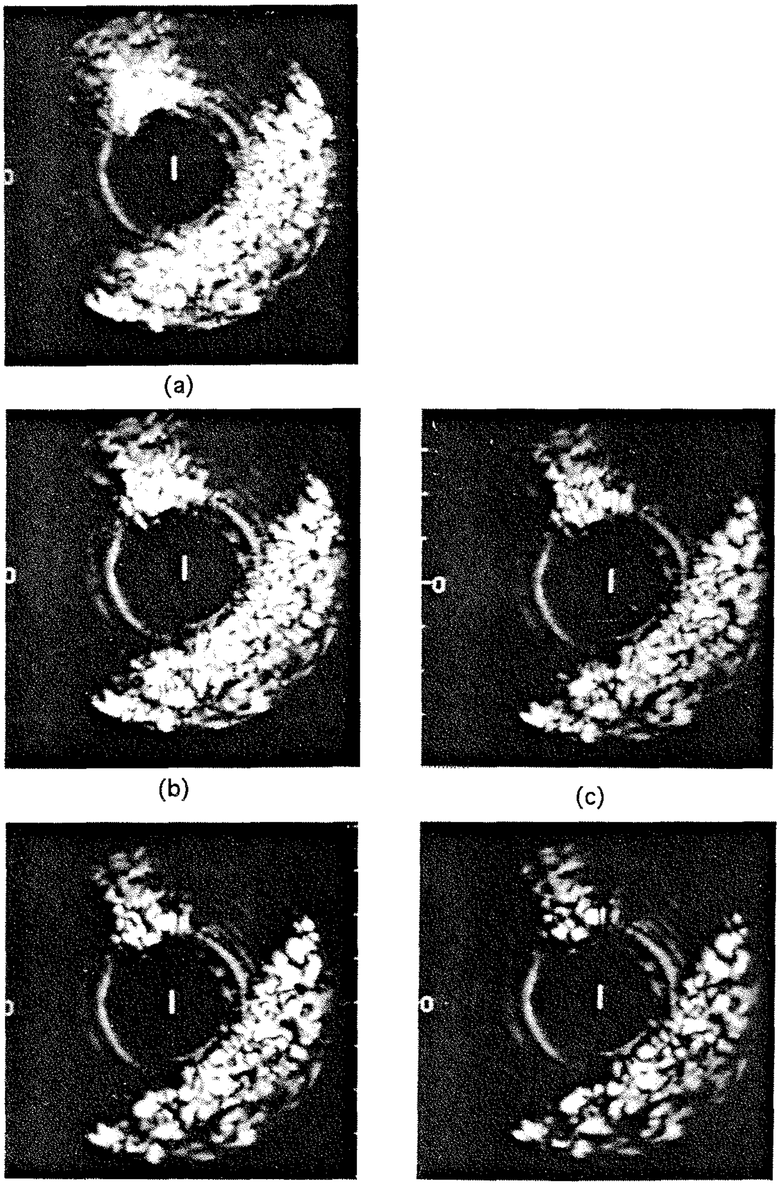

Figure 4.8 *Averaging the complex quadrature demodulated signal in the lateral direction by Filter2. A tissue mimicking phanthom is imaged with 4.88 times lateral oversampling. The image is slightly distorted for $N_{Ave}=5$. For higher N_{Ave} -values, the speckle pattern is enhanced.*
(a) No filtering, the reference image.
(b) $N_{Ave} = 5$ (4th order filter)
(c) $N_{Ave} = 7$. (d) $N_{Ave} = 9$. (e) $N_{Ave} = 13$.

4.2.5 Test results

In order to test the blood noise reduction by beam tilting and lateral low-pass filtering, two tests were performed:

1) *The static test:* Visualize the blood noise reduction versus flow velocity by flushing water with five different constant velocities through a circular tube. Sephadex particles were immersed in the water to mimic blood cells.

2) *The dynamic test:* Apply a realistic cardiac phasic velocity to the water flow in a tube and display 10 filtered images as a real time cineloop through the cardiac cycle.

1) The static test:

> ***Test setup 4.2:*** *A 20 MHz, 8F rotating mirror catheter (Cardiovascular Imaging Systems) was inserted into a 45 cm long rubber hose of inner diameter 5mm. The distal tip was located concentrically in the hose. The beam tilt angle was approximately 8 degrees. Water containing Sephadex particles was flushed through the hose from the proximal end of the catheter with a pump. The mean flow versus motor voltage was calibrated by time/collection measurements. The cross section of the hose and the catheter was measured, and the average water velocity at the scan plane was calculated. The raw data were transferred to the computer for filtering, magnitude detection, scan conversion and display.*
> *The beam density was N_b=1024, the frame rate f_m = 15 f.p.s. and the log-amp was used. Decimation from 1024 to 256 beams was performed after filtering.*

Results static test: The filtered (through Filter2), magnitude detected and scan converted images are shown in Figure 4.9. The bright circle in the periphery is the rubber hose. Water with Sephadex is located between the catheter and the hose. The strut artifact is located at between 11 to 12 o'clock in all images. A mirror leakage reverberation is located in the near field from 12 to 6 o'clock.

The image in Figure 4.9(f) is a reference image. It is not passed through the filter, just magnitude detected. The Sephadex noise is strong. Introducing the lateral low-pass filter reduces the noise even with zero velocity. The reason is electronic noise reduction due to lateral oversampling and averaging. This zero velocity image is shown in Figure 4.9(a). In (b) the water velocity is 20 cm/sec. The Sephadex noise is slightly reduced. In (c), (d), and (e) the water velocity is 40, 50 and 80 cm/sec. respectively.

> **The noise rejection increases with water velocity, but it is effective only for velocities ≥ 50 cm/sec. This corresponds to the observation made in Section 4.2.2.**

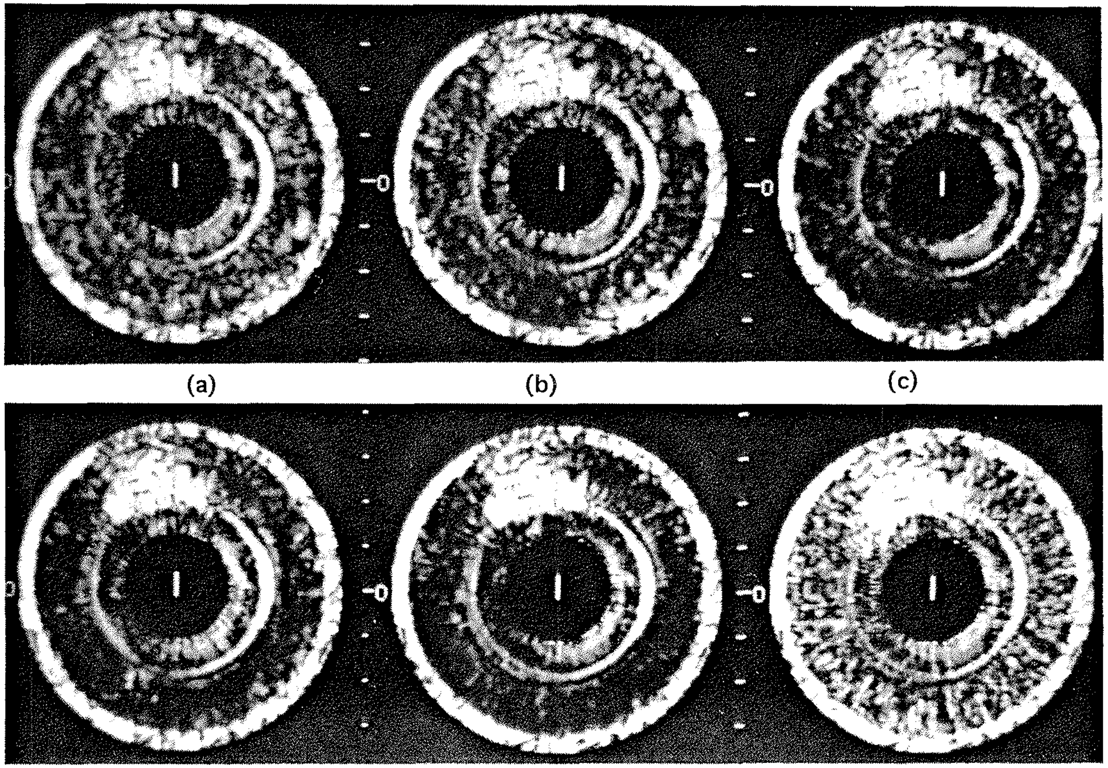

(a) (b) (c)

(d) (e) (f)

Figure 4.9 The static test: Reduction of blood noise versus blood velocity by lateral low pass filtering.
Filter2 (N=5) is applied in the lateral direction.
A 20 MHz catheter (8F) is located concentrically in a 5mm diameter rubber hose (bright ring). Water with immersed Sephadex particles mimics blood. Constant flow velocity "VB" is obtained with a pump.
(a) VB = 0 cm/sec. (d) VB = 50 cm/sec.
(b) VB = 20 cm/sec. (e) VB = 80 cm/sec.
(c) VB = 40 cm/sec. (f) Magnitude detected reference image.

2) The dynamic test:

A more realistic experiment was performed by introducing the catheter in the cardiovascular hydromechanical model described in Section 3.1.7. The purpose of this experiment was to do imaging with a realistic flow curve and observe the performance in an approximate real time situation.

Test setup 4.3: *A 20 MHz, 8F rotating mirror catheter (Cardiovascular Imaging Systems) was introduced into the vascular model in a rubber "vessel" with diameter 8mm . The flow was directed towards the catheter tip in order for the catheter not to affect the flow profile except around the distal tip.*

The flow velocity was monitored by a 7.5 MHz pulsed Doppler system, CFM750 (Vingmed Sound, Horten, Norway). The sample volume was located less that 1 cm from the catheter tip, and the location within the vessel was adjusted to obtain maximum velocity. The cardiac model parameters were adjusted to obtain a realistic phasic velocity curve for a coronary artery (primarily diastolic flow) and for a peripheral artery (short systolic peak flow). However, the peak velocities were set somewhat higher than realistic. The model was filled with water. To mimic red blood cells, 20 ml water with Sephadex particles was injected into the ventricle a few seconds prior to the data acquisition.

In order to reduce electromagnetic interference from the instrument and other services, the transducer leads were cut at the distal tip of the catheter, and new short (≈20cm) leads were connected directly to the pre-amp.

Ten images were acquired with beam density N_b = 1024 and transferred to the computer. In the computer, the ten images were filtered laterally, decimated from 1024 to 256 beams/rev., magnitude detected and scan converted. The resulting ten images were stored in the memory.

Parameters summarized:

Beam tilt angle:	$\psi = 8$ *deg.*
System frequency:	$f_o = 20$ *MHz,*
Circular transducer, radius:	$a = 0.72mm$
Frame rate:	$f_m = 20$ *f.p.s.*
Lateral sampling frequency:	$f_{\phi s} = 20kHz$
Water velocity:	$V_B = 0\text{-}90$ *cm/sec.*
Lateral oversampling:	$K_{\phi OS} = 4.41$
Filter2 (order + 1):	$N_{Ave} = 5$

Results dynamic test: The filtered images were displayed in a real time cineloop by the "EchoLoops" program (Vingmed Sound). For comparison, the same 10 images without filtering were displayed simultaneously. This test demonstrated the same that was found in the static test: blood noise is effectively reduced for velocities exceeding ≈50cm/sec. With the peripheral phasic velocity, the blood noise was rejected a short fraction of the cardiac cycle. With the coronary phasic velocity, the noise reduction was effective over a larger fraction of the cardiac cycle. In both cases, the blood noise was blinking.

4.2.6 Summary, discussion and conclusion

Summary: Many parameters affect the frequency diversity of blood and vessel wall signal, the most important ones can be summarized as follows:

Beam tilt angle: The Doppler shift from blood is approximately proportional to the tilt angle for relevant angles. This parameter has no significant influence on the bandwidth.
A minor side effect is geometric distortion.

System frequency: The Doppler shift is proportional to the system frequency. If the system frequency is increased without affecting the beam profile (by reducing the transducer diameter) the separation increases proportionally.
The undesirable side effect is increased back-scattered power from blood ($P_s \sim f^4$). For velocities where the frequency diversity is high, the low-pass filter rejects most of the blood noise. At zero or low velocities where the filter is not effective, the situation has become worse.

Transducer size: Reducing the transducer size while the system frequency is kept constant will broaden the beam and reduce the lateral bandwidth from tissue and blood. The separation process becomes easier.
The major undesirable side effect is reduced resolution.

Frame rate: Decreasing the frame rate reduces the vessel wall temporal bandwidth proportionally. The temporal bandwidth from blood is not decreased proportionally due to the *blood spectrum broadening factor* (k_{BSB}). The Doppler shift from blood is not affected. The net effect is increased frequency diversity and an improved result.
The undesirable side effect is geometric distortion due to vessel wall and/or catheter movements.

Blood velocity: The Doppler shift is proportional to the blood velocity. Unfortunately, the bandwidth does also increase due to reduced transit time. The blood velocity is not under control by the user except for the artificial occlusion caused by the catheter.

Discussion: With the parameters as described in the experiment, the blood noise rejection algorithm is not cost effective to implement. The question is whether it can be made cost effective by changing all or some of the parameters affecting the frequency diversity. There is a large amount of tradeoff situations, and if we are willing to sacrifice other image quality parameters, a more effective blood suppression may be obtained, for example:

Increase the beam tilt angle from 8 to 12 degrees and the system frequency from 20 to 35 MHz. The Doppler shift from blood increases with a factor 2.6. This means that a blood velocity of ≈20 cm/sec will cause the same Doppler shift as 50 cm/sec in the previous test. Reducing the frame rate will make the blood noise rejection even more effective.

Blood noise reduction by beam tilting and lateral low-pass filtering causes the blood noise to blink. The contrast between the vessel wall and the lumen is improved in a short fraction of the cardiac cycle and the vessel wall is enhanced. But the blinking effect may be distracting to the user, the blood noise "calls attention".

In contrast, with no blood noise filtering, the lumen appears as a continuously changing noise pattern while the vessel wall signal is more stationary. This difference helps in discriminating the vessel wall from the lumen. It is questionable what the ultrasound users will prefer.

Conclusion: Reduction of blood noise by beam tilting and lateral low pass filtering is effective for blood velocities exceeding ≈50 cm/sec. with the parameters described in this section. This means that the noise will blink. Blood noise reduction can be traded against other image quality parameters.

The *averaging filter* (Filter2) is found to perform approximately equal to the 14th order FIR-filter (Filter1). The averaging filter is selected due to its simple implementation form and high speed.

4.3 Electronic noise reduction by lateral LP-filtering

Uncorrelated noise is effectively reduced by low-pass filtering in the lateral direction. To avoid distortion of the desired signal, lateral oversampling is required. This method is effective if the transmitted power per pulse is kept constant, i.e. the average transmitted power is allowed to increase by lateral oversampling. However, if the average power cannot be increased, no effect will be obtained. Constant power per pulse is assumed here.

The method is most efficient for noise that is completely uncorrelated in the lateral direction, i.e. amplifier and sensor noise which will be denoted *uncorrelated electronic noise. Electromagnetic interference* is uncorrelated or partially correlated. *Tissue reverberations* (due to the "diamond" effect) may be partially correlated, however, this is not verified. The performance of the noise reduction method described in this section is only specified for *uncorrelated electronic noise*.

4.3.1 Minimum beam density

To be able to extract all information in the vessel wall signal, the lateral spatial sampling frequency should be at least twice the maximum frequency component present in the signal. According to Equation 2.28, the lateral spatial sampling frequency equals the beam density. This puts the following restriction on the beam density:

$$N_b = k_{\phi s} \geq 2\, k_{\phi Max} \tag{4.3}$$

The maximum spatial frequency content in the stationary vessel wall signal is given by Equation 2.43. To avoid aliasing, the lower limit to the beam dencity is:

$$N_{bMin} = 2\, k_{\phi Max} = 4\, k_o\, a \tag{4.4}$$

> ***Example 4.1*** *For a flat circular 20 MHz transducer with radius a=0.68mm, the minimum required beam density is (c=1560 m/sec):* $\boldsymbol{N_{bMin} = 4\, k_o\, a = 219}$
> *These parameters are realistic for the system used in this work. The default beam density of the system is* $N_b = 256$ *which means that the system is slightly oversampled for a linear frontend. With the log-amp present, the maximum lateral frequency component in the stationary vessel wall signal is higher (up to two times higher) which means that aliasing occurs for the default beam density.*

The *lower* limit of the beam density for a circular transducer is set to $N_{bMin} = 4k_o\, a$ in order to avoid aliasing.

4.3.2 Maximum beam density

For a fixed frame rate, the beam density can be increased until the echo from pulse "n-1" almost interfere with the echo from pulse "n". This puts the following restriction to the beam density:

$$N_b \le \frac{PRF_{max}}{f_m} \tag{4.5}$$

where the PRF_{max} is the maximum *pulse repetition frequency* that does not cause interference between pulses. PRF_{max} is determined by the transmit power, the transducer insertion loss, the attenuation and the electronic noise level. This value can be *calculated* based on measured transducer and instrument parameters and measured or tabulated attenuation coefficients. However, in this work the upper PRF-limit is determined empirically by defining a maximum Penetration Depth (PD) based on experience with practical imaging. The maximum PRF is related to the penetration depth by:

$$PRF_{max} = \frac{c}{2\,PD} \tag{4.6}$$

Experience with the "Insight" instrument from Cardiovascular Imaging Systems indicates the following practical limits: At 20 MHz the penetration depth is approximately 10mm and at 30 MHz it is approximately 4.5mm. A safe upper limit to the PRF is defined by doubling these penetration depths, see Table 4.1.

The maximum beam density is then:

$$N_{bMax} = \frac{PRF_{max}}{f_m} \tag{4.7}$$

Table 4.1 *Empirically evaluated penetration limits determine the maximum pulse repetition frequencies.*

f_o	PL	$\mathbf{PRF_{max}}$
20 MHz	20 mm	**39 kHz**
30 MHz	9 mm	**86 kHz**

4.3.3 Lateral oversampling, maximum noise reduction

Lateral oversampling: In the previous two sections, a lower and an upper limit to the beam density was found:

$$N_{bMin} \le N_b \le N_{bMax} \tag{4.8}$$

When "N_b" exceeds the lower limit, the signal is *oversampled*. This can be expressed in the frequency domain by the ratio of the *actual* spatial sampling frequency to the *minimum* required spatial sampling frequency in the lateral direction. The *lateral spatial oversampling ratio* is defined:

$$k_{\phi OS} = \frac{k_{\phi s}}{2\, k_{\phi Max}} \tag{4.9}$$

By inserting Equations 2.28 and 4.4 into this equation, the result is:

$$k_{\phi OS} = \frac{N_b}{N_{bMin}} \tag{4.10}$$

Noise reduction: Noise reduction due to oversampling and low-pass filtering is conveniently described by an ideal low-pass filter covering the spectrum from the vessel wall. The Noise Equivalent Bandwidth (NEB) of the ideal low-pass filter equals the filter bandwidth. If the sampling frequency is increased while the signal and noise power is kept constant, the fraction of the noise that passes the filter will decrease proportionally. The maximum possible *noise reduction factor* "P_{nRej}" is given by the ratio of the sampling frequency "$k_{\phi S}$" to twice the noise equivalent bandwidth of the filter (2NEB). This ratio equals the lateral spatial oversampling ratio:

$$P_{nRej} = 10\log\left(\frac{k_{\phi S}}{2\,NEB}\right) = 10\log(k_{\phi OS}) = 10\log\left(\frac{N_{bMax}}{N_{bMin}}\right) = 10\log\left(\frac{PRF_{Max}}{N_{bMin}\ f_m}\right) \tag{4.11}$$

This relation is illustrated in Figure 4.10 where Equations 4.7 and 4.10 are plotted and connected.

In the first quadrant, "N_{bMax}" is plotted versus the frame rate "f_m" for 20 and 30 MHz system frequency. Operating above these lines, there is a risk that the echo from the previous pulse will interfere with the signal from the current pulse. The area below these lines indicates possible tradeoffs between frame rates and beam densities. In order to avoid geometric distortion due to vessel wall or catheter movements, the frame rate should be selected from the right half of the allowed area. In order to avoid aliasing from the blood signal, the PRF should be high, i.e. the beam density should be selected from the upper part of the allowed area.

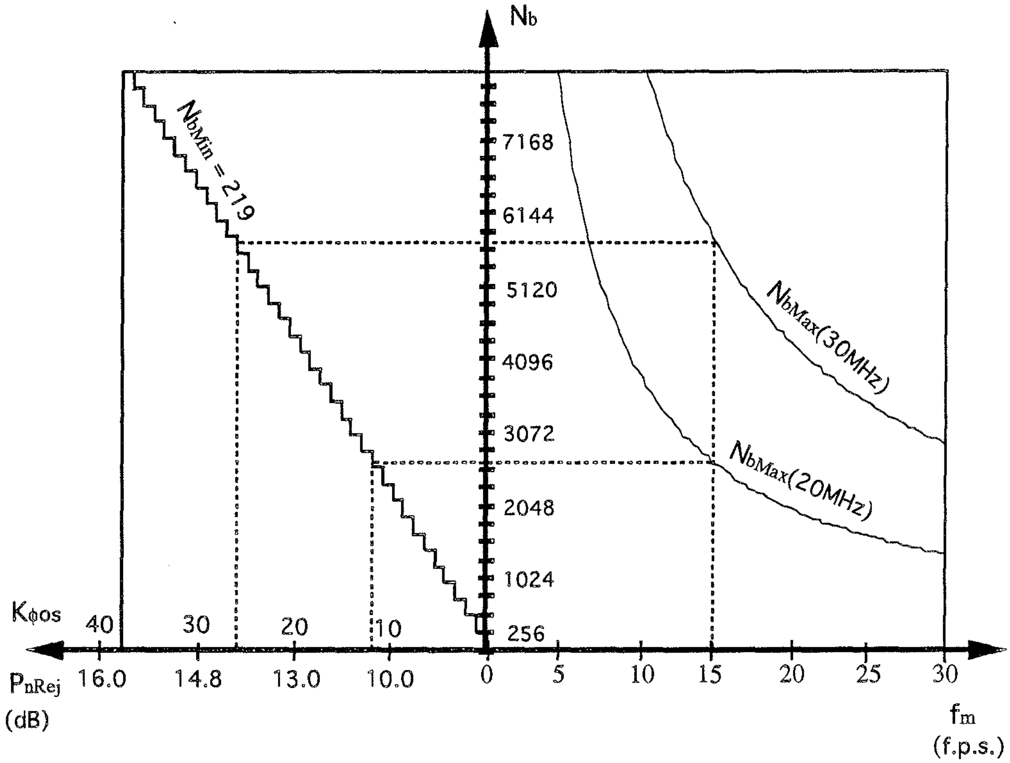

Figure 4.10 ***First quadrant:*** *Maximum beam density "N_b" without aliasing versus the frame rate "f_m" for 20 and 30 MHz system frequency.*
Second quadrant: *The lateral oversampling ratio "$k_{\phi OS}$" versus the minimum beam density "N_b" (the aliasing limit).*
The corresponding maximum noise rejection factor "P_{nRej}" in dB is shown below.

The lateral spatial oversampling ratio "$k_{\phi OS}$" is plotted versus the minimum beam density in the second quadrant. A realistic value for the minimum beam density (valid for the measurements in this work) is used: N_{bMin} = 219.

Example 4.2: *At the default frame rate f_m = 15 f.p.s., (N_{bMin} = 219) and at 20 MHz system frequency, the maximum lateral oversampling rate is $k_{\phi OS}$ = 11.8. This corresponds to a maximum possible noise rejection ratio P_{nRej} = 10.7 dB. At 30 MHz, the same values are 26.2 and 14.2 dB respectively.*

By lateral oversampling and ideal low-pass filtering, it is possible to obtain electronic noise power rejection ratios in the range ≈7 to ≈15 dB.

The increased penetration depth due to lateral oversampling and ideal low pass filtering is demonstrated in the following example. We assume that electronic noise is the only noise that limits the penetration. As a rule of thumb, the one way attenuation in tissue is 1dB/cm/MHz.

> ***Example 4.3:*** *With the same parameters as in Example 4.2, the penetration depth will increase from ≈10mm to ≈12.7mm at 20 MHz and from ≈4.5mm to ≈6.9mm at 30 MHz. This represents a 27% increase in penetration at 20 MHz and 53% increase at 30 MHz.*

4.3.4 Lateral averaging, test results

The ideal low pass filter represent maximum noise reduction with no vessel wall signal distortion. The Wiener filter optimizes the signal to noise ratio, i.e. accepts a minor vessel wall distortion. Since uncorrelated noise has constant power spectral density, the Wiener filter is a good choice with respect to signal to noise performance. However, the processing requirements of the Wiener filter are not investigated. Based on the results from section 4.2, only the *averaging filter* will be considered.

Averaging filter: The averaging filter has a *noise equivalent bandwidth* equal to $1/N_{Ave}$ where N_{Ave} is the number of samples averaged. This means that this filter performs equal to the ideal low-pass filter with respect to noise reduction. The frequency response of the averaging filter deviates from the ideal low pass filter frequency response, but this was found to have a minor effect on the image.

The number of adjacent samples to average can be expressed by the integer part of the lateral spatial oversampling factor:

$$N_{Ave} = \mathrm{INT}\{K_{\phi OS}\} = \mathrm{INT}\{\frac{N_b}{N_{bMin}}\} \qquad (4.12)$$

The effect of lateral oversampling and averaging to reduce electronic noise is demonstrated by the following test:

> ***Test setup 4.4:*** *A 20 MHz catheter was located in water and the gain was turned up to make electronic noise visible (log-compressed electronic noise). The beam density "N_b" was set to 1024 (4.7 times lateral oversampling). The data were transferred to the computer, filtered by the averaging filter, magnitude detected, scan converted and displayed.*

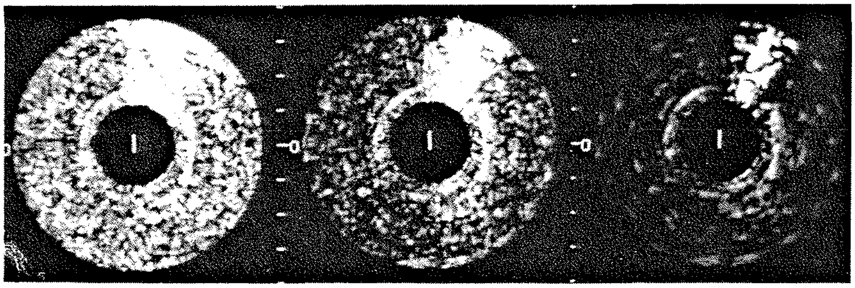

(a) (b) (c)

Figure 4.11 *Illustration of electronic noise rejection by lateral averaging. A catheter was located in water and the gain turned up to make electronic noise visible (with log-amp).*
(a) Magnitude detected reference image.
(b) N=5 values averaged.
(c) N=13 values averaged.

The result is shown in Figure 4.11. The original noisy image (no filtering) is shown in (a). A significant noise reduction is observed in (b) where N=5 adjacent values are averaged. The image in (c) is filtered with N=13, almost all electronic noise is canceled (however, the latter filter would distort the vessel wall signal).

4.3.5 Conclusion

Lateral oversampling and low-pass filtering to reduce uncorrelated (primarily electronic) noise is a powerful method to increase the signal to noise ratio and thereby increase the penetration limit. Noise power rejection factors in the range ≈7dB to ≈15dB are realistic. This represents a significant improvement.

The averaging filter is an effective electronic noise reduction filter. Its application leads to a minor vessel wall distortion.

A realistic value for the noise figure of the pre-amp is 3 dB. If this limit is reached, very little is gained by further improving the noise figure. Noise reduction by lateral oversampling and averaging is a more cost effective solution.

In addition to rejecting electronic noise, this filter also rejects blood noise that is located outside the pass band of the filter as described in Section 4.2.

The simple form of the *averaging filter* and the fact that this filter serves two noise rejection purposes simultaneously, makes lateral oversampling and averaging a cost effective solution.

4.4 Catheter reverberations, lateral detection and canceling

This section describes a method of detecting and canceling catheter reverberations characterized by constant phase, i.e. *mirror leakage reverberations* and *protecting tube reverberations*. These two reverberation types are denoted *constant phase catheter reverberations*.

In beam to beam mode, these reverberations represent a narrow band low-pass signal, typical bandwidth is less than 10% of the bandwidth from the stationary vessel wall. A lateral high-pass filter may be implemented in each depth location to suppress the reverberations. An attempt was made to design a high-pass FIR-filter with a cutoff frequency about 10% of "$k_{\phi Max}$", the maximum spatial frequency content from stationary vessel wall. Due to the very steep transition band requirement of the filter frequency responce, a filter order in the range 100 was necessary. This method was rejected due to difficulties in the implementation.

4.4.1 Reverberation signal characteristics

The reverberation reduction method described in this section is based on signal characteristics extracted from realistic measurements. Such reverberations may appear in the lumen with no other noise signals. They may also appear in combination with electronic noise, blood noise and/or vessel wall signal. The data acquired in this work include reverberations in combination with electronic noise and vessel wall signal, no blood noise is considered. The following test describes the data collection:

> ***Test setup 4.5:*** *A 20 MHz rotating mirror catheter (8F, Cardiovascular Imaging Systems) was located in water. The catheter exhibited* ***mirror leakage reverberations.*** *Data were sampled with beam density N_b=512 to avoid aliasing since the log-amp was used (see Example 4.1 in Section 4.3.1). Several images were acquired with different signal combinations: low noise level, high noise level, with and without the tissue mimicking phantom.*

Signals from different regions of the images were characterized in the computer. The following description summarizes the main results:

Electronic noise only: Electronic noise is characterized by a circular Gaussian process at the output of the quadrature demodulator when a linear frontend is used. With the log-amp present, the probability density distribution changes, but the complex signal will still describe a "noise cloud" centered at origin. The complex mean-value is located at the origin, and the fluctuations around this point increases with the noise power.

A lateral sequence of electronic noise samples is plotted in Figure 4.12(a), adjacent values are connected with straight lines in the complex plane.

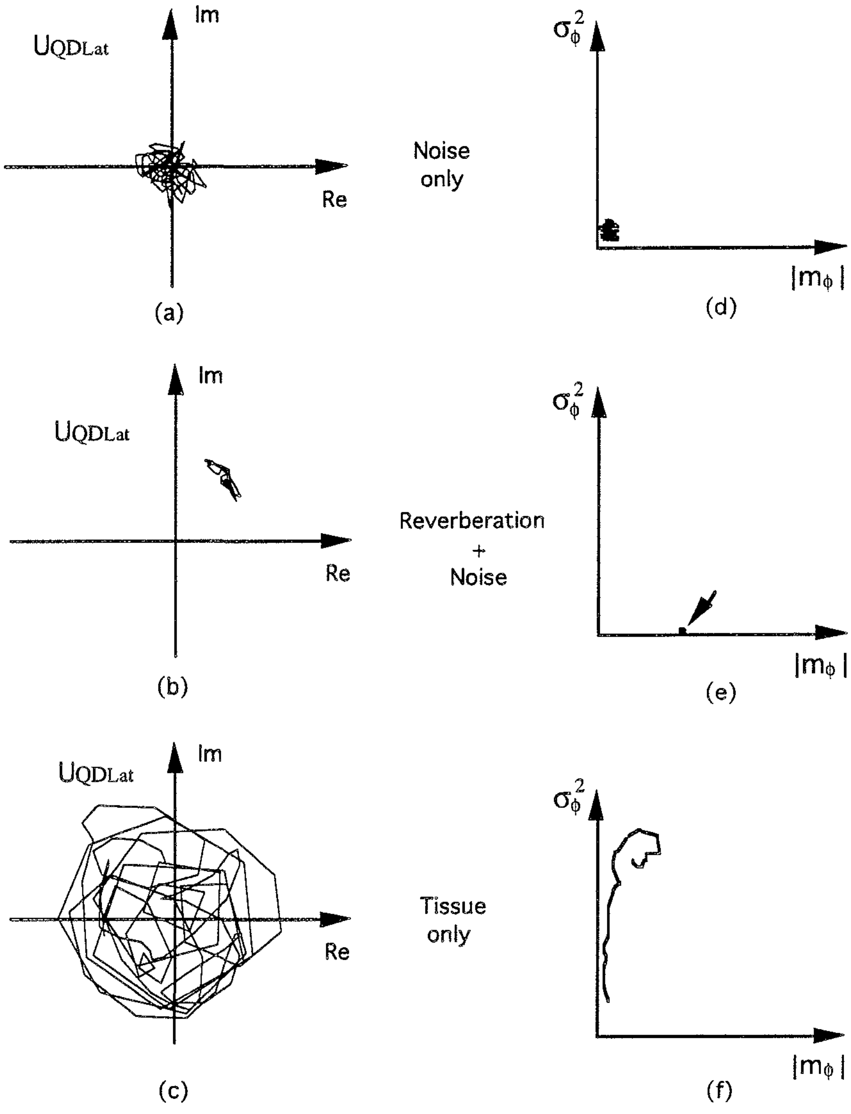

Figure 4.12 *__Left:__ Lateral sequences from acquired data are displayed by projecting all samples down in the complex plane. Mirror leakage reveberations are from a rotating mirror catheter in water, and tissue signals are from a tissue mimicking phantom. All measurements are performed with the log-amp.*
(a) Electronic noise only. (b) Reverberation plus electronic noise.
(c) Tissue mimicking phantom.
__Right:__ "Magnitude of lateral mean-value estimate" $|m_\phi|$ and "lateral variance estimate" σ_ϕ^2 of the same sequences are plotted to illustrate tha
(d) Electronic noise yields low mean-value magnitude and low variance.
(e) Reverberation plus noise yields high mean-value magnitude and low variance.
(f) Tissue signal yields low mean-value magnitude and high variance.

Constant phase reverberations only: If the signal *strength* from a phase reverberation is constant as well as the phase, all the complex samples will be located at a *single point* in the complex plane. The complex mean-value will be located in the complex plane outside the origin. The distance from the origin increases with the signal strength, and the phase is given by the phase difference between the received RF-signal and the local oscillator in the quadrature demodulator, i.e. by the distance between the transducer and the reflector. There are no fluctuations around the complex mean-value.

Reverberations plus noise: When electronic noise is added to a *constant phase & constant strength reverberation*, the complex signal will describe a noise cloud centered at the point given by the complex mean-value of the reverberation (assume linear frontend).

The situation changes when the log-amp is included. The effect of the log-amp on the sum of noise and a strong signal is described in Section 2.4.5. Increasing the *reverberation* signal strength causes the *noise* power at the output of the log-amp to *decrease*. A data sequence of a reverberation signal plus noise is plotted in the complex plane, see Figure 4.12(b) (the input noise level is the same as in Figure 4.12(a)). The fluctuations around the complex mean-value are reduced.

Tissue only: The signal from the vessel wall is normally much stronger than the electronic noise. The vessel wall signal exhibits large fluctuations around the complex mean-value which is located at the origin. This is illustrated in Figure 4.12(c).

Tissue and reverberation: When a reverberation signal is added to a tissue signal, the complex mean-value is shifted out to a certain position given by the reverberation mean-value. However, it is difficult to detect this change in mean-value due to high variance in the estimate. The reason for this is limited observation length and limited spatial bandwidth of the system.

From this signal characterization, the following conclusions can be made:

1) Electronic noise is characterized by a complex mean-value located at the origin and low to medium fluctuation or variance around this point.
2) Constant phase catheter reverberations are characterized by a complex mean value located off center in the complex plane and with no fluctuations, zero variance.
3) Adding noise to a constant phase catheter reverberation causes the variance to increase slightly.
4) Tissue signal is characterized by a complex mean-value located at the origin and medium or large variance.

4.4.2 Reverberation detection

The signal characteristics found in the previous section indicates that a *lateral mean-value estimator* (m_ϕ) and a *lateral variance estimator* (σ_ϕ^2) will yield valuable information for the purpose of reverberation detection. The former is defined by simply averaging "K_{Ave}" (a odd number) quadrature demodulated samples in the lateral direction:

$$m_\phi(r,\phi) = \frac{1}{K_{Ave}} \sum_{n=-x}^{x} QD(r,\phi+n) \qquad x = \frac{K_{Ave}-1}{2} \qquad (4.13)$$

The magnitude of this estimate describes the distance in the complex plane from the origin to the lateral mean-value estimate.

The fluctuations around the estimated mean value is described by the *lateral variance estimate*:

$$\sigma_\phi^2(r,\phi) = \frac{1}{K_{Ave}} \sum_{n=-x}^{x} \left| QD(r,\phi+n) - m_\phi(r,\phi) \right|^2 \qquad x = \frac{K_{Ave}-1}{2} \qquad (4.14)$$

The two estimators: "$|m_\phi(r,\phi)|$" and "$\sigma_\phi^2(r,\phi)$" were applied to the data sequences presented in Figure 4.12(a),(b) and (c). The result is shown in (d),(e) and (f) respectively. In these calculations, the number of averaged samples was: $K_{Ave} = 35$. Electronic noise is represented with a low mean-value magnitude and low or medium variance. Constant phase catheter reverberations are represented by low, medium or high mean-value magnitude and low variance. Tissue signal is represented with a low mean-value magnitude and medium or high variance.

The two estimators can be combined in a mathematical function or a lookup table that outputs a *Reverberation Detector* (RD), a value between zero and one. Values close to one represent *constant phase catheter reverberations* in the presence or absence of electronic noise. Values close to zero represent everything else, i.e. vessel wall and/or other noise signals.

One possible realization of the lookup table is illustrated schematically in Figure 4.13. This function is not an optimal function based on statistical analysis, it is rather an intuitive suggestion based on the observations made in Figure 4.12.

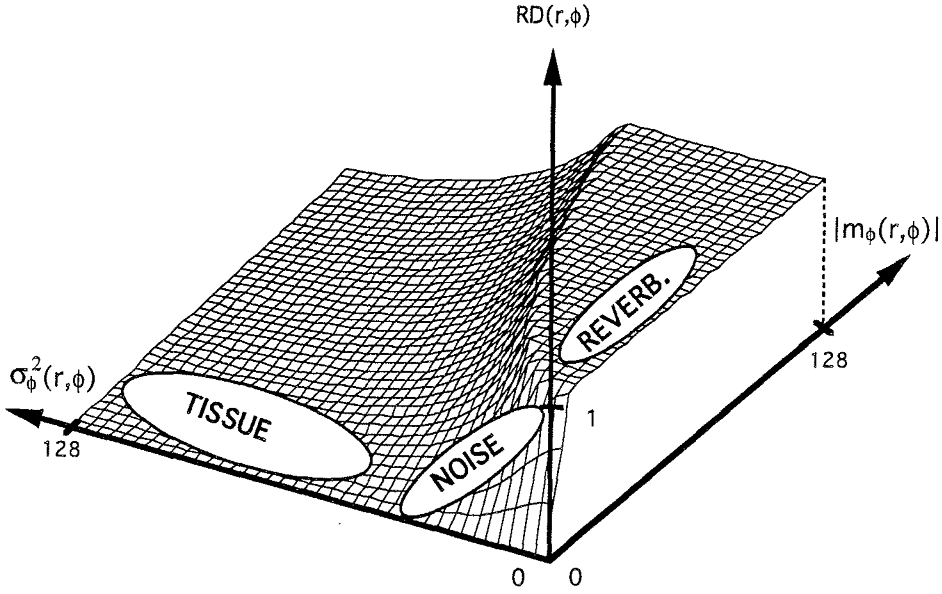

Figure 4.13 *One possible realization of the lookup table that combines the magnitude of the* ***lateral mean-value estimate*** *$|m_\phi(r,\phi)|$ and the* ***lateral variance estimate*** *$\sigma_\phi^2(r,\phi)$ to a* ***Reverberation Detector*** *RD(r,ϕ). Electronic noise is characterized by a low mean-value magnitude and low or medium variance. Constant phase catheter reverberations are characterized by a low, medium or high mean-value magnitude and low variance. Tissue signal is characterized by a low mean-value magnitude and medium or high variance.*

4.4.3 Reverberation canceling

A reverberation detector is found in all locations of the ultrasound image. The RD(r,ϕ) value represents the probability that a sample belongs to a reverberation region. There are several ways to *cancel* reverberations from the display when RD(r,ϕ) is given:

One way is to turn the display off (black) in areas where RD(r,ϕ) exceeds a certain threshold. This is a drastic way or rejecting reverberation. The error will be large when the algorithm fails.

Another method is to multiply the original magnitude detected image with [1-RD(r,ϕ)], a value that is close to zero in reverberation regions and close to one in other regions. This is a softer way of reducing reverberations. This will still have a dramatic consequence when the estimator fails. Bright regions in the original image may be displayed black.

A third and better method is to subtract the *lateral mean-value estimate* "$m_\phi(r,\phi)$" from the original image in regions where $RD(r,\phi)$ exceeds a certain threshold. When this estimator fails, the error will be much smaller. This method was implemented and tested, but appeared to have one visible drawback: The "tails" of the reverberations were not canceled. It took a few samples before the threshold was exceeded, and then the reverberation was cut abruptly.

A fourth and even better method is combine the second and third methods: Reverberations are rejected by subtracting the *lateral mean-value estimate* "$m_\phi(r,\phi)$" from the original signal in regions with reverberations. However, before "$m_\phi(r,\phi)$" is subtracted, it is scaled with the reverberation detector $RD(r,\phi)$. This product is denoted: Reverberation Mean Estimate (RevMeanEst). This means that in regions where $RD(r,\phi)=0$, no mean-value estimate is subtracted, the signal is passed straight through. In regions where $RD(r,\phi)=1$, the mean-value estimate is subtracted entirely and the reverberations are canceled. In the transition regions, the mean value estimate is subtracted partially.

This method was implemented and tested in the computer. The algorithm totally cancels *mirror leakage reverberations*. This is demonstrated in Figure 4.14. In (a) an unprocessed image is shown from an 8F 20 MHz rotating mirror catheter. Four reverberation sectors are visible close to the catheter (the strut is located from 12 to 3 o'clock). Figure 4.14(b) shows the processed image. All the reverberations are canceled effectively. (The black sector from 12 to 2 o'clock is due to startup conditions of the algorithm.)

4.4.4 Discussion and conclusion

Discussion: It is demonstrated by post processing realistic data that *mirror leakage reverberations* from the *rotating mirror catheter* can be detected and canceled. No testing is performed on *protecting tube reverberations*. The algorithm is expected to cancel *protecting tube reverberations* if the tube is located concentrically around the mirror or transducer axis. Eccentric tube location may however cause the phase to vary with the beam angle, which may reduce the effectiveness of the algorithm.

No testing is performed on signals containing reverberations plus blood signal (Sephadex particles). At frequencies where blood noise represents a problem, the mean and variance estimates from such signals are expected to be little different from signals from tissue plus blood. The variance will be high and the mean-value will probably be low. Detection and canceling of reverberations in the presence of blood noise is expected to be difficult.

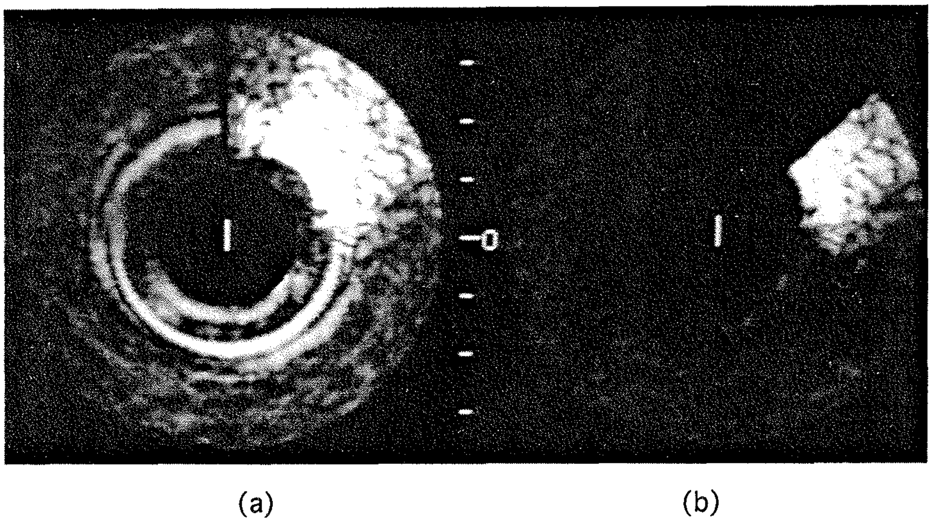

Figure 4.14 *The four mirror leakage reverberations seen in (a) are effectively canceled by the reverberation detection and canceling algorithm, see (b). A 20 MHz catheter (8F) from Cardiovascular Imaging Systems was dipped in water to obtain this image. The log-amp was included in the signal path.*

Conclusion: Detection and canceling of *constant phase catheter reverberations* is accomplished in areas where only electronic noise is present. The algorithm is base on a mean-value and a variance estimate in the lateral direction. Signal from vessel wall, electronic noise and *constant phase catheter reverberations* are distinguished by combining the two estimators to a *reverberation detector*. The algorithm is effective for reverberations located in the lumen at system frequencies below $\approx$15 MHz where blood noise is not a problem. No testing is performed with reverberations in combination with blood noise.

4.5 Vessel wall detection and blood noise canceling by frame to frame phase difference

This section describes an algorithm for *detecting* the presence of the vessel wall and *rejecting* the signal in other regions. The algorithm is based on temporal and spatial correlation properties of the vessel wall signal and the blood noise. The vessel wall signal is normally correlated from frame to frame while the blood signal is not. Electronic noise is also uncorrelated from frame to frame and will fall in the same category as blood noise. After processing an ultrasound image with the algorithm, the blood noise in the lumen is canceled as well as the electronic noise in the region outside the field of view (outside the penetration limit).

The algorithm is developed by analyzing acquired data and search for properties and algorithms that make it possible to distinguish vessel wall and blood signal, preferably in real time. The data acquisition is described in the following test setup:

> ***Test setup 4.6:*** *A thin rubber material was glued to the inside wall of a thin metal cylinder to mimic a blood vessel. The cylinder was located around the mirror shaft and the transducer in the test tank shown in Figure 3.2 with a thin metal piece acting as a spring.*
> *Vessel wall displacements were obtained by placing a water filled balloon in the test tank, touching the metal cylinder and the test tank wall. A hose connection was made from the balloon to the cardiac model described in Section 3.1.7. By applying a realistic cardiac blood pressure to the balloon, the expansion of the balloon generated a realistic translation of the cylinder. The movement was of the same order as has been observed in video tape studies of human and pig cases.*
> *Uncorrelated "blood" signal was obtained by flushing water containing Sephadex particles through the hose with high velocity (≈ 1 m / sec.).*
> *The transducer was a flat circular 20 MHz transducer. The log-amp was used during data collection. The beam density was N_b = 256 and the number of radial samples was N_r = 256.*
> *An example of an image from this setup is shown in Figure 4.19(e). The signal from the Sephadex particles represents a strong noise. Only a minor signal penetrates through the metal. The region outside the cylinder represents uncorrelated noise.*

4.5.1 Correlation properties

Temporal domain:
The correlation properties in the temporal direction are given by the temporal sampling rate (the frame rate), the radial and the angular dimensions of the sample volume, the velocity and the distribution of the scatterers. Blood scatterers traverse primarily through the sample volume in the beam angular direction. The velocities are high, up to 100 cm/sec. Vessel wall scatterers may traverse with both radial and angular velocity components due to catheter tip movements and vessel wall dilatation. These relative velocities are lower, approximately 1% of realistic blood velocities.

Adjacent samples in the temporal direction (frame to frame) will be 100% uncorrelated if no scatterers contribute to the signal more than once. A scatterer traversing with velocity "V" through the sample volume of length "L" will contribute only once if the transit time "T" is equal to or less than the sample interval:

$$T = \frac{L}{V} \leq \frac{1}{f_m} \tag{4.15}$$

This criterion yields a conservative limit to the scatterer velocity that causes adjacent temporal samples to be uncorrelated:

$$V_{uncorr} \geq L\, f_m \tag{4.16}$$

The dimensions of the sample volume are different in the radial and the angular directions. Approximate realistic values for the minimum velocity in these directions will be found by the following examples:

Minimum angular velocity: Assume a circular focused transducer. The beam diameter in the focal region versus range "r_o" is given by Equation 2.19:

$$D_{-12dB} \approx \frac{\lambda}{a}\, r_o = 2\,\frac{\lambda}{D}\, r_o \tag{4.17}$$

Inserted into Equation 4.16, this gives:

$$V_{\phi,uncorr} \geq D_{-12dB}\, f_m \approx \frac{\lambda\, r_o\, f_m}{a} \tag{4.18}$$

The following realistic values (λ=78μm, a=0.68mm, r_o=3mm and f_m=15 f.p.s.) give:

$$V_{\phi,uncorr} \geq 0.5 \text{ cm/sec} \tag{4.19}$$

Minimum radial velocity: The radial size of the sample volume "Δr" is equal to half the acoustic pulse length which is given by the velocity of sound and the fractional bandwidth of the transducer "K_{XD}". An approximate description is:

$$\Delta r \approx \frac{c}{2\, f_o\, K_{XD}} \tag{4.20}$$

Equation 4.20 inserted in Equation 4.16 yields:

$$V_{r,uncorr} \geq \Delta r\, f_m \approx \frac{c\, f_m}{2\, f_o\, K_{XD}} \tag{4.21}$$

The following realistic values (c=1560m/sec., f_m=15f.p.s., f_o=20MHz and K_{XD}=0.25) give:

$$V_{r,uncorr} \geq 0.2 \text{ cm/sec.} \tag{4.22}$$

Adjacent temporal samples will be uncorrelated for angular velocities exceeding ≈0.5 cm/sec. and radial velocities exceeding ≈0.2 cm/sec.

This means that blood signal will normally be uncorrelated. Exceptions are short instants when the blood flow changes direction in peripheral arteries. The signal from *stationary* vessel wall will be correlated. The signal from pulsating vessel wall will often be uncorrelated since there are radial dilatation velocities of up to ≈0.5 cm/sec. and the catheter tip velocity comes in addition.

Spatial domain:

To be able to distinguish blood and pulsating vessel wall signals, the image signal needs to be analyzed in the spatial domain as well. Vessel wall motions occur primarily in the beam scan plane: *radial* and *lateral* velocity components are dominating.

In case of noise free measurement, the following properties apply versus vessel wall and catheter tip movements:

1) Lateral translation: If the vessel wall rotates laterally around the catheter axis, the image signal from frame N will be identical to the image signal from frame N-1 except for a lateral lag, the two images are 100% correlated.

2) Radial translation, far field, constant scattering distribution: If the vessel wall moves radially without changes in the scattering distribution, and the far field approximation holds (within the focal region of a focused transducer for example), a pure radial lag is introduced, i.e. 100% correlation.

3) Near field or change in scattering distribution: In the transducer *near field*, the speckle pattern will change with radial displacement, even if the scatterer distribution is constant. The speckle pattern will also change if the *scattering distribution* changes due to radial dilatation (elastic wall). In both cases the spatial correlation will be less than 100%.

The signal from blood is uncorrelated in the temporal domain for velocities exceeding ≈0.5 cm/sec. In coronary arteries, the signal will be uncorrelated through the entire cardiac cycle. In peripheral arteries, the signal may be correlated during a short fraction of the cardiac cycle each time the flow changes direction.

The stationary vessel wall signal is correlated in the temporal and the spatial domain.

The signal from the pulsating vessel wall will generally not be correlated in the temporal direction.

The signal from the pulsating vessel wall will generally be correlated in spatial direction. A change in speckle pattern due to radial movements in the extreme near field or changes in scatterer distribution may limit the correlation.

4.5.2 Correlation estimators

To detect and discriminate pulsating vessel wall and blood signals based on their correlation properties, both the temporal and the spatial domain should be involved. It is reasonable to suggest a cross correlation function between two spatial regions from temporal adjacent frames. A cross correlation estimate (CC) was tested, but for several reasons it was rejected. Two other algorithms were tried: One based on *Averaging the Absolute value of Magnitude Differences* (AAMD), and another based on averaging *Phase Difference Unit Vectors* (PDUV).

Cross correlation (CC):

A cross correlation estimate was applied to the acquired data in one dimension at the time, in the radial or in the lateral direction. Two beams (256 samples) from the same angular direction "ϕ", but from adjacent frames (frame N-1 and frame N) were analyzed. Equivalently, two circles (256 samples) from the same depth "r", but from frame N-1 and frame N were analyzed.

In the radial direction, the cross correlation estimate is given by:

$$CC_r(N,r,\phi,\Delta r) = \frac{1}{n_r}\sum_{i_r=-x_r}^{x_r} QD(N,r,\phi)\, QD^*(N\text{-}1,\, r+\Delta r+i_r,\, \phi) \qquad (4.23)$$

$$x_r = \frac{n_r - 1}{2}$$

For each radial value "r", a sequence of "n_r" (an odd number) cross correlation product terms are averaged with a specified lag "Δr". The corresponding lateral cross correlation estimate is given by:

$$CC_\phi(N,r,\phi,\Delta\phi) = \frac{1}{n_\phi}\sum_{i_\phi=-x_\phi}^{x_\phi} QD(N,r,\phi)\, QD^*(N\text{-}1,\, r,\, \phi+\Delta\phi+i_\phi) \qquad (4.24)$$

$$x_\phi = \frac{n_\phi - 1}{2}$$

An example of the radial cross correlation estimate between two beams is shown in Figure 4.15 together with the magnitude of the two beams. The data is taken from the rubber vessel with Sephadex-immersed water flushing through as described in Test setup 4.6. Water and Sephadex is located in the region r=0mm to r=5mm. The signal levels are high in this region, the magnitudes are rarely equal. The rubber vessel is located from r=5mm to r=6.5mm. In this region the signals are also strong, but the magnitudes match well. The region outside the metal cylinder from r=6.5mm to r=10mm contains weaker electronic noise.

A segment length of $n_r = 11$ values was used to calculate $CC_r(N,r,\phi,\Delta r)$, and the lag parameter "Δr" was varied from -10 to +10. The magnitude of this radial cross correlation estimate is displayed as a mesh-plot with the radial *depth* "r" as one horizontal coordinate and the radial *lag* variable "Δr" as the other.

As can be seen in Figure 4.15, a peak is obtained for the stationary vessel wall signal. A radial displacement between the frames was introduced in another simulation and the peak was shifted from the center axis as expected. In order to detect and distinguish the pulsating vessel wall signal from blood signal, an algorithm is required that can detect a peak in this two-dimensional function.

Even though the Sephadex signal is uncorrelated in the temporal domain, this signal contributes significantly to the correlation estimate. This makes it difficult to distinguish vessel wall and blood noise. The reason why the uncorrelated signal contributes that much is: *limited observation length* and *limited signal bandwidth*, i.e. the *variance* of the cross correlation estimate is high.

The estimator yields low correlation in the electronic noise region, but this is due to weaker signal levels, not only the lack of correlation. The cross correlation estimate is signal level dependent. It favors strong signals that are correlated. Weak signals that are correlated get a lower score than strong correlated signals.

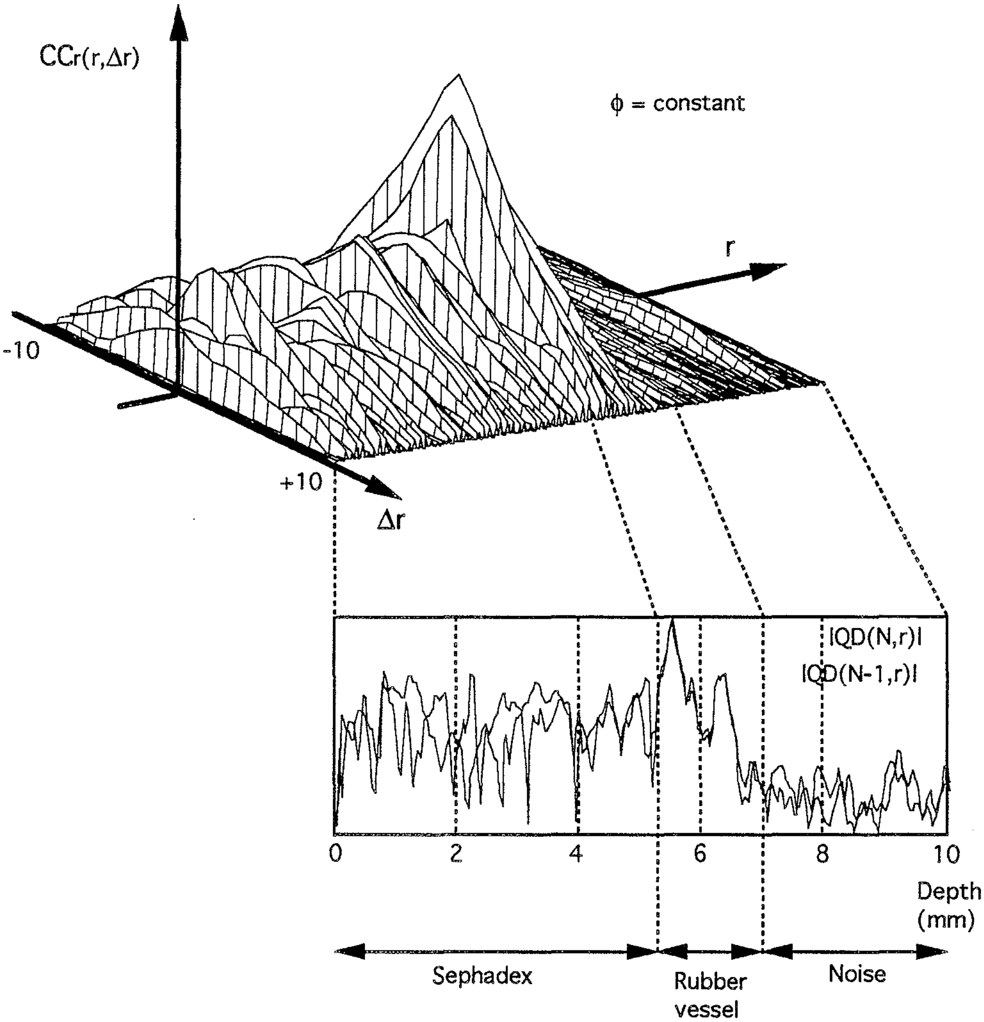

Figure 4.15 *Cross correlation between two temporarly adjacent beams containing signals from three different regions: Sephadex in water, rubber vessel and electronic noise.*

The radial cross correlation estimate is shown in the upper panel, while the magnitudes of the two beam signals are plotted in the lower panel.

For the following reasons, the cross correlation estimator was rejected, and the two other algorithms were tested:

1) The cross correlation estimator favors both *correlation* properties and signal *strength*. Weak vessel wall signals with high correlation get a lower score than strong correlated signals.
2) Vessel wall motion should be tracked by detecting the peak in the two-dimensional cross correlation function. Introducing a lag in the correlation operation causes a dramatic increase in the computational power requirement.
3) To increase the detectability, the variance should be reduced. This can be done by increasing the spatial size of the two input regions, for example to a two-dimensional kernel. This would further increase the computation requirements.

Average Absolute Magnitude Difference (AAMD):

The magnitude of the complex quadrature demodulated signals from adjacent frames will be identical in regions with stationary vessel wall signal (assume no noise and no catheter movements). The *magnitude difference* is zero. In blood regions, the two signals will rarely be equal: the magnitude difference will vary strongly within a spatial region, positive and negative values will occur. This can be seen in the lower panel of Figure 4.15.

By "rectifying" the magnitude difference, the following estimator term can be defined: *Average Absolute Magnitude Difference* (AAMD). This estimator was applied to one-dimensional data sequences from the acquired data sets. In the radial direction "n_r" radial values were averaged according to:

$$\mathrm{AAMD}_r(N,r,\phi,\Delta r) = \frac{1}{n_r} \sum_{i_r=-x_r}^{x_r} \left| \, |QD(N,r,\phi)| - |QD(N-1, r+\Delta r+i_r, \phi)| \, \right| \tag{4.25}$$

$$x_r = \frac{n_r - 1}{2}$$

and in the lateral direction:

$$\mathrm{AAMD}_\phi(N,r,\phi,\Delta\phi) = \frac{1}{n_\phi} \sum_{i_\phi=-x_\phi}^{x_\phi} \left| \, |QD(N,r,\phi)| - |QD(N-1, r, \phi+\Delta\phi+i_\phi)| \, \right| \tag{4.26}$$

$$x_\phi = \frac{n_\phi - 1}{2}$$

This estimator is simpler to compute and performs quite well in detecting and distinguishing vessel wall and blood signal. However, the ***AAMD-estimator is very sensitive to vessel wall displacements***, especially if the signals contain steep edges. It is therefore ***necessary to introduce lag*** and search for the presence of the vessel wall. This increases the computation requirement dramatically. For this reason, this estimator is also rejected.

Sum-based estimators are simpler and faster to implement than multiplication-based estimators. Jacovitti describes how the so-called *Average Magnitude Difference Function* (AMDF) can be used to estimate the normalized autocorrelation function for stationary processes [Jacovitti 1987]. The AAMD-algorithm is related to the AMDF-algorithm described by Jacovitti.

Phase Difference Unit Vector (PDUV):

It is found that the general cross correlation function is not well suited for vessel wall detection due to its signal level sensitivity and the complexity related to a real time implementation. The estimator based on the magnitude information is sensitive to displacements and it is rejected for that reason. An estimator based on *phase information only* is tested. This estimator is independent of the signal levels and as will be seen, less sensitive to displacements. It is not necessary to introduce lag and search for the pulsating vessel wall.

The phase difference between two adjacent frames is represented by unit vectors, the phase of each vector equals the phase difference between two quadrature demodulated samples. This is described by the following equation where the term *Phase Difference Unit Vector* (PDUV) is defined for a spatial location (r,ϕ):

$$\mathrm{PDUV}(N,r,\phi) = \frac{\mathrm{QD}(N,r,\phi)\,\mathrm{QD}^*(N-1,r,\phi)}{\left|\,\mathrm{QD}(N,r,\phi)\,\mathrm{QD}^*(N-1,r,\phi)\,\right|} \qquad (4.27)$$

In a *stationary vessel wall region* (with no noise or catheter tip movements), the phase of two temporal adjacent samples will be identical. The phase difference is *zero*. With a small radial displacement of the vessel wall (less than the distance between radial sample points) the phase difference will be zero or close to zero. Observed over a certain radial region, all the phase differences will be small. In contrast, in a *blood region*, the phase differences will fluctuate strongly between 0 and 2π when observed over a radial region. By averaging the *phase difference unit vectors* in the radial direction and extracting the magnitude of the complex average, a *Radial Phase Difference Magnitude* (RPDM) estimate is obtained, defined by:

$$\mathrm{RPDM}(N,r,\phi) = \left|\, \sum_{i_r} \mathrm{PDUV}(N,\, r+i_r,\, \phi) \,\right| \qquad (4.28)$$

The corresponding *Lateral Phase Difference Magnitude* (LPDM) is:

$$\mathrm{LPDM}(N,r,\phi) = \left| \sum_{i_\phi} \mathrm{PDUV}(N, r, \phi+i_\phi) \right| \tag{4.29}$$

Figure 4.16 illustrates the method of discriminating vessel wall and blood signals by the phase difference. In (a), eight adjacent radial values of the PDUV are taken from a vessel wall region. All vectors have approximately the same phase. Complex averaging and magnitude detection yields a real valued number close to 1. In (b) an equivalent sequence from a blood region is shown. The phases are randomly distributed, and the magnitude of the average is small, close to 0.

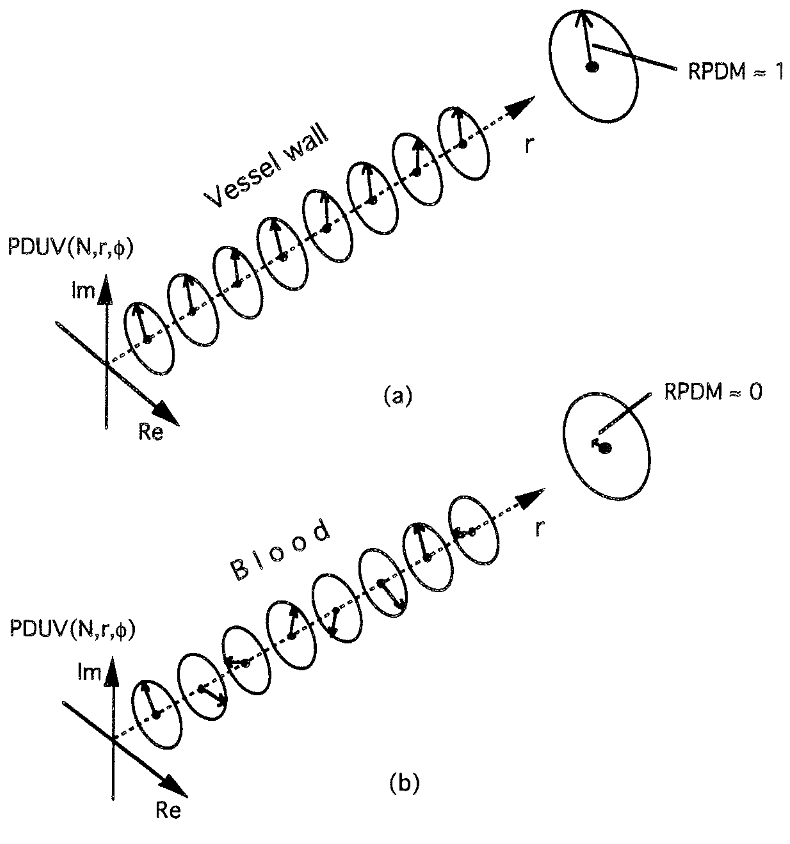

Figure 4.16 *Typical Phase Difference Unit Vector (PDUV) versus range in:*
(a) a vessel wall region, the phase differences are almost equal, RPDM ≈1.
(b) a blood region, the phase differences are randomly distributed, RPDM ≈0.

When applied to the acquired data, the *radial phase difference magnitude* estimator *(RPDM)* was found to be robust against radial vessel wall movements, and the *lateral phase difference magnitude estimator* (LPDM) was found to be robust against lateral vessel wall movements.

The vessel wall signal estimate based on the *phase difference unit vector* is not as sensitive to displacement as the estimator based on the magnitude. According to the measurements , ***it is not necessary to introduce lag and search for a peak value.*** This makes this estimator suitable for real time implementation.

The *radial and lateral phase difference* estimators are based on averaging the normalized cross correlation product in Equation 4.27, i.e. normalizing *prior to* averaging. These estimators are expected to be related to the *cross correlation coefficient* estimate "$\rho(N,r,\phi)$" since the latter estimate represents normalizing *after* averaging of the same kernel:

$$\rho(N,r,\phi) = \frac{\sum QD(N,r,\phi)\ QD^*(N-1,r,\phi)}{\sqrt{\sum |QD(N,r,\phi)|^2 \sum |QD(N-1,r,\phi)|^2}} \tag{4.30}$$

The *cross correlation coefficient* estimate "$\rho(N,r,\phi)$" is not tested for the purpose of vessel wall detection.

4.5.3 Vessel wall detection algorithm

This section describes the vessel wall *detection* algorithm in detail. The description is supported with some results from an example to visualize the most important steps in the algorithm. This example is described in *test setup 4.6* (in the introduction to Section 4.5). Acquired data were transferred to the computer, processed and various estimators of the algorithm were displayed as images. The results are visualized with a photo of the computer monitor in Figure 4.19.

The magnitude detected image of the rubber vessel is shown in Figure 4.19(e). The Sephadex particles reduce the contrast between the lumen and the vessel wall, and only a minor signal penetrates through the metal cylinder. The region outside the cylinder represents electronic noise.

Phase Difference Image:

The first step in the algorithm is to calculate the *phase difference unit vector* $PDUV(N,r,\phi)$ in Equation 4.27 for all spatial locations in two adjacent frames. For illustration, the angles of all these vectors are displayed as a gray level intensity image on the monitor: 0 equals black and 2π equals white. This *phase* *difference image* is shown in Figure 4.19(a). In regions with Sephadex and electronic noise, the phase difference appears as a random white noise process. In the vessel wall region, the phase difference changes slowly, the spatial frequency content in the phase difference is low. The phase *difference* image contains information about correlation properties. In contrast, the *individual* phase images do not, the phase appears as a random noise over the entire image.

Radial and lateral vessel wall detector:

The next step of the algorithm is to calculate the *radial and lateral phase difference magnitudes:* RPDM and LPDM defined in Equations 4.28 and 4.29. In the radial direction, "R_{NR}" values are averaged. In the lateral direction, "L_{NL}" values are averaged:

$$\mathrm{RPDM}(N,r,\phi) = \left| \frac{1}{R_{NR}} \sum_{i_r = -x_r+1}^{x_r} \mathrm{PDUV}(N, r+i_r, \phi) \right| \tag{4.31}$$

$$x_r = \frac{R_{NR}}{2}$$

$$\mathrm{LPDM}(N,r,\phi) = \left| \frac{1}{L_{NL}} \sum_{i_\phi = -x_\phi+1}^{x_\phi} \mathrm{PDUV}(N, r, \phi+i_\phi) \right| \tag{4.32}$$

$$x_\phi = \frac{L_{NL}}{2}$$

With the parameters used in the test: $R_{NR} = 20$ and $L_{NL} = 10$, (these values were found experimentally to yield a reasonable compromise between variance and resolution of the estimates) the ***variance was unacceptable high*** for RPDM and LPDM to be used for vessel wall detection. The variance can be reduced by: 1) increasing the number of samples averaged: "R_{NR}" and "L_{NL}" (at the expense of the resolution of the estimates). 2) by averaging the *radial phase difference magnitude* in the lateral direction and average the *lateral phase difference magnitude* in the radial direction. The latter method is selected yielding the: *Radial Vessel Wall Detector* (RVWD) and the *Lateral Vessel Wall Detector* (LVWD) respectively:

$$\mathrm{RVWD}(N,r,\phi) = \frac{1}{R_{NL}} \sum_{i_\phi = -y_\phi+1}^{y_\phi} \mathrm{RPDM}(N,r,\phi+i_\phi) \tag{4.33}$$

$$y_\phi = \frac{R_{NL}}{2}$$

$$\mathrm{LVWD}(N,r,\phi) = \frac{1}{L_{NR}} \sum_{i_r=-y_r+1}^{y_r} \mathrm{LPDM}\,(N,r+i_r,\phi) \tag{4.34}$$

$$y_r = \frac{L_{NR}}{2}$$

The abbreviations are supposed to be read:
R_{NR}: Radial estimator, Number of Radial elements
R_{NL}: Radial estimator, Number of Lateral elements
L_{NL}: Lateral estimator, Number of Lateral elements
L_{NR}: Lateral estimator, Number of Radial elements

Figure 4.17 illustrates how the *radial and lateral vessel wall detectors* are calculated by averaging in the radial and lateral directions.

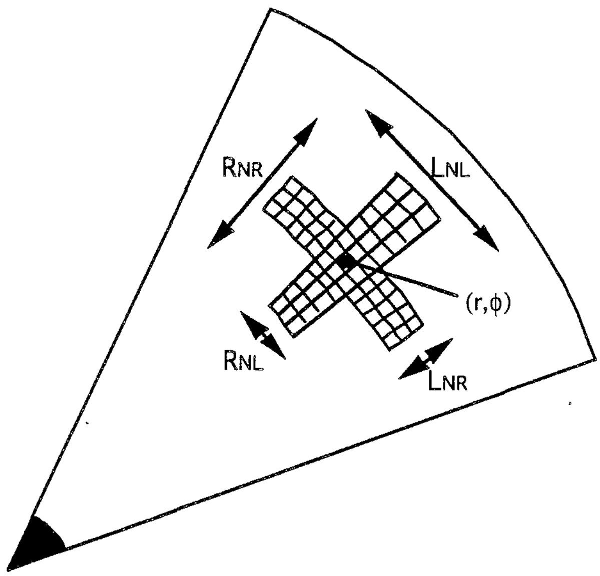

Figure 4.17 *For each location (r, ϕ) in the image, a radial vessel wall detector (RVWD) and a lateral vessel wall detector (LVWD) are calculated:*

RVWD(N,r,ϕ) is generated by averaging R_{NR} radial complex samples and do magnitude detection. This operation is repeated for R_{NL} adjacent lateral locations and the result averaged to reduce the variance.

LVWD(N,r,ϕ) is generated by averaging L_{NL} lateral complex samples and do magnitude detection. This operation is repeated for L_{NR} adjacent radial locations and the result averaged to reduce the variance.

The following parameters were used in the illustration test (not optimized): $R_{NL} = 3$ and $L_{NR} = 3$. The *radial vessel wall detector* is a number between 0 and 1, 0 representing blood or electronic noise and 1 representing vessel wall signal. This detector is displayed as a gray level image with zero as black and one as white in Figure 4.19(b). The lateral vessel wall detector is shown in (c). (To obtain this appearance, the detector images were passed through a compression curve in the display program.)

Phase Difference Vessel Wall Detector:
In regions with blood, both the *radial and lateral vessel wall detectors* will be close to 0. In regions with a stationary vessel wall, both will be close to 1. In regions with a pulsating vessel wall, at least one of the detectors will be close to 1. This calls for an OR-operation between the two. One possible (intuitive) realization is the "smooth OR-operation" illustrated schematically in Figure 4.18. The output of this function is denoted: *Phase Difference Vessel Wall Detector* (PDVWD).

Figure 4.19(f) shows the *phase difference vessel wall detector* displayed as a gray level image. The location of the rubber vessel is described precisely, and only a few dropouts are found in the lumen. (The discontinuity at 12 o'clock is due to start up conditions of the algorithm.)

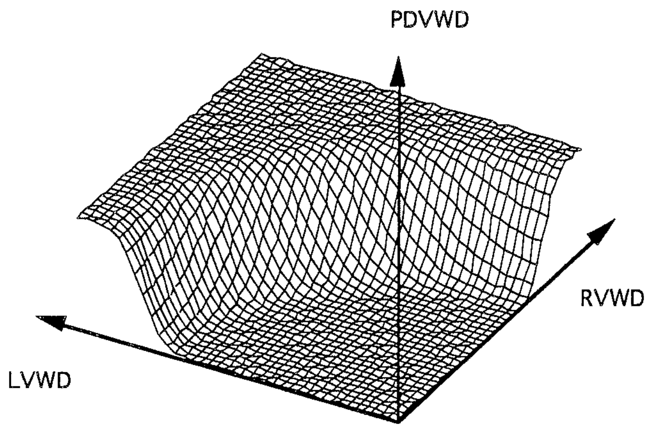

Figure 4.18 *Schematically illustration of the implemented "smooth OR function" that combines the radial and lateral vessel wall detectors to the phase difference vessel wall detector.*

4.5.4 Blood noise canceling, test results

A robust vessel wall detector is developed. It represents a spatial description of the probability that a specific sample belongs to a vessel wall region. This detector is used to manipulate the original image, the magnitude detected version of frame N. Two methods to cancel noise are suggested:

1) The original magnitude detected image is *multiplied* with the *phase difference vessel wall detector*. This results in an almost completely black lumen which is undesirable for two reasons: a) Ultrasound users often like to see a certain degree of background noise to be sure that the entire dynamic range of the instrument is in use. b) When the estimator fails, the consequences will be very dramatic, especially if a bright vessel wall signal is detected as blood and displayed in black.

2) A better method is to pass the magnitude detected image through a digital lookup table that realizes a family of input/output mappings. The *phase difference vessel wall detector* is used to select the mapping. When the $PDVWD(N,r,\phi) = 1$ (vessel wall), a linear curve is used. The original image sample is passed through with no modifications. When $PDVWD = 0$ (blood or uncorrelated noise), a curve with hard rejection is selected. For values between 0 and 1, mappings between the two extremes are applied. Each particular sample of the magnitude detected image $|QD(N,r,\phi)|$ is adjusted according to its corresponding *phase difference vessel wall detector* value $PDVWD(N,r,\phi)$.

The latter method is applied to the test described in the previous section, see Figure 4.19(f).

The result is an almost noise free image. Strong (uncorrelated) blood noise and weak (uncorrelated) electronic noise is effectively canceled. The vessel wall is passed through with negligible distortion.

The blood noise canceling effect should be user-adjustable. This can be accomplished by adding several I/O-mapping families to the lookup table. When the blood canceling is switched off, all I/O mappings are linear. The signals are passed through with no modifications. When the algorithm is fully effective, the above situation is described. A very hard rejection is applied to blood regions. A desirable number of I/O-mapping families between these two extremes can be implemented. This method is not tested.

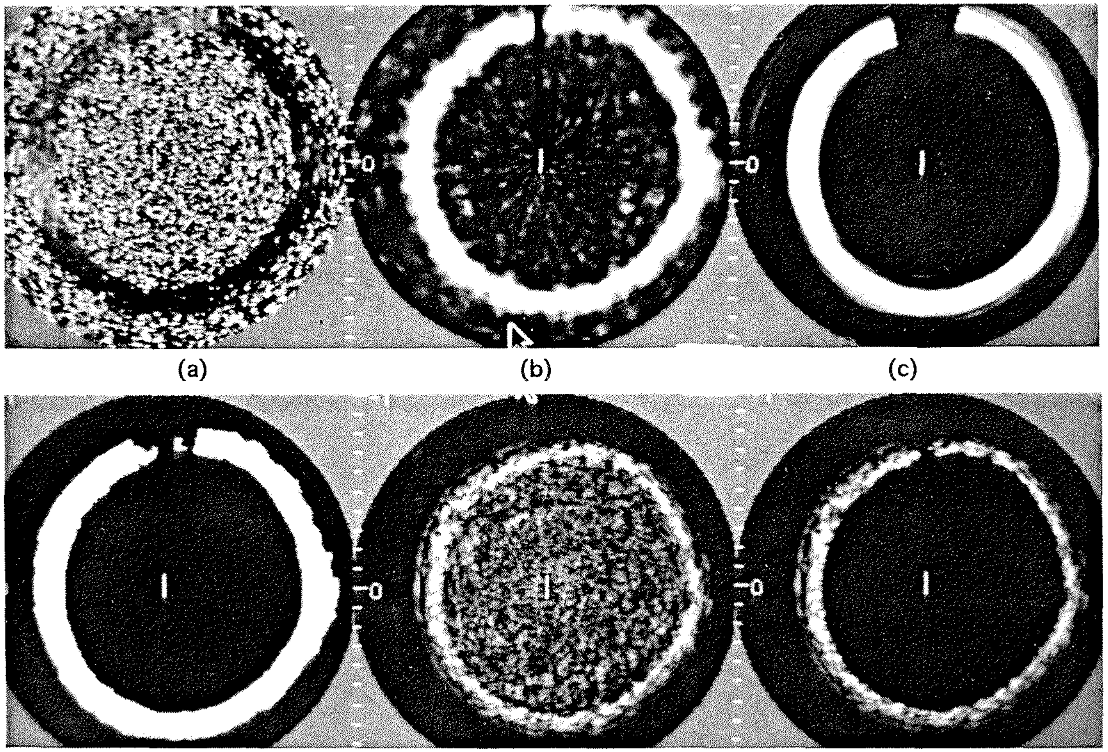

(a) (b) (c)

(d) (e) (f)

Figure 4.19 *Images illustrating the process of detecting vessel wall signal by complex phase difference between adjacent frames.*

(a) The phase difference unit vestor: PDUV(N,r,ϕ) (displayed as gray levels: 0=black, 2π =white).

(b) Radial Vessel Wall Detector: RVWD(N,r,ϕ) (R_{NR} =20, R_{NL}=3)

(c) Lateral Vessel Wall Detector: LVWD(N,r,ϕ) (L_{NL}=20, L_{NR} =3)

(d) Phase Difference Vessel Wall Detector: PDVWD(N,r,ϕ)

(e) The original magnitude detected image: | QD(N,r,ϕ) |

(f) Noise rejected image. The image in (e) is manipulated by the phase difference vessel wall detector in (d).

Real time cineloop testing:
The vessel wall detector based on phase difference between adjacent frames is found to be more robust against vessel wall movements than the "CC" and "AAMD"-estimators. This performance was briefly tested by an experiment where a realistic movement of the rubber vessel was applied (see test setup 4.6). Ten images were acquired during one cardiac cycle. Nine processed frames were displayed in a real time cineloop side by side with an unprocessed loop.

In this single experiment, the Sephadex noise canceling effect was similar to the result shown in Figure 4.19(f) for all images: except for a few dropouts, a black lumen was obtained. The rubber vessel wall was represented with negligible distortion, but the transition region between the vessel wall and the Sephadex was slightly blurred. The electronic noise region outside the cylinder was effectively canceled.

4.5.5 Vessel wall detector variance

The so-called "uncertainty relation" can be applied to the *phase difference vessel wall detector*. In radar applications this relation states that the product of the signal bandwidth and the duration of the signal should be no less than π [Skolnik 1962]. In signal processing, the uncertainty relation is a consequence of the Fourier transform relation between time and frequency domain. A narrow pulse in the time domain yields a broad spectrum and vice versa. The pulse duration and the spectrum cannot be made arbitrarily small simultaneously.

For a stochastic signal like an ultrasound image signal, the product of the bandwidth "BW" and the observation length "T_{obs}" is a measure of the amount of information that can be extracted from signal. It is assumed here that the variance of a correlation estimate is inversely proportional to the amount of information in the signal. According to this, a simplified expression for the variance of a correlation estimator can be written:

$$\mathrm{Var(CorrEst)} \sim \frac{1}{BW\, T_{obs}} \tag{4.35}$$

The observation length "T_{obs}" equals the sampling interval "T_s" times the number of elements averaged "N_a".

$$\mathrm{Var(CorrEst)} \sim \frac{1}{BW\, N_a\, T_s} = \frac{1}{N_a\, BW/f_s} = \frac{1}{N_a\, BW_{Rel}} \tag{4.36}$$

where the relative bandwidth "BW_{Rel}" is introduced.

Applied to the *radial phase difference magnitude* estimate, the result is:

$$\mathrm{Var(RPDM)} \sim \frac{1}{\mathrm{BW_{rRel}}\, \mathrm{R_{NR}}} \tag{4.37}$$

where "$\mathrm{BW_{r\,Rel}}$" is the relative bandwidth in the radial direction. Accordingly:

$$\mathrm{Var(LPDM)} \sim \frac{1}{\mathrm{BW_{\phi Rel}}\, \mathrm{L_{NL}}} \tag{4.38}$$

The variance of the *radial and lateral phase difference magnitude* estimators were reduced by averaging in the perpendicular direction (Equation 4.33 and 4.34). It is here assumed that adjacent values are independent, i.e. the variance is inversely proportional to the number of samples averaged. The variance of the *radial and lateral vessel wall detectors* is then given by the following approximate expressions:

$$\mathrm{Var(RVWD)} \sim \frac{1}{\mathrm{BW_{rRel}}\, \mathrm{R_{NR}}\, \mathrm{R_{NL}}} \tag{4.39}$$

$$\mathrm{Var(LPDM)} \sim \frac{1}{\mathrm{BW_{\phi Rel}}\, \mathrm{L_{NL}}\, \mathrm{L_{NR}}} \tag{4.40}$$

These equations indicate that the quality of the vessel wall detector can be improved by increasing the number of samples averaged in the radial and the lateral direction, or by increasing the relative bandwidth in the lateral and the radial direction.

4.5.6 Discussion and conclusion

Discussion: The algorithm is developed by analyzing and characterizing data that is collected in an idealized test setup. In real cases, other signal characteristics will come into account. The most important are:

Very low blood velocities: The algorithm is expected to fail when the blood velocity is below ≈ 0.5 cm/sec. for a time interval equal to or longer than the time between two frames. This is most likely to occur in peripheral arteries when the blood flow changes direction, but no testing is performed to see if this is a problem or not.

Non-uniform rotation distortion (NURD): The test tank with no NURD was used in the tests. The experiments indicate that the algorithm is robust against lateral movements. The algorithm is therefore expected to handle the amount of NURD that is observed in the catheters used in this work (They were lubricated with glycerol and are expected to represent a worst case NURD-situation). However, this is not tested.

Radial dilatation and catheter tip movements: The testing of movements between the vessel wall and the catheter (mirror) was limited to a realistic *translation* of the cylinder. Realistic vessel wall expansion and catheter tip translations are not simulated carefully. This means that the speckle pattern may alter due to changes in the scattering distribution or due to radial movements in the near field. (The latter can to a certain degree be compensated for by using a focused beam.) If the speckle pattern changes, the correlation will drop, and the probability of correct detection will decrease.

Conclusion: The blood noise reduction algorithm based on the phase difference between adjacent frames is effective for blood velocities exceeding ≈ 0.5 cm/sec. The algorithm is not optimized with respect to statistical properties of the signals. There may be room for improvements by changing the number of samples to average and by changing the shape of the OR-function. Nevertheless, the presented algorithm is robust to vessel wall and catheter tip movements without introducing lag and searching for a peak. It is shown in Chapter 5 that the algorithm is cost effective to implement in real time.

Chapter 5

REAL TIME NOISE FILTERING

In Chapter 4, algorithms for noise reduction were described and tested by post processing on a computer. This chapter describes how these algorithm can be implemented in real time in the instrument. Four different *methods* were described in Chapter 4:

1) *Blood noise* reduction by beam tilting and lateral low-pass filtering.
2) *Uncorrelated electronic noise* reduction by lateral oversampling and low-pass filtering.
3) Lateral detection and canceling of *mirror leakage* and *protecting tube reverberations*.
4) Detection and canceling of *blood noise* and *uncorrelated electronic noise* by frame to frame phase difference.

The first two methods are based on the same algorithm: lateral low-pass filtering. It is found that blood noise is more effectively reduced by method 4. For simplicity reasons, lateral low-pass filtering will be denoted: ***Uncorrelated electronic noise filter*** although it also reduces blood noise.

Two types of catheter reverberations are reduced by method 3. In this chapter this method will be denoted: ***Reverberation filter***.

The fourth method is also effective for two noise types, blood and uncorrelated electronic noise. Since blood noise reduction is its primary purpose, the fourth method will be denoted: ***Blood noise filter***.

Two solutions are presented in this chapter:

1) Section 5.2 presents a hardware-solution of all three filters based on Digital Signal Processors (DSP). This solution is *possible*, but *not cost effective*. This section does also serve as a functional description of the implementation.

2) Section 5.3 describes a fast and cost effective implementation of two of the three filters (the *Uncorrelated electronic noise filter* and the *Blood noise filter*) based on conventional electronics or programmable logic.

5.1 Introduction

5.1.1 Processing speed requirements

The noise filters operate basically at two different data rates.

1) The *Uncorrelated electronic noise filter* is supposed to filter the (laterally oversampled) raw data from the AD-converters. This can either be done at the maximal data rate from the AD-converters "DR_{ADmax}" ($\approx 20 \cdot 10^6$ words/sec) or at the average data rate "DR_{ADave}" which is lower ($\approx 1 \cdot 10^6$ to $20 \cdot 10^6$ words/sec).

2) The *Reverberation noise filter* and *Blood noise filter* process decimated data on the same format as the display unit. The maximal display data rate "$DR_{DispMax}$" is normally lower ($\approx 1 \cdot 10^6$ words/sec) than the maximum and average data rates from the AD-converters.

The maximum data rate from the AD-converters equals the radial sampling rate. The default value for the system used in this work is $f_{rs} = 20$ MHz according to Section 3.1.2 (100% oversampling). The minimum radial sampling frequency is in general determined by two times the maximum frequency component in the signal. If the dual sided bandwidth of the transducer is 100% and a 40 MHz transducer is considered, the radial sample frequency should be no less than 20 MHz.

A realistic upper limit to the *maximum data rate from the AD-converters* in words/second is:

$$DR_{ADmax} = 20 \cdot 10^6 \text{ words/sec.} \tag{5.1}$$

The *average data rate from the AD-converters* is given by the number of radial samples "N_r", the beam density "N_b" and the frame rate "f_m":

$$DR_{ADave} = N_b \, N_r \, f_m \tag{5.2}$$

The default value of the system is (N_r=256, N_b=256 and f_m=15):
$DR_{ADave} \approx 1 \cdot 10^6$ words/sec.

Tradeoffs between the degree of lateral oversampling and processing requirements can be made. The data can be stored in a fast memory at the maximum data rate and be processed at a rate no lower than the average data rate. However, in order to take full advantage of the method of lateral oversampling and filtering, the noise filter should be able to operate at a speed close to the maximum data rate from the AD-converters.

Lateral decimation from acquired beam density "N_b" to displayed beam density "N_{bDisp}" is supposed to be done after the *Uncorrelated electronic noise filter*. This operation reduces the data rate further. The display format of the instrument is: N_{bDisp}=256 beams of N_{rDisp}=256 radial samples (see Section 3.1.2). Maximum display data rate of the system is then ($f_m \approx 30$ f.p.s.):

$$DR_{DispMax} = N_{rDisp} N_{bDisp} f_m \approx 2 \cdot 10^6 \text{ bytes/sec.} \tag{5.3}$$

5.1.2 Available processing components

The noise filters can be implemented in many different ways, the architecture depends of the selected components. Many factors should be taken into account when the architecture is decided, the most important are: performance, development cost, production cost, ability to maintain, flexibility to further develop the system, reliability, testability, board real estate and power dissipation.

The implementation of the digital noise filters is described on a block diagram level by two building blocks: *Digital Signal Processing Units* (DSPU) and *Memory devices* (MEM). The most relevant components or technologies available today and some of their main properties are listed in the following:

Digital signal processing components (DSPU):

Custom design: Custom designed integrated circuits can realize large and complex function on a small real estate. Both DSPU and MEM devices can be realized with this technology at high processing speed. The development cost is high, but in large volume production, the unit price can be low. The flexibility of the design is very low, the architecture cannot be changed when silicone is made. The reliability is high.

Discrete components: Conventional digital components requires large real estate, and many solder points and connections reduce the reliability. The development and production cost is high. Speed is high. Both MEM and DSPU can be realized, but the flexibility is low.

Dedicated DSP's: Dedicated digital signal processors execute a few special operations at high speed. They typically perform a certain number of multiplications and additions in parallel, and they and are well suited for filtering and correlation. The filter coefficients can easily be changed, but otherwise the structure is fixed. They fall primarily in the DSPU-group and offer quite high density on small real estate.

General DSP's: General Digital Signal Processors (DSP) offer high flexibility at the expense of speed (compared to dedicated processors). They naturally belong to the DSPU-group, but the built in memory is normal. The development trend in this field is to increase the amount of parallel operations.

Some relevant manufacturers are: Texas, Analog Device, Motorola, AT&T and Sharp. The first four manufacturers seem to deliver DSP's with approximately the same performance. The architecture, instructions and instruction cycle time differ slightly, but they are comparable. The typical instruction cycle time is 25-100 nsec. The LH9124 (262 pins) from Sharp is more powerful. It is designed with a high degree of parallelism, *complex* 8 bits data processing is default. The instruction cycle time is ≈25 nsec. An address generator (LH9320, 52 pins) circuit is required in addition to the DSP.

These circuits provide high flexibility in the development phase and during maintenance and further development.

Programmable logic: A very powerful and fast developing tool is the *field programmable gate array* (FPGA). The market leaders today are ALTERA, XILINX and ACTEL. These components offer high density circuits where the HW-structure and function can be specified through the use of SW-tools. The number of input and output pins is high (up to 300) and can be freely configured.

They are well suited for state machines, counters, combinatorial logic etc. The XILING circuits are configured from a built in RAM that is loaded serially after power up. The content of this RAM can be reloaded by the user so that the entire function of the device can be changed. These circuits are in addition well suited for memory purposes (RAM and FIFO's) and simple ALU-functions. The configuration RAM is released after configuration and can be used as general internal RAM by the device.

FPGA's are ideal for prototyping and development where the algorithms are not yet totally defined. The density is high, but lower than full custom design. Reliability is also high. The development tools are still expensive (ALTERA ≈75.000 NOK in 1992).

Memory devices:

FIFO: The FIFO is a one-dimensional memory where writing and reading is totally decoupled. This is a very useful component for interconnecting devices with different data rates.

Static and dynamic RAM:
Static and dynamic RAM is available in a variety of sizes and speeds, large memory size to a low price is available. Two-dimensional memories can easily be realized. However, read and write cannot be done simultaneously which limits the use of these devices. This problem can be overcome by the "ping pong" method: use two memories, read from one while writing to the other, then changing the roles.

Dual port RAM: These devices make simultaneous read and write access possible (except at the same location). In contrast to a conventional RAM they contain *two parallel data ports* and *two address ports*. These circuits are well suited for interconnecting two DSPU's. A disadvantage is relatively high price versus memory size compared to static and dynamic RAM.

Video-RAM: These devices are dual port RAM's, but instead of having two parallel random access ports, they have one random access port and one serial port. The data flow can be in either direction. Video RAM is well suited for applications where a high speed serial data flow and a relatively slow random access data rate is acceptable. They find wide applications in the computer market which brings the price down.

Memory cards: Memory cards of approximately the size of a credit card are available. They offer very high memory capacity versus price, up to 40 MB is currently available. In ultrasound imaging they may be used to store several images for the purpose of cineloops or to store three-dimensional data. By the "ping pong" technique, one memory card may be filled with acquired data while an other is subject to digital signal processing.

In the myriad of available components, tradeoffs have to be made. Since the noise filter algorithms are not fully tested in real situations, a great deal of flexibility in the design is desirable. Components under software control offer flexibility: *digital signal processors* and *field programmable gate arrays*. Two different architecture's are suggested in this chapter, one based on *digital signal processors* and one based on *field programmable gate arrays*.

5.2 A complete solution based on general digital signal processors

5.2.1 Block diagram

The block diagram for a complete solution is shown in Figure 5.1 including the *Uncorrelated electronic noise filter*, the *Reverberation filter* and the *Blood noise filter*. *Uncorrelated electronic noise filtering and decimation* is performed by a digital signal processing unit (DSPU) labeled (1). The other two filters are realized by three DSPU's: the *Reverberation detector* labeled (2), the *Vessel wall detector* labeled (3) and the *Noise filter* block labeled (4). Suggestions to the required number of bits are labeled in brackets.

Lateral oversampling can be accomplished by a *phase locked loop* (PLL) circuit which outputs "$K_{\phi Dec}$" pulses per input pulse from the angle sensor (an optical encoder). The output of the PLL-circuit drives the transmitter which transmits "N_b" pulses per revolution.

The received signal is passed through the RF-frontend and the quadrature demodulator. The in-phase and quadrature component are digitized by two (8 bits) AD-converters and written to a two-dimensional memory device denoted *QDRawData*.

The *Uncorrelated electronic noise filter and decimation* circuit labeled (1) is supposed to realize a lateral low-pass filters at each of the "N_r" depth locations. Due to lateral decimation, only every "$K_{\phi Dec}$" is outputted. Three separate MEM-devices are used to simplify synchronization between the DSPU's. In this way the processing units can access their data without any conflict with other processors.

The *Reverberation detector* circuit labeled (2) performs a lateral mean-value (m_ϕ) and variance (σ_ϕ^2) estimate. Based on these two estimates, the Reverberation Detector (RD) is generated. The lateral mean-value estimate is multiplied with the *reverberation detector* to obtain the Reverberation Mean Estimate (RevMeanEst) which is written to a memory device.

The *Vessel wall detector* labeled (3) reads the complex data from two adjacent frames and calculates the *phase difference unit vector*. A radial and lateral vessel wall detector is generated and combined in an OR-function to the Phase Difference Vessel Wall Detector (PDVWD).

The *Noise filter* in block (4) combines data from three memories to a final noise canceled image. The original complex image is read from memory and the *reverberation mean estimate* is subtracted to cancel catheter reverberations. This signal is magnitude detected and passed through a blood noise canceling function, a lookup table where the I/O-mapping is individually selected for each pixel by the corresponding *phase difference vessel wall detector*.

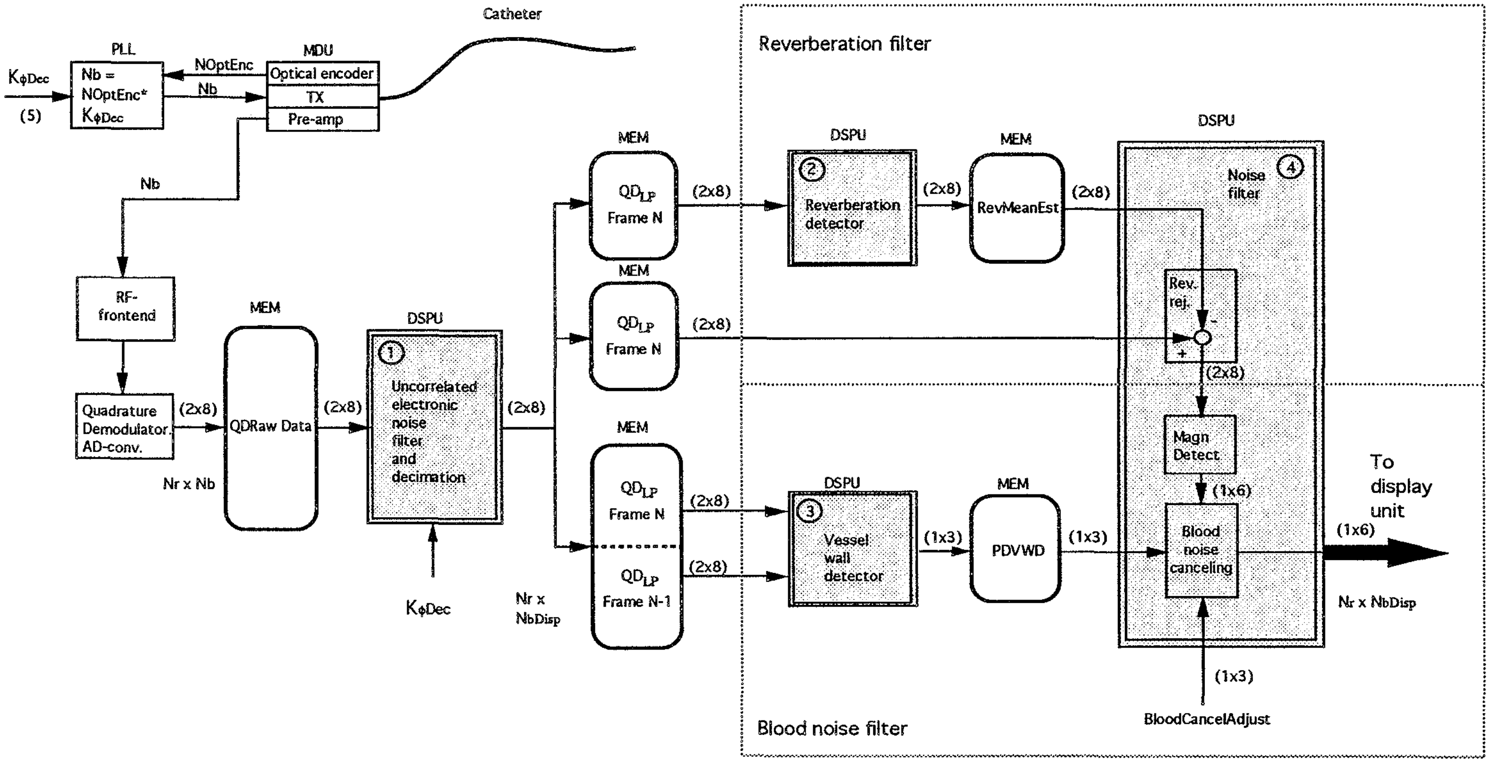

Figure 5.1 *Block diagram of the complete solution based on general digital signal processors.*
Uncorrelated electronic noise filter and decimation *is performed in DSPU labeled (1)*
Reverberation filter *is performed in (2) and (4).*
Blood noise filter *is performed in (3) and (4).*

5.2.2 Uncorrelated electronic noise filter and decimation

Several processors have to be used in parallel in order to filter the signal in the lateral direction at an average data rate of up to DR_{ADmax}. One way to share the job is to let each processor filter a certain number of depth locations. Figure 5.2 illustrates how this can be accomplished by fragmenting the memories.

In Section 4.3, two relevant filters were described, a 14th order FIR-filter and an *averaging filter*, both symmetric. The former filter executes slower than the *averaging filter* when implemented on a general DSP. The processing requirements of the averaging filter will be found to determine a *minimum* number of DSP's required. An (N-1) order averaging filter (average N values) is expressed by the following two equations:

$$\mathrm{Temp}(n_r, n) = \mathrm{Temp}(n_r, n\text{-}1) + \mathrm{QD}(n_r, n_\phi) - \mathrm{QD}(n_r, n_\phi\text{-}N) \tag{5.4}$$

$$\mathrm{QDLP}(n_r, n_{Disp}) = \left\{ \frac{1}{N}\mathrm{Temp}(n_r, n) \right\} \quad \text{for} \quad n_{Disp} = \frac{n_\phi}{k_{\phi Dec}} \tag{5.5}$$

where a radial and a lateral discrete variable is introduced, "n_r" and "n_ϕ" respectively. To distinguish the current and previous value of the temporal variable, the symbols "n" and "n-1" are used.

Equation 5.4 accumulates the last "N" values by one addition and one subtraction per iteration. Equation 5.5 describes division by N and also decimation. The output is read only when the lateral beam counter for the display unit "n_{Disp}" equals an integral number of the lateral oversampling ratio "$k_{\phi Dec}$".

Number of DSP's: A rough estimate of the number of processors required can be found by comparing the processing capacity of one processor by the average data rate from the AD-converters.

The Processing Capacity (PC) of a particular DSP is defined:

$$PC_{DSP} = \frac{1}{T_{Inst}\, N_{Inst}} \tag{5.6}$$

"T_{Inst}" is the instruction cycle time, and "N_{Inst}" is the number of instructions required for one filter iteration at one depth location. The instruction time is processor dependent as well as the number of instruction required. Realistic values for "T_{Inst}" are in the range 33-100 nsec. The number of instructions required to execute Equations 5.4 and 5.5 is estimated to approximately $N_{Inst} = 6$. This number cannot be specified without a detailed study of the actual DSP and the HW-architecture. Synchronization and processing flow may require some additional instructions, while decimation may save some instructions.

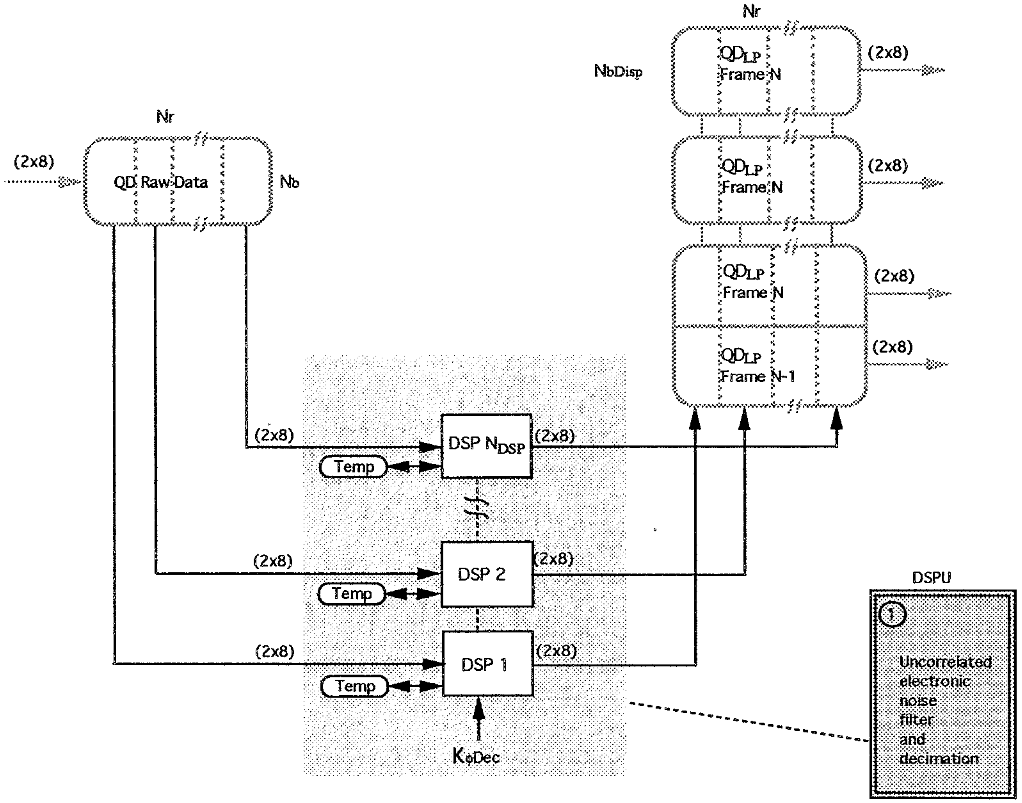

Figure 5.2 *Block diagram of the **Uncorrelated electronic noise filter.** Lateral low pass filtering is accomplished by "N_{DSP}" general digital signal processors. Each processor filters a certain number of depth locations*

The ratio of the *average data word rate* from the AD-converters (Equation 5.2) to the *processing capacity* of the actual DSP yields an expression for the minimum number of DSP's required:

$$N_{DSP} = \frac{DR_{ADave}}{PC_{DSP}} = N_b \, N_r \, f_m \, T_{Inst} \, N_{Inst} \qquad (5.7)$$

The acquired beam density "N_b" equals the lateral decimation ratio "$K_{\phi Dec}$" times the optical encoder pulse density:

$$N_{DSP} = N_{OptEnc} \, K_{\phi Dec} \, N_r \, f_m \, T_{Inst} \, N_{Inst} \qquad (5.8)$$

The input data rate is specified in "words" per second, assuming complex values. Equation 5.8 will therefore apply to a DSP that can process complex data in each instruction cycle like the LH9124 from Sharp. For the other DSP's, the number of processors will have to be doubled in order to obtain the same throughput. Some values are shown in Table 5.1 for the following realistic parameters (N_{OptEnc} =256, N_r =256, T_{Inst} =50nsec., N_{Inst}=6):

This brief estimate indicates that the required number of DSP's will be very high in order to obtain a significant noise reduction by using general DSP's. If other filter characteristics than the averaging filter are required, fast dedicated DSP's can be considered. But shifting from one job (depth location) to another reduces the effectiveness.

General digital signal processors *can* be used to realize lateral low-pass filtering. However, other more cost effective solutions should be considered, especially for high frame rates and/or over-sampling ratios.

Table 5.1 *The minimum number of DSP's versus frame rate and lateral decimation factor for T_{Inst} = 50ns and N_{Inst} = 6.*

f_m [f.p.s]	$K_{\phi Dec}$ [.]	N_{DSP} (Sharp) [.]	N_{DSP} (others) [.]
10	4	1	2
20	4	2	4
30	4	3	6
10	10	2	4
20	10	4	8
30	10	6	12
10	20	4	8
20	20	8	16
30	20	12	24

5.2.3 Reverberation detector

A block diagram of the *Reverberation detector* is shown in Figure 5.3. At this level, the maximum data rate is given by Equation 5.3, i.e. available time for one iteration is $\geq$ 500 nsec. If the instruction time for a DSP is T_{Inst}=50nsec, minimum 10 instructions per DSP are available.

The first DSPU reads the low-pass filtered and decimated data (QD_{LP}) from the memory device and calculates the complex mean-value estimate "m_ϕ" by averaging in the lateral direction. According to the previous section, one lateral averaging iteration can be accomplished with approximately 6 instructions. One single Sharp DSP can handle this in less than 500 nsec. The result is stored in a MEM-device.

The second DSPU calculates the variance estimate based on the lateral mean-value estimate. This operation is quite equal to the lateral mean value estimate, but two arguments are involved. An additional memory read access, one subtraction and one magnitude square operation are required. One single Sharp DSP can handle this.

The third DSPU generates a *reverberation detector* (RD) by taking the magnitude of the *lateral mean-value estimate* and combine with the *lateral variance estimate*. The *reverberation detector* is multiplied with the *lateral mean-value estimate* to obtain the *Reverberation Mean Estimate* which is written to a memory device. This operation involves 8 basic operations and can be executed by a single Sharp DSP.

The *Reverberation detector* can be realized by 3 powerful digital signal processors.

5.2.4 Vessel wall detector

The block diagram of the *Vessel wall detector* is shown in Figure 5.4. It is realized by six DSPU's and six MEM's. The first DSPU reads the two complex 8 bits values from the two adjacent (low-pass filtered and decimated) frames, conjugates one of them and multiplies. This result is normalized to one (assume a floating point DSP to simplify the description). The result is a unit vector whose phase is equal to the phase difference between the two input signals. This *phase difference unit vector* (PDUV) is written to two equal MEM-devices. One Sharp DSP is sufficient to perform this operation.

The next step is to do radial and lateral averaging of the PDUV's and find the magnitude of the results: the *radial phase difference magnitude* (RPDM) and the *lateral phase difference magnitude* (LPDM). One processor for each of these blocks is sufficient. The magnitudes of these averaged phase difference unit vectors are written to individual memories to simplify synchronization between DSPU's.

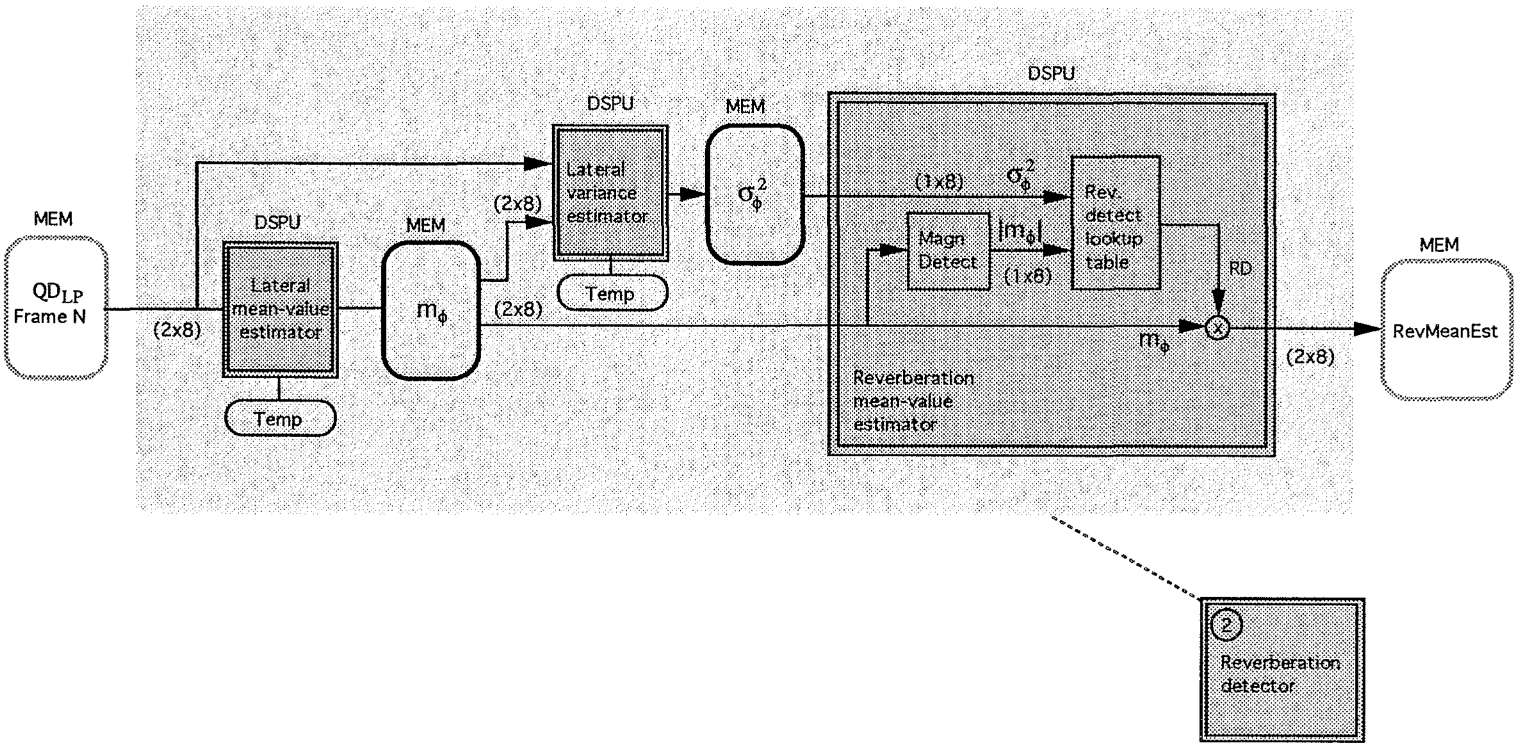

Figure 5.3 *Block diagram of the **Reverberation detector.** This block can be realized by three powerful digital signal processors.*

The variance of these estimates are reduced by averaging the magnitude detected values in the perpendicular direction. Again one processor for each block is sufficient. The result is the *radial vessel wall detector* (RVWD) and the *lateral vessel wall detector* (LVWD) which are written to individual memories.
The final operation is to combine the two detectors in the smooth OR lookup table to obtain the *phase difference vessel wall detector* (PDVWD). One DSP can easily read the proper locations in the two memories and perform the lookup function.

The *Vessel wall detector* can be realized by 6 digital signal processors.

5.2.5 Noise filter

The *Noise filter* labeled (4) in Figure 5.1 represents three simple operations:

1) A complex subtraction of the *reverberation mean estimate* (RevMeanEst) from the original image to cancel catheter reverberations.
2) A magnitude operation of the difference to obtain a gray level image signal.
3) Blood noise canceling by passing the magnitude detected signal through a lookup table.

The *Noise filter* can be accomplished by a single digital signal processor.

5.2.6 Conclusion

It is demonstrated that the *Uncorrelated electronic noise filter* based on lateral averaging *can* be realized with general digital signal processors, but other components are preferable. The *Reverberation filter* and the *Blood noise filter* can be realized with a total of 10 powerful DSP's. In addition a large number of memory and synchronization circuits is required. The flexibility in this solution is limited due to marginal processing capacity and given architecture. Little is gained in flexibility compared to the price paid in the number of components. This clearly calls for a simpler and more effective implementation.

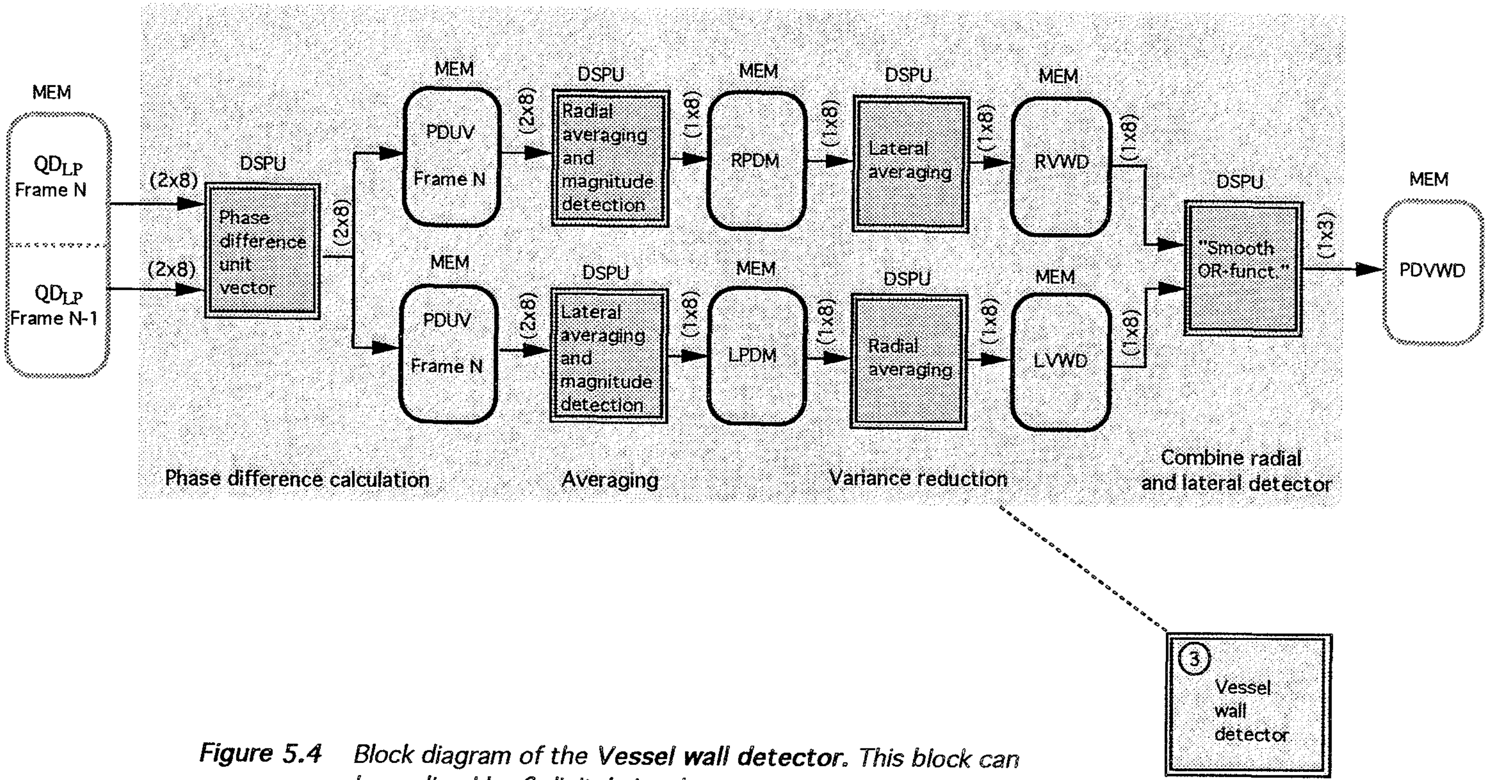

Figure 5.4 *Block diagram of the* ***Vessel wall detector****. This block can be realized by 6 digital signal processors.*

5.3 An efficient HW-solution for blood and uncorrelated electronic noise

This section describes an effective cost effective HW-solution for the *Uncorrelated electronic noise filter* and the *Blood noise filter*. The *Reverberation filter* is left out for two reasons: 1) Catheter reverberations can be reduced by careful catheter design. 2) The *Reverberation filter* complicates the implementation significantly.

5.3.1 Block diagram

The block diagram of the efficient HW-solution is shown in Figure 5.5. The number of memory devices is reduced significantly relative to the *complete solution* described in the previous section.

The uncorrelated electronic noise filtering is performed synchronized with the data rate from the AD-converters. This block is labeled (5) and denoted: *Synchronous uncorrelated electronic noise filtering and decimation.* No memory device is required between the AD-converters and the filter. Magnitude detection is also performed synchronized with the AD-converters through a lookup table, and the result can be stored as a 6 bits magnitude image rather than a complex 2x8 bits image.

Section 5.3.3 describes *hard limiting* prior to the phase difference calculation. The data format can be limited from 2x7 bits to 2x1 bits with a minor degradation of the *vessel wall detector* quality. This represents a significant memory saving since two frames are involved.

The *Blood noise filter* is split in three separate DSPU-blocks that will be described in Sections 5.3.4, 5.3.5 and 5.3.6. The first block labeled (6) takes care of the phase difference calculation and averaging in the radial and lateral directions. Magnitude detection is also performed before storage in memory devices.

In block (7), the variance of the detectors is reduced by averaging in the perpendicular direction. The results, the *radial and lateral vessel wall detectors* are stored in memory devices.

Block (8) combines the two detectors to the final *phase difference vessel wall detector* which is used to select the proper blood canceling curve.

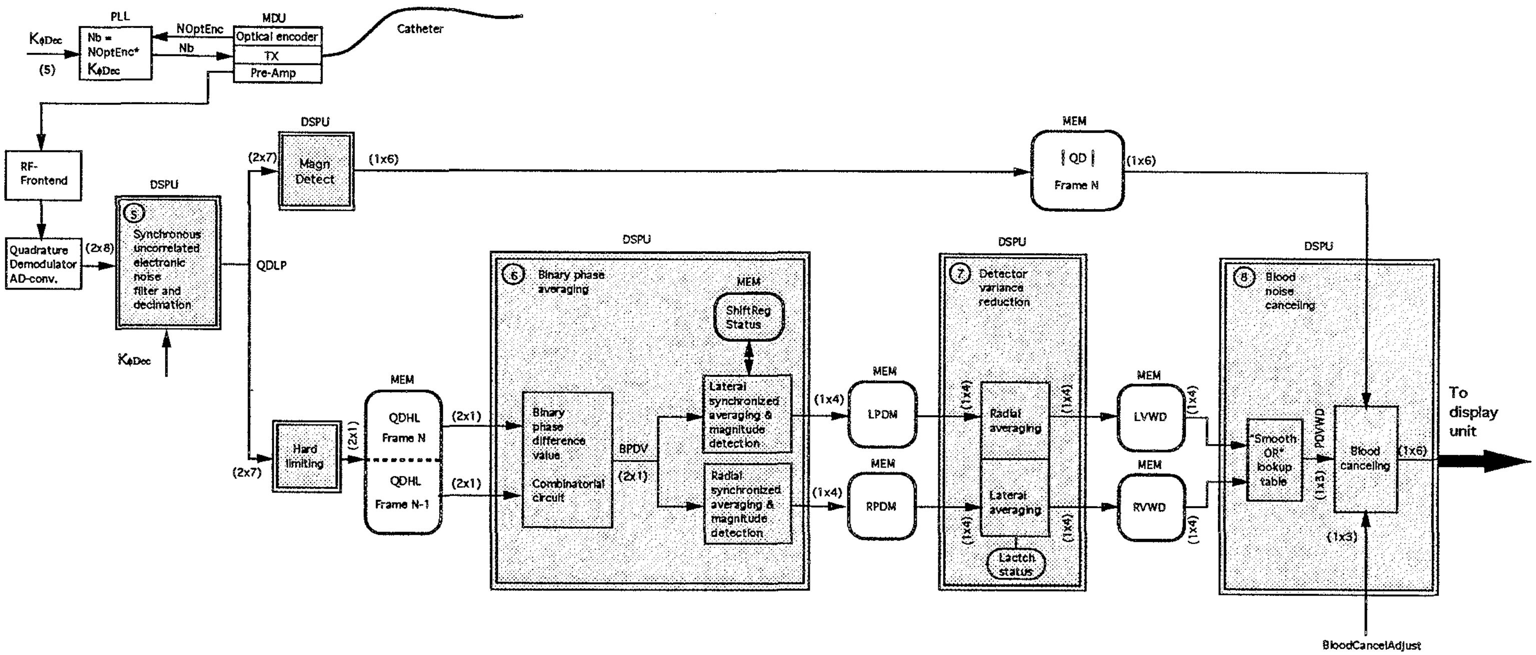

Figure 5.5 *Block diagram for the* ***efficient HW-solution for blood and electronic noise****The* ***Electronic noise filter****is running synchronized with the data rate from the AD-converters (≈20Mwords/sec.)*
The ***blood noise filter****is split in three separate blocks.*

5.3.2 Synchronous uncorrelated electronic noise filter and decimation

Data from the AD-converters are sampled in the *radial* direction, but the filter is supposed to average "N" values in the *lateral* direction for each new input value. Since a symmetric filter is supposed to be implemented, the real and imaginary value can be averaged separately. The maximum data rate is $\approx 20 \cdot 10^6$ words/sec which means that each filter iteration should be performed in maximum 50 nsec.

A possible HW-implementation structure is illustrated in Figure 5.6. The light shaded part realizes Equation 5.4 while the dark shaded part realizes Equation 5.5. Two memory devices are involved:

1) The *cyclic memory* is supposed to store the last N input values in the lateral direction in order to realize an (N-1) order filter. The *lateral write pointer* (LatWrPt) is used to address this memory for storage of the *current* input value $QD(n_r,n_\phi)$. The *lateral read pointer* (LatRdPt) is used to access the *maximum delayed* input value $QD(n_r,n_\phi-N)$. This circular memory device stores complex numbers of 2x8 bits, and it is "N_r" long and "N" values "wide".

2) The *temporal memory* stores the intermediate sums, one complex value for each radial location. The number of bits required is $2x(8+\log_2 N)$.

One filter iteration involves both read and write operations. Reading and writing can be controlled by two clock phases: "θ_1" and "θ_2". This means that a clock rate of minimum 40 MHz is required, and both a read and a write access should be performed in less than 50 nsec.

The division by "N" can be done very simply if powers of 2 are used. Some bits can simply be skipped. If other values are required, a lookup table may be used. The data format can be reduced to 2x7 bits if the output of the magnitude detector is 6 bits. Decimation is obtained by clocking only every "$K_{\phi Dec}$" value out to the next circuits.

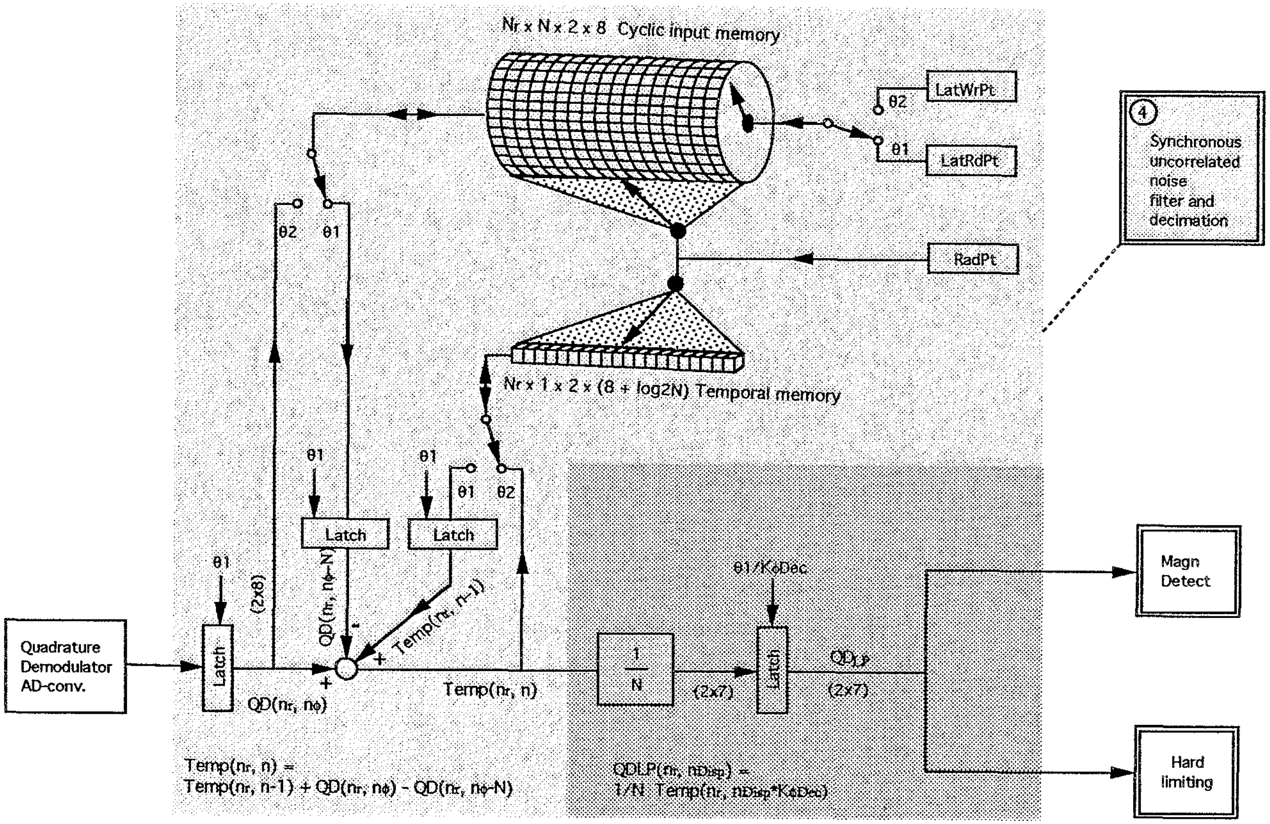

Figure 5.6 *Block diagram of the* ***Synchronous uncorrelated electronic noise filter and decimation*** *circuit.*
Averaging in the lateral direction is performed synchronized with the radial data flow at ≈20 Mwords/sec.

5.3.3 Simplification due to hard limiting

The digital representation of the phase difference between adjacent frames can be simplified by hard limiting the signals. Instead of doing 8 bits complex multiplications and divisions, simple combinatorial circuits can be used. This can be seen from the following relation, first obtained by Van Vleck [Papoulis 1965]:

$$\langle sgn(x)\, sgn(y) \rangle = \frac{2}{\pi} \sin^{-1} \frac{\langle xy \rangle}{\sqrt{\langle x^2 \rangle \langle y^2 \rangle}} \tag{5.9}$$

where

$$sgn(x) = \begin{cases} 1 & x > 0 \\ -1 & x < 0 \end{cases} \tag{5.10}$$

This relation states that the cross correlation coefficient of two zero mean Gaussian variables "x" and "y" is given by the ensemble average "$\langle \cdot \rangle$" of the product of their signs. An estimate of the left side of Equation 5.9 is much simpler to implement than an estimate of the right side. Although this relation is given for the cross correlation coefficient and based on ensemble averages, it is reasonable to assume that the calculation of the *phase difference unit vector* will be simplified as well. Hard limiting is applied to the *phase difference vessel wall detector* and tested without any further analysis.

Hard limiting: Hard limiting can be accomplished very simply in the system due to the biasing of the AD-converters, see Figure 5.7. In (a) the format of the complex signal from the quadrature demodulator is shown. "U_{QD}" is the complex analog signal in volts while "QD" is the digitized signal (see Figure 2.1). The AD-converters are biased so that the range 00-7F represents negative values, while the range 80 to FF represents positive values, i.e. *the most significant bit represents the sign.*

The digitized signal "QD" can describe ≈700 vectors around the indicated circle. If the analog signal "U_{QD}" is hard limited, the resultant vector can take only four values can be described as illustrated in (b). If this representation is scaled, and the origin is shifted, a more convenient format for digital processing is obtained, see (c). The vectors in (b) are described by the following four binary points: (0,0), (0,1), (1,0) and (1,1) which are given by the most significant bits of the AD-converters, denoted "QD_{HL}" (hard limited).

Binary phase difference: The hard limited complex signal can take only 4 values and it is described by 2 bits. The *phase difference* between two signals of this format can take 8 values, i.e. 3 bits are required to describe the phase difference. A further simplification is introduced by also limiting the number of possible *phase difference* values to 4, i.e. only 2 bits are required. Since the phase difference is no longer represented by a vector, this simplified 2 bits phase difference is denoted: Binary Phase Difference Value (BPDV).

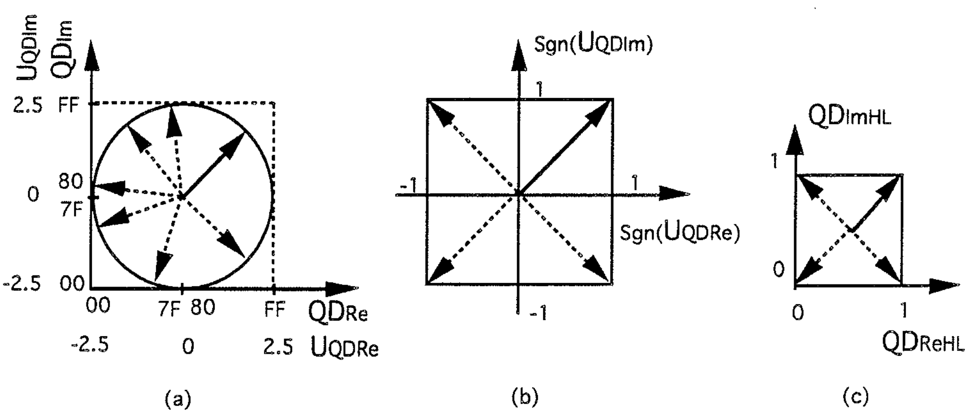

Figure 5.7 *Data format, hard limiting:*
(a) The quadrature demodulated signal is represented by two 8 bits integer numbers.
(b) The hard limited analog signal can only describe four vectors.
(c) Hard limiting the digitized signal is obtained by extracting the most significant bit. Four different values can be represented.

Comparison: A simple comparison was performed between the full 8 bits representation and the hard limited version based on the *binary phase difference value*. The result is shown in Figure 5.8 and contains data from the test described in *Test setup 4.6.* Two radial sequences (0-10mm) from adjacent frames is shown in the upper panel. The inner 6 mm represents flushing water containing Sephadex particles. The magnitudes are rarely equal. The rubber "vessel" region is located between 7-8mm, and further out the signal drops gradually until electronic noise dominates. In the vessel wall region, the magnitudes are almost equal.

The middle panel shows the *radial vessel wall detector* (RVWD) based on the two different methods. Both use R_{NR}=20 and R_{NL}=3. Note that the simplification by hard limiting has negligible influence on the result. The log-amp was used in both cases, so the data were already compressed to a certain degree.

The lower panel shows the final *phase difference vessel wall detector* (PDVWD) for the two cases. To obtain this, the lateral vessel wall detector (LVWD) (20*3) was combined with the *radial vessel wall detector* (RVWD) (20*3) through the "smooth-OR" lookup table. (In order to obtain approximately the same quality (variance) of the two detectors, the number of lateral samples "L_{NL}" was doubled from 10 to 20.)

By increasing "L_{NL}" from 10 to 20 it looks like the simplified algorithm based on hard limited signals (2 bits) performs approximately equal to the general algorithm (8 bits).

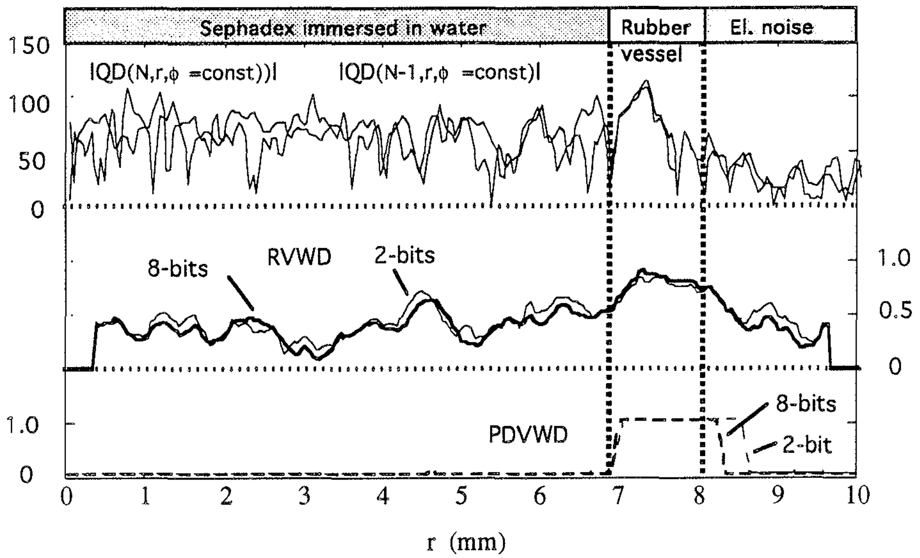

Figure 5.8 *The quality of the vessel wall detector is not reduced significantly by hard limiting the signals.*
Upper panel: magnitude of two beams from adjacent frames.
Middle panel: The radial vessel wall detector (RVWD) based on 8 bits and 2 bits (hard limited) processing.
Lower panel: The phase difference vessel wall detector (PDVWD) based on 8 bits and 2 bits (hard limited) processing.

Simplifications: The advantages of the hard limiting simplification is: *reduced complexity* and *increased speed*. Calculation of the *phase difference unit vector* the "hard way" requires one eight bits complex multiplication, an absolute value operation and a division (Equation 4.27). This can be done by a powerful signal processor (Sharp), but the calculation requires several instructions. The resultant complex number is represented by two 8 bits numbers and stored in a 16 bits memory for radial and lateral averaging.

In contrast, by taking only the sign into account, the computation of the *binary phase difference value* can be done by some simple combinatorial circuits at very high speed (<50 nsec.). The result is a complex number represented by two 1 bit numbers. The memory requirements are reduced and the computation speed is increased.

It should be noted that this simplified algorithm based on hard limited signals is not applied to entire images for display and comparison.

5.3.4 Binary phase averaging

Block (6) in Figure 5.5 describes the *binary phase difference value* calculation and radial and lateral averaging.

Binary phase difference value: Assume that the hard limited data is clocked out of the two memory devices (Frame N and Frame N-1) *radially* by a control unit. When one beam is finished, the adjacent beam is read, and the operation is repeated. Two cyclic memories are realized, and they need not contain two complete frames.

The two input signals to the binary phase difference value calculation can take 16 different values, and the output can take 4. A simple combinatorial circuit or a lookup table can execute this operation in less than 50 nsec.

Radial averaging: The *binary phase difference value* is represented by one bit in the real part and one bit in the imaginary part. These signals are supposed to be averaged in the radial direction. A possible realization is shown in the lower panel of Figure 5.9. The real and the imaginary parts are shifted in a *serial in parallel out* shift register of length R_{NR}. All the bits in the parallel output are summed. The number of bits required to represent this sum is $\log_2(R_{NR})$. According to the experiments, a realistic upper limit to R_{NR} is 32, i.e. the width of the adder should be 5 bits. The magnitude of the averaged complex number is generated by a lookup table. The result is a 4 bits number that represents the *radial phase difference magnitude* (RPDM). This value is written to a memory device using the same address as was used to read the QD_{HL}-data.

Lateral averaging: In the lateral direction, "L_{NL}" values are supposed to be averaged. The same method with *serial in parallel out* shift registers *can* be used, but this would require "N_r" registers and adders. An alternative solution is shown in the upper panel of Figure 5.9. *One* L_{NL}-bits *serial in parallel out* shift register and *one* adder is used, but the shift register content for the particular depth is stored in an N_r x L_{NL} memory. As data is clocked radially, the shift register status from that particular depth is loaded into the shift register. The shift operation, summation and magnitude detection is performed. Before the next depth location is processed, the shift register status is written back to the memory device and a radial pointer is incremented. The output of this circuit is the *lateral phase difference magnitude* (LPDM) signal which is written to a MEM-device as described above.

It is no problem to perform these operations in less than 500 nsec. The operations can be realized with general digital components, but programmable logic is more flexible and offer higher density and reliability. The XILINX devices are particularly well suited for this purpose due to the internal RAM capability. When a different filter order is required, the circuit can simply be re configured from the CPU.

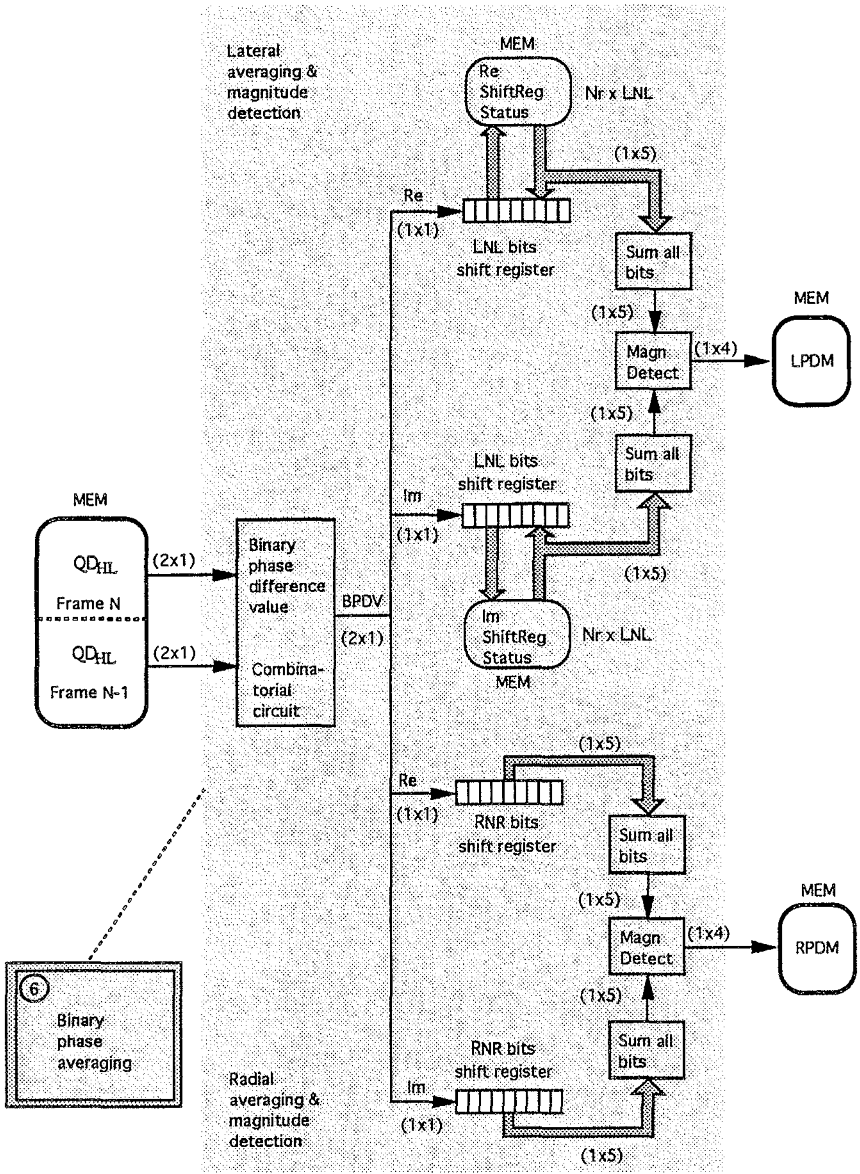

Figure 5.9 *Block diagram of one possible realization of the* ***binary phase averaging*** *circuit.*
Lateral averaging and magnitude detection are performed in the upper panel while radial averaging and magnitude detection are performed in the lower panel.

5.3.5 Detector variance reduction

The *lateral phase difference magnitude* (LPDM) is supposed to be averaged in the radial direction and the *radial phase difference magnitude* (RPDM) is supposed to be averaged in the lateral direction in order to reduce the variance of the estimates. See block (7) in Figure 5.5. The method of averaging described in the previous section can be used with small modifications. At this stage the signals are 4 bits real valued in contrast to 1 bit complex. See Figure 5.10 for illustration.

Radial averaging is performed in the upper panel. The *lateral phase difference magnitude* is read from the MEM-device and sequentially shifted through a cascade of "L_{NR}" latches (4 bits). The output of the latches are summed and divided by "L_{NR}". The resultant *lateral vessel wall detector* (LVWD) is written to a memory device.

Lateral averaging is performed in the lower panel. The status of all the "R_{NL}" latches have to be stored in a memory for each particular depth location. For each depth location, the following operations are required: a read, shift, add, divide and storage.

Again *field programmable gate arrays* are well suited for this task. Depending on the RAM capacity of these devices, additional external RAM-circuits may be required for storing the intermediate latch status. A general DSP's may be used if the number of samples to average is small (2-3).

5.3.6 Blood noise canceling

Block (8) in Figure 5.5, the *blood noise canceling* function, is supposed to read the *radial and lateral vessel wall detectors* and combine them in a lookup table to the final *phase difference vessel wall detector* (PDVWD), see Figure 5.11. Then this value is used to select the compression curve for blood rejection. Both these operations are easily realized in lookup tables and executed in less than 100 nsec.

The radial and lateral averaging introduce lags in the vessel wall estimates relative to the magnitude detected image. This means that three different address pointers are needed to keep track of the proper addresses versus the filter parameters, a memory address generator is required. A programmable device is well suited for this task.

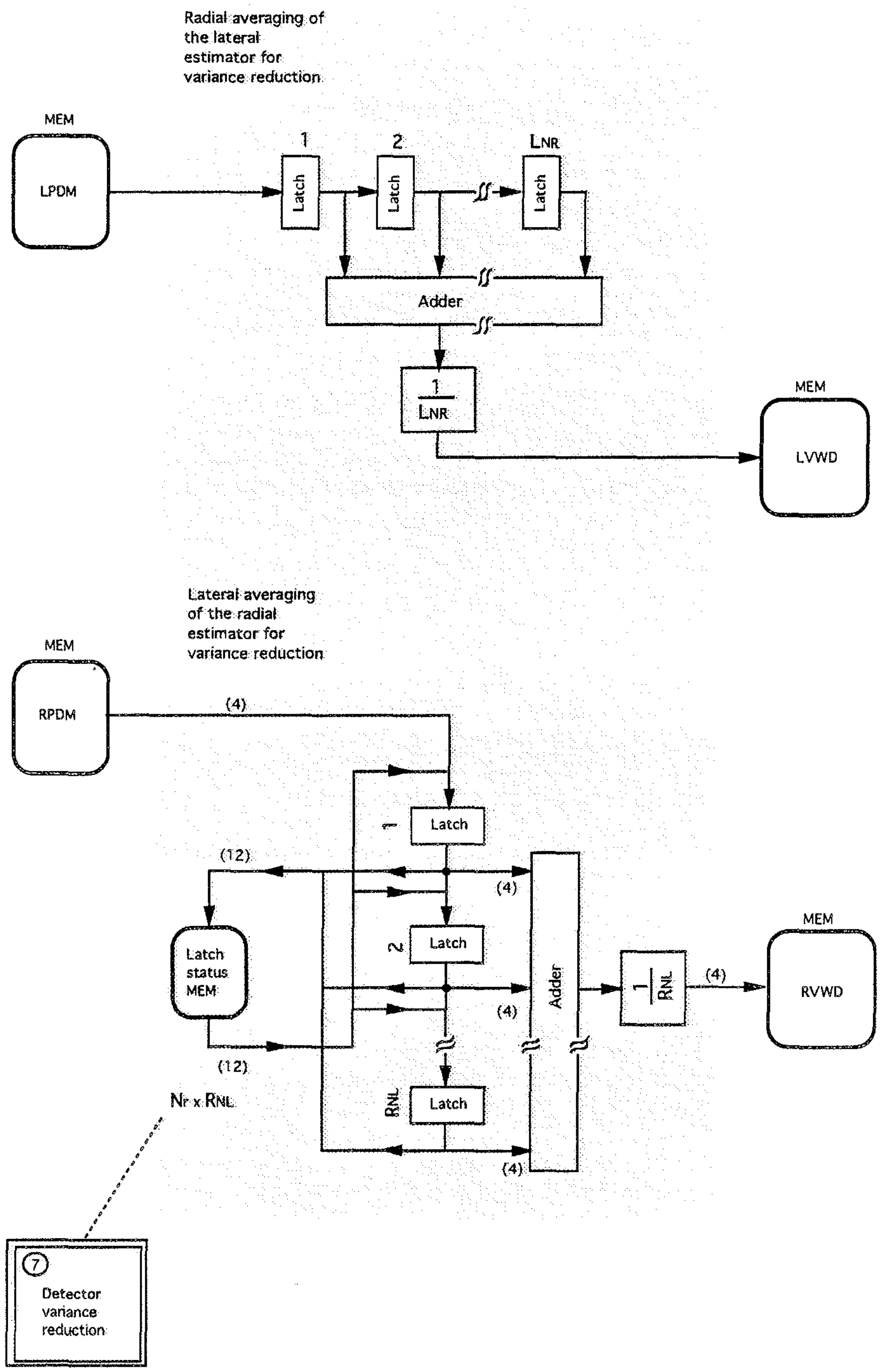

Figure 5.10 *Block diagram of the* ***detector variance reduction*** *circuit including radial averaging of the lateral estimate (upper panel) and lateral averaging of the radial estimate (lower panel)*

Synchronization: No synchronization network is shown in the block diagrams. Obviously, some control circuit is needed to access all the memory-devices in proper order. The suggested structure is supposed to run as three partially independent processes. The blocks labeled (6), (7) and (8) in Figure 5.5 have their own address generators. Reading from memory, processing data and writing to memory is locally controlled within that particular block.

Due to the lags generated in the radial and lateral averaging, the process in block (8) should run with a lag to block (7), and block (7) should run with a lag to block (6). These lags are not critical as long as they are large enough to inhibit access to invalid data. Some additional electronics is required to take care of this synchronization. Programmable devices are well suited for this task as well.

The radial boundaries of the image (inner and outer regions) need a special action due to invalid data. This may require some extra electronics and programming.

5.3.7 Conclusion

A cost effective HW-solution for the *Uncorrelated electronic noise filter* and the *Blood noise filter* is presented. *Field programmable gate arrays* are well suited for the task, in particular the XILING circuits. Both filters are expected to fit on a standard dual size Europe printed circuit board.

The *Uncorrelated electronic noise filter* processes synchronized with the AD-converter. This means there are no practical restrictions on the frame rate or the lateral oversampling ratio.

The *Blood noise filter* is based on the hard limiting simplification, a possible but not necessary method. This simplification saves components, cost and board real estate. The performance of this simplified algorithm is only tested on one dimensional data sets. The simplification degrades the quality of the filter negligible.

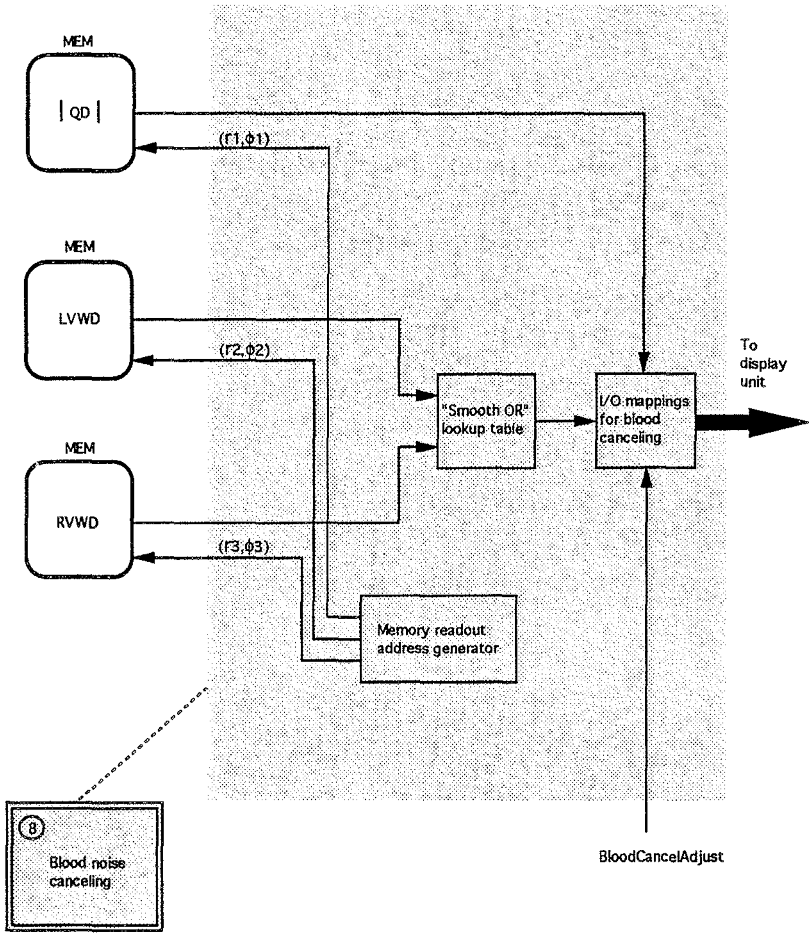

Figure 5.11 *Block diagram of the **Blood noise canceling** circuit combining data from three memory devices and performing vessel wall detection through the smooth OR-lookup table and blood noise canceling through another lookup table.*

REFERENCES

Angelsen B. A. J. (1991). *"Waves, Signals and Signal Processing in Medical Ultrasonics"*, Department of Biomedical Engineering, University of Trondheim, Norway.

Baum R. F. (1957).*"The Correlation Function of Smoothly Limited Gaussian Noise"*, IRE Transaction on Information Theory, March.

Brubakk A.O. (1978) and R. Aaslid. *"Use of a model for simulating individual aortic dynamics in man"*, Med. & Biol. Eng. & Comput. May.

Cole J.S. (1977) and Hartley C.J. . *"The pulsed Doppler Coronary Artery Catheter. Preliminary Report of a New Technique for Measuring Rapid Changes in Coronary Artery Flow Velocity in Man"*, Circulation, Vol 56, No 1, July.

Folts J.D. (1977), Gallagher k. and Rowe G.G.. *"Hemodynamic effects of controlled degrees of coronary artery stenosis in short-term and long-term studies in dogs"*, J Thorac Cardiovasc Surg; 73:59-65.

Foster F.S. (1991), Pavlin C.J., Lockwood G.R., Ryan L.K., Harasiewicz K., Berube L. and Rauth A.M. *"Ultrasound backscatter imaging"*, 1991 Ultrasonics symposium pp. 1161-1169.

Fronek A. (1989), *"Noninvasive diagnostics in vascular disease"*, McGraw-Hill, New York.

Hokanson D.E. (1972), *"A phase-locked echo tracking system for recording arterial diameter changes in vivo"*. J. of Applied Physiology, Vol. 32, No. 5, May.

Insana M.F. (1986) and Wagner R.F. *"Analysis of ultrasound image texture via generalized Rician statistics"*, Optical Engineering 25(6), June.

Jacovitti G. (1987) and Cusane R*"An Efficient Technique for High Correlation Estimation"*, IEEE Transactions on acoustics, speech, and signal processing, VOL. ASSP-35, NO. 5. May.

Kino G. S. (1987). *"Acoustic Waves, Devices, Imaging, & Analog Signal Processing"*, Prentice-Hall, New Jersey.

Motchenbacher C.D. (1973) and Fitchen F.C.*"Low-Noise Electronic Design*, John Wiley & Sons, Inc.

Nichols W.W. (1990) and O'Rourke M.F. , *"McDonald's Blood Flow in Arteries: theoretic, experimental, and clinical principles."*, Third Edition, E. Arnold, London.

Papoulis A. (1965). *"Probability, Random Variables and Stochastic Processes"* Tokyo, Japan: McGraw-Hill.

Roberts R. A. (1987) and Mullis C.T. *"Digital signal processing"*, Addison-Wesley.

Seggie D.A.(1987), *"Deterministic approach towards ultrasound speckle reduction"*, IEE Proceedings, Vol. 134, Pt.A, No.2, Feb.

Sibley D. H. (1986), Millar H.D., Hartley C.J. and Whitlow P.L. *"Subselective Measurement of Coronary Blood Flow Velocity Using a Steerable Doppler Catheter"*, JACC Vol.8. No6, December.

Skolnik M.I.(1962), *"Introduction to radar systems"*, New York, McGraw-Hill.

Van Trees H.L. (1968), *"Detection, Estimation, and Modulation Theory. Part I"*, John Wiley & Sons, Inc.

Wagner R.F. (1986), Insana M.F. and Brown D.G. *"Unified approach to the detection and classification of the speckle texture in diagnostic ultrasound"*. Optcal engineering, Vol. 25, No. 6, June.

Wagner R.F. (1987), Insana M.F. and Brown D.G. *"Statistical properties of radio-frequency and envelope-detected signals with applications to medical ultrasound"*. J. Opt. Soc. Am. A/Vol. 4, No. 5/ May.

Wiersema M.J. (1989), Reilly C.R., Sanghvi N.T., Hawes R., Wiersema L. and Aust C. *"Tventyfive MHz gastrointestinal ultrasonography"*, IEEE Ultrason. Symp. Proc. IEEE Cat. No. 89CH2791-2, pp. 845-848, IEEEE, New York.

Yock P.G. (1989), Linker D.T. and Angelsen B.A., *"Two dimensional intravascular ultrasound: Technical development and initial clinical experiance"*, J. Am. Soc. Echo., 2:296-304.